First Results from the HERMES Experiment using Unpolarized Targets

Dissertation
zur Erlangung des Doktorgrades
des Fachbereichs Physik
der Universität Hamburg

vorgelegt von
Klaus Ackerstaff
aus Weidenau
(jetzt Siegen)

Hamburg
1996

Gutachter der Dissertation:	Prof. Dr. A. Wagner
	Prof. Dr. B. Naroska
Gutachter der Disputation:	Prof. Dr. A. Wagner
	Prof. Dr. E. Lohrmann
Datum der Disputation:	28. 5. 1996
Sprecher des Fachbereichs Physik,	
Vorsitzender des Promotionsausschusses:	Prof. Dr. B. Kramer

Zusammenfassung

Thema dieser Arbeit sind Tests der experimentellen Methoden des HERMES Experiments und die Analyse der ersten Daten, die 1995 mit unpolarisierten Targets genommen wurden.

Das HERMES Experiment ist konstruiert worden, um die Spinstruktur der Nukleonen mittels tiefinelastischer Streuung polarisierter Elektronen oder Positronen an polarisierten Gastargets zu untersuchen. Es wurde 1994/95 in den HERA-Ring bei DESY eingebaut. Zum ersten Mal wurde ein internes polarisiertes Speicherzellentarget in einem Elektronen-Positronen-Speicherring hoher Energie benutzt.

Während eines Testexperiments 1994 und während der Datennahme 1995 wurde diese neuartige Target-Technologie eines internen Speicherzellentargets im HERA-Ring studiert. Die Ergebnisse dieser Tests sowie Studien von Prototypen einiger Detektorkomponenten werden diskutiert.

HERMES hat 1995 Daten mit einem polarisierten $^3\mathrm{He}$ Target und mit unpolarisierten $\mathrm{H}_2/\mathrm{D}_2$ Targets genommen. Die Analyse der Daten mit unpolarisierten Targets wird im Detail beschrieben. Die Messung des Strukturfunktionsverhältnisses $F_2^{\mathrm{n}}/F_2^{\mathrm{p}}$ als erstes physikalisches Ergebnis des HERMES Experiments zeigt gute Überinstimmung mit früheren Messungen und unterstreicht, daß sowohl das Spektrometer als auch die Analyse verstanden ist.

Darüberhinaus wird eine Messung des noch nicht bestimmten Strukturfunktionsverhältnisses $F_2^{^3\mathrm{He}}/F_2^{\mathrm{D}}$ vorgestellt, welche die zukünftigen Möglichkeiten des HERMES Experiments in unpolarisierter Physik aufzeigt.

Erste vorläufige Ergebnisse aus semiinklusiven Messungen mit unpolarisierten Targets werden diskutiert, die die Stärke des HERMES Experiments in diesem Bereich zeigen. Das Verhältnis der Valenzquarkverteilungen wird bestimmt und eine Messung der Seequark Flavor-Asymmetrie wird untersucht.

Abstract

The subject of this thesis is the test of the experimental techniques of the HERMES experiment and the analysis of the first data taken with unpolarized targets in 1995.

The HERMES experiment is designed to measure the spin structure of the nucleon by deep inelastic scattering of polarized electrons or positrons off polarized gas targets. It was installed into the HERA ring at DESY in 1994/95. For the first time an internal polarized storage cell target was used in a high energy electron/positron storage ring.

Tests of the novel target technique using an internal storage cell target in the HERA ring have been performed during a test-experiment in 1994 and during the first data taking in 1995. The results are discussed along with results from the performance of prototype spectrometer components.

In 1995 HERMES took data with a polarized $^3\mathrm{He}$ target and with unpolarized $\mathrm{H}_2/\mathrm{D}_2$ targets. The analysis of the unpolarized target data is presented in detail. The extraction of the structure function ratio $F_2^{\mathrm{n}}/F_2^{\mathrm{p}}$ as the first physics result obtained at HERMES shows good agreement with previous measurement and proves the understanding of the experiment and analysis.

In addition the extraction of the structure function ratio $F_2^{^3\mathrm{He}}/F_2^{\mathrm{D}}$ which is a unique measurement is described, giving an outlook on future possibilities of HERMES in unpolarized physics.

Preliminary results on semi-inclusive measurements with unpolarized targets are discussed and confirm the strength of the HERMES detector in measuring semi-inclusive processes. The valence quark distribution function ratio is determined and a proposed measurement of the sea quark flavor asymmetry is studied in this thesis.

Contents

List of Figures

Chapter 1

Introduction

Much progress has been made in the investigation of the structure of the nucleon in the last decades. Beyond the measurement of static properties like mass, charge, magnetic moments, spin and parity etc. which have been carried out in the early days, scattering experiments resolved the substructure of the nucleon in the last years. As a result from early deep inelastic scattering experiments in the late 1960's at the Stanford Linear Accelerator Center (SLAC) the Quark Parton Model (QPM) emerged as an explanation for the observed independence of the cross section of the scale at which the nucleon was probed. In the simplest model the nucleon consists of three fundamental point-like particles called *valence quarks*. The additive quantum numbers of the nucleon hence can be understood as the sum of it's partons quantum numbers. This simplified picture has been extended further by deep inelastic scattering experiments around the world in the last years.

The more deeply experiments probed the substructure the more questions arose and deviations from the simple picture of the QPM emerged. The European Muon Collaboration [Aub83] for example detected a slight difference in the muon-nucleon scattering depending on the target nucleus, the EMC-effect.

Another surprising result of this experiment was that the spin of the nucleon is not the simple sum of the parton spins. Today's experiments indicate that quarks contribute around 27% of the nucleon's spin. The question where the spin of the nucleon comes from has been the motivation to design the HERMES experiment at HERA .

HERA is an electron-proton collider located at DESY. A stored proton beam collides with a stored electron or positron beam in two interaction regions, North and South, where the experiments H1 and ZEUS are located. These experiments investigate the substructure of the nucleon at very high center of mass energies. In 1994/95 a third experiment, HERMES has been installed in the East section of the HERA ring. HERMES took first data using only the polarized positron beam together with a fixed polarized target. A fourth experiment, HERA-B, is currently installed in the West section designed to investigate heavy quarks using only the proton beam with a fixed target.

HERMES is designed to measure the spin structure of the nucleon with high systematic precision and also to extend previous measurements. HERMES has the capability of disentangling the different contributions to the nucleon spin via *semi-inclusive* measurements. In addition a wide variety of different unpolarized targets enables HERMES to measure various properties of nucleons in different nuclei.

This thesis describes first tests of the experimental technique and first results of the HERMES experiment obtained using data taken in 1995 with unpolarized targets.

Chapter 2

Physics Concepts

HERMES performs measurements on the structure of nucleons via *Deep Inelastic Scattering* (DIS). In the DIS-regime a virtual photon scatters off constituents of nucleons. The virtual photons are emitted by beam-positrons interacting with target nucleons. The positrons and other particles produced in the reaction are scattered mostly into the forward direction. By detecting the scattered positron the reaction kinematics are deduced to gain information on the scattering process and the underlying physics. HERMES concentrates on the spin dependency of the DIS reaction to retrieve information on the composition of the nucleon spin. Apart from the measurement of only the scattered positron which is called *the inclusive* measurement additional information can be obtained by detecting hadrons produced in the scattering process

This chapter gives an overview of the basic DIS process with special emphasis on the physics of the measurements described in this work.

2.1 The DIS Kinematics

The fundamental scattering process of a lepton scattering off a nucleon via exchange of a virtual vector boson is sketched in figure 2.1. In the following only the electro-magnetic case will be described. At HERA energies (27.5 GeV) and fixed targets the weak neutral and charged current is small and can be treated as a perturbation. In lowest order the incoming lepton[1] emits a virtual photon in the scattering process which then interacts with the nucleon. The scattered lepton is used to determine the kinematics of the event. The four-vector of the incoming lepton is denoted by k where the outgoing is k'. Analogously p denotes four-vector of the incoming nucleon, p' the four-vector of the hadronic final state X. The virtual photon γ is represented by the four-vector $q = k - k'$ and in the laboratory frame it carries the energy $\nu = E - E'$ lost by the lepton. The negative four momentum square of the virtual photon Q^2, the relative energy transfer to the photon ν

[1] positrons in the HERMES case

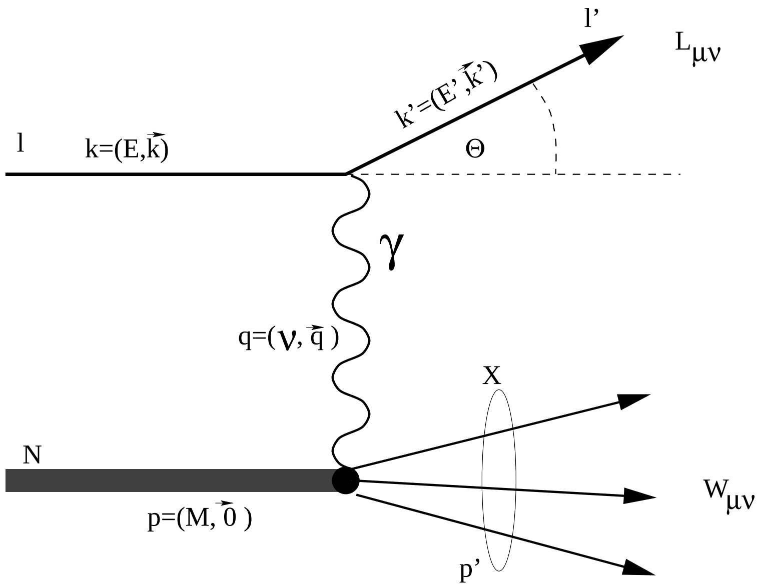

Figure 2.1: First order (one photon exchange) scattering of leptons from nucleons. The incoming lepton l scatters emitting a virtual photon γ into the outgoing lepton state l'. The target nucleon N absorbs the virtual photon producing the final state X.

and the squared invariant mass of the photon nucleon system W^2 are defined in a standard way:

$$Q^2 = -q^2 = -(k-k')^2 > 0 \;, \tag{2.1}$$
$$\nu = \frac{p \cdot q}{M} \;, \tag{2.2}$$
$$W^2 = p'^2 \overset{\text{lab}}{=} M^2 + 2M\nu - Q^2 \;, \tag{2.3}$$

where M is the mass of the proton; the lepton mass can be neglected at high energies. For HERMES the Lorentz invariants can be expressed in terms of the energy E of the incoming electron, the scattering angle θ and energy E' of the outgoing (measured) electron in the laboratory frame as follows:

$$Q^2 \overset{\text{lab}}{=} 4EE' \sin^2(\theta/2) \;, \tag{2.4}$$
$$\nu \overset{\text{lab}}{=} E - E' \;. \tag{2.5}$$

The wavelength of the virtual photon is proportional to $1/\sqrt{Q^2}$, hence Q^2 is a measure of the scale at which the target nucleon is probed. There are two dimensionless scaling variables commonly used which are related to the above variables through:

$$x = \frac{Q^2}{2p \cdot q} \overset{\text{lab}}{=} \frac{Q^2}{2M\nu} \;, \tag{2.6}$$

$$y = \frac{p \cdot q}{p \cdot k} \stackrel{\text{lab}}{=} \frac{\nu}{E} \,. \tag{2.7}$$

In the infinite momentum frame where the nucleon has an infinitely large momentum and all masses and transverse momenta can be neglected x (commonly known as x-Bjørken) is the fraction of the nucleon's momentum carried by the struck quark. The scaling variable y in the laboratory frame is the fractional energy of the incident electron transferred to the target nucleon.

2.2 The Cross Section

In the one photon exchange approximation the double differential cross section can be written in terms of the leptonic tensor $L_{\mu\nu}$ and the hadronic tensor $W^{\mu\nu}$ as:

$$\frac{d^2\sigma_{1\gamma}}{dQ^2 d\nu} = \frac{4\pi\alpha^2}{Q^4 E^2} L_{\mu\nu} W^{\mu\nu} \,, \tag{2.8}$$

where $\alpha \approx \frac{1}{137}$ is the fine structure constant. The leptonic tensor describes the lepton-photon vertex whereas the hadronic tensor describes the photon-nucleon vertex and hence includes the information on the structure of the nucleon. The leptonic tensor describing a point-like interaction can be derived from QED [Sch88] using the spinors $u(k, s)$ where k is the above mentioned four-vector and s describes the spin of the lepton:

$$L_{\mu\nu} = \frac{1}{2} \sum_{s'} \bar{u}(k', s') \gamma_\mu u(k, s) \bar{u}(k, s) \gamma_\nu u(k', s') \,. \tag{2.9}$$

The spin states of the outgoing leptons s' are summed since they are not observed. The above expression can be calculated in terms of a simple trace in case the incoming lepton is unpolarized (averaged over incoming lepton spin)[2]:

$$\begin{aligned} L_{\mu\nu} &= \frac{1}{2} \mathrm{T} \left[\gamma_\mu (\not{k} + m) \gamma_\nu (\not{k}' + m) \right] \\ &= 2[k_\mu k'_\nu + k_\nu k'_\mu - (k \cdot k') g_{\mu\nu}] + 2m^2 g_{\mu\nu} \,. \end{aligned} \tag{2.10}$$

For the polarized case an additional spin dependent term (underlined) remains in the leptonic tensor:

$$L_{\mu\nu} = 2[k_\mu k'_\nu + k_\nu k'_\mu - (k \cdot k') g_{\mu\nu}] + 2m^2 g_{\mu\nu} + \underline{2mi\epsilon_{\mu\nu\alpha\beta} S^\alpha (k - k')^\beta} \,, \tag{2.11}$$

where $\epsilon_{\mu\nu\alpha\beta}$ is the 4-dimensional totally anti-symmetric tensor. S is the spin four-vector of the incoming lepton:

$$S^\alpha = \frac{1}{2} \bar{u}(k, s) \gamma^\alpha \gamma_5 u(k, s) \,. \tag{2.12}$$

[2] $\not{k}$ is defined as $\not{k} := \gamma^\mu k_\mu$, γ^μ are the Dirac matrices.

The hadronic tensor is not calculable from fundamental principles. The most general ansatz, expressing $W_{\mu\nu}$ in terms of Lorentz invariants and scalar functions is simplified via symmetry requirements. Requiring Lorentz invariance, parity conservation (for pure electro-magnetic processes) and invariance under time reversal yields [Lea82]:

$$\begin{aligned} W_{\mu\nu} &= \left(-g_{\mu\nu} + \frac{q_\mu q_\nu}{q^2}\right) W_1(q^2,\nu) \\ &+ \left[\left(p_\mu - \frac{p\cdot q}{q^2}q_\mu\right)\left(p_\nu - \frac{p\cdot q}{q^2}q_\nu\right)\right]\frac{W_2(q^2,\nu)}{M^2} \\ &+ i\epsilon_{\mu\nu\alpha\beta}q^\alpha M S_h^\beta G_1(q^2,\nu) \\ &+ i\epsilon_{\mu\nu\alpha\beta}q^\alpha[(p\cdot q)S_h^\beta - (S_h\cdot q)p^\beta]\frac{G_2(q^2,\nu)}{M} \ . \end{aligned} \tag{2.13}$$

S_h is the polarization vector of a spin-1/2 target nucleon and W_1, W_2, G_1, G_2 are scalar functions depending on Q^2 and ν, describing the structure of the target nucleon. The unpolarized case is described by the first two terms since the last two vanish when averaging over the spin states.

2.2.1 The Unpolarized Structure Functions

In the unpolarized case the double differential cross section for lepton-nucleon scattering only involves the symmetric part of the hadronic tensor:

$$\frac{d^2\sigma_{1\gamma}}{dQ^2 d\nu} = \frac{4\pi\alpha^2}{Q^4E^2}\left(W_2(Q^2,\nu)\cos^2\frac{\theta}{2} + 2W_1(Q^2,\nu)\sin^2\frac{\theta}{2}\right) \ . \tag{2.14}$$

The same calculation as described above can be applied to elastic scattering of two point-like spin 1/2 particles where one only has two lepton-like tensors[3]. The cross section for this process can be analytically calculated:

$$\frac{d^2\sigma_{1\gamma}}{dQ^2 d\nu} = \frac{4\pi\alpha^2}{Q^4E^2}\left[\left(\cos^2\frac{\theta}{2} + \frac{Q^2}{2m^2}\sin^2\frac{\theta}{2}\right)\delta(\nu - \frac{Q^2}{2m})\right] \ , \tag{2.15}$$

where m denotes the mass of the target particle. Comparison of the two results suggests the following equations:

$$\begin{aligned} 2mW_1 &= \frac{Q^2}{2m}\delta(\nu - \frac{Q^2}{2m}) \ , \\ \nu W_2 &= \delta(\nu - \frac{Q^2}{2m}) \ . \end{aligned} \tag{2.16}$$

[3]e.g. the hypothetical case of $e-\mu$ scattering

If lepton-nucleon scattering can be explained as incoherent scattering off point-like constituents inside the nucleon, the structure functions $W_{1/2}$ only depend on $x = Q^2/2m\nu$ and not on Q^2 itself. In other words if x is defined with the parton mass, elastic scattering off a parton fixes x to one. Since the mass of the partons is unknown within $0 < m_{\text{parton}} < M$, $x_{Bj} = \frac{Q^2}{2M\nu}$ is defined with the proton mass M and x can be interpreted as the fractional momentum of the parton in the infinite momentum frame.

Experimental results (discussed later) support this picture, which is the Quark Parton Model based on the following assumptions:

- all hadrons (nucleons) consist of partons (quarks and gluons), deep inelastic lepton scattering off a hadron can be described in terms of a virtual photon exchange between the lepton and a quark inside the hadron,

- parton-parton interactions inside the hadron are negligible during the time of the interaction. The momenta of the partons are parallel to the momentum of the hadron they are contained in.

The probability of finding a parton i with momentum fraction x inside the proton is $f_i(x)$. In the Bjørken scaling limit where Q^2 and ν go to infinity, the structure functions reduce to only x-dependent structure functions:

$$
\begin{aligned}
F_2(x) &\overset{\substack{Q^2\to\infty \\ \nu\to\infty}}{=} \nu W_2(x) = \sum_i e_i^2 f_i(x) x \;, \\
F_1(x) &\overset{\substack{Q^2\to\infty \\ \nu\to\infty}}{=} M W_1(x) = \frac{1}{2}\sum_i e_i^2 f_i(x) \;. \qquad (2.17)
\end{aligned}
$$

Thus the structure functions $F_{1/2}(x)$ are related to the sum over all parton distribution functions $f_i(x)$. This means in the scaling limit only one independent structure function remains:

$$F_2(x) = 2xF_1(x) \;, \qquad (2.18)$$

which is known as the *Callan-Gross-Relation*.

Another way of looking at the cross section is expressing the total electro-magnetic cross section in terms of the flux of the virtual photons Γ and the absorption cross section for longitudinal (helicity $\lambda = 0$) and transverse ($\lambda = \pm 1$) photons ($\sigma_{\mathrm{L}}/\sigma_{\mathrm{T}}$):

$$\sigma = \Gamma(\sigma_{\mathrm{T}} + \epsilon\sigma_{\mathrm{L}}) \;, \qquad (2.19)$$

where ϵ is the ratio of probabilities that a lepton emits a longitudinally or transversely polarized virtual photon:

$$\epsilon = \frac{\Gamma_{\mathrm{L}}}{\Gamma_{\mathrm{T}}} = \frac{1-y}{1-y+y^2/2} \;, \qquad (2.20)$$

then the ratio $R(Q^2, x) = \sigma_\mathrm{L}/\sigma_\mathrm{T}$ is:

$$R(Q^2, x) = \frac{(1 + \frac{4M^2x^2}{Q^2})F_2(Q^2, x) - 2xF_1(Q^2, x)}{2xF_1(Q^2, x)} \ , \tag{2.21}$$

and hence the *Callan-Gross-Relation* holds if only transverse photons interact with partons.

The double differential cross section finally is given in terms of F_2 and R as

$$\frac{d^2\sigma(Q^2, x)}{dQ^2dx} = \frac{4\pi\alpha^2}{xQ^4}F_2(Q^2, x)\left[(1 - y - \frac{Q^2}{4E^2}) + \frac{(y^2 + Q^2/E^2)}{2(1 + R(Q^2, x))}\right] \ . \tag{2.22}$$

The deviations from the pure QPM assumptions where masses are neglected as well as transverse momenta of partons inside the nucleons are then described by the ratio $R(Q^2, x)$.

2.2.2 Unpolarized Inclusive Measurements

As stated above the structure function F_2 can be expressed in terms of parton distributions $f_i(x)$ inside the nucleon. In the QPM and scaling limit this means:

$$F_2(x) = \sum_i e_i^2 f_i(x)x \ . \tag{2.23}$$

Assuming only valence quarks the structure function for the proton is described by the distribution function $u^p(x)$ for the two u-quarks with charge $\frac{2}{3}$ (always referring to the electron charge) and the distribution function $d^p(x)$ for the d-quark with charge $-\frac{1}{3}$:

$$F_2^p(x) = \frac{4}{9}xu_v^p(x) + \frac{1}{9}xd_v^p(x) \ . \tag{2.24}$$

If the distribution functions are isospin invariant then going from the proton to the neutron by flipping the isospin the following relation for the distribution functions holds:

$$u^n(x) = d^p(x); \ \ d^n(x) = u^p(x) \ . \tag{2.25}$$

Adding quark anti-quark pairs, which are produced by gluons radiated from the valence quarks with high momentum, results in a *"sea"* of low momentum (low x) $u\bar{u}, \ d\bar{d}, \ s\bar{s}$ pairs forming an SU(3) singlet (neglecting heavy quarks). These pairs can be expressed by one function assuming the sea is isospin symmetric:

$$\sum_\mathrm{sea} e_i^2 f_i^p(x) = \sum_\mathrm{sea} e_i^2 f_i^n(x) = f_\mathrm{sea}(x)\sum_\mathrm{sea} e_i^2 = \frac{4}{3}f_\mathrm{sea}(x) \ . \tag{2.26}$$

Then the structure function for the neutron and proton can be written as:

$$
\begin{aligned}
F_2^p &= x\left(\frac{4}{9}u_v^p(x) + \frac{1}{9}d_v^p(x) + \frac{4}{3}f_{\text{sea}}(x)\right) , \\
F_2^n &= x\left(\frac{4}{9}d_v^p(x) + \frac{1}{9}u_v^p(x) + \frac{4}{3}f_{\text{sea}}(x)\right) .
\end{aligned} \tag{2.27}
$$

In QCD the distribution functions can not be computed so they have to be adjusted to experimental results.

With the above assumption one can derive certain constraints on the quark distribution function by measuring the fundamental structure function ratio $F_2^{\mathrm{n}}/F_2^{\mathrm{p}}$:

- if the sea dominates over the valence quarks the ratio has to be 1,
- if the valence quarks dominate the ratio is between 1/4 and 4,
  - for exact SU(6) symmetry ($u_v(x) = 2d_v(x)$) it is 2/3 [Car75],
  - in case $u_v(x)$ dominates it goes to 1/4,
  - in case $d_v(x)$ dominates it goes to 4.

First results on the measurement of the structure function ratio using H_2 and D_2 targets are described in chapter 5.

2.2.3 The Polarized Structure Functions

The information on the spin distribution inside the nucleon is contained in the antisymmetric part of the hadronic tensor $W_{\mu\nu}$ (see equation 2.13). In the unpolarized case this contribution of the tensor to the cross section vanishes when averaging over the spin states, in the polarized case the symmetric part cancels out when looking at the cross section difference of leptons with opposite spin states. To see this one has to look closer into the scattering process. Figure 2.2 shows the definition of the angles α and φ with respect to the target polarization S and the lepton momenta k, k'. The lepton spin is oriented parallel or anti-parallel to its initial momentum. The cross section difference $\sigma^S - \sigma^{-S}$ only depends on the antisymmetric part of the lepton and hadron tensor (see equations 2.11, 2.13). In the laboratory system it is:

$$
\frac{d^3\sigma^S}{d\cos\theta\, d\phi\, dE'} - \frac{d^3\sigma^{-S}}{d\,\cos\theta\, d\,\phi\, dE'} = \frac{2\alpha^2}{MQ^4}\frac{E'}{E}L_{\mu\nu}^{(A)}W^{\mu\nu(A)} , \tag{2.28}
$$

where $L_{\mu\nu}^{(A)}W^{\mu\nu(A)}$ are the antisymmetric parts of the leptonic and hadronic tensors. Now the same arguments as for the unpolarized case yield two scale invariant (Q^2-independent)

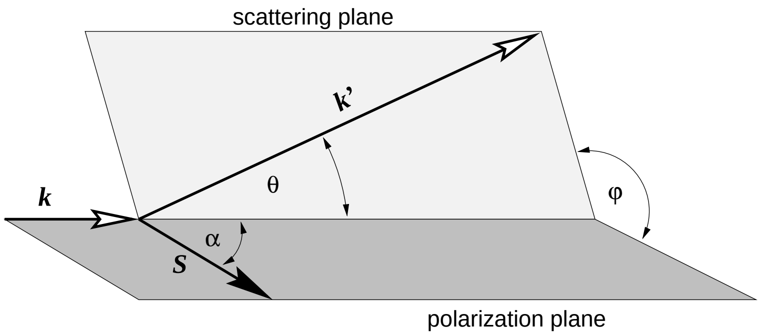

Figure 2.2: The definition of scattering angles in polarized DIS. S denotes the target spin, α is the angle between the target spin and the beam direction, k, k' are the four momenta of the incoming, outgoing lepton, θ is the scattering angle of the lepton and φ is the angle between the scattering plane and the polarization plane.

spin structure functions which are related to the structure functions $G_{1/2}$ (see equation 2.13). In the scaling limit this leads to the following relations:

$$\begin{aligned} M^2\nu G_1(Q^2,\nu) &\overset{\substack{Q^2\to\infty \\ \nu\to\infty}}{=} g_1(x) \ , \\ M\nu^2 G_2(Q^2,\nu) &\overset{\substack{Q^2\to\infty \\ \nu\to\infty}}{=} g_2(x) \ . \end{aligned} \tag{2.29}$$

The spin structure function $g_1(x)$ can be expressed in terms of parton distribution functions in a similar way as it was done for the unpolarized structure functions (see equation 2.17):

$$g_1(x) = \frac{1}{2}\sum_i e_i^2 (f_i^{\rightrightarrows}(x) - f_i^{\rightleftarrows}(x)) \ , \tag{2.30}$$

where the arrows denote parallel and anti-parallel orientation of the parton spin with respect to the nucleon spin. The spin structure function $g_2(x)$ vanishes in this model[4].

The cross section difference can be calculated using the lepton and hadron tensors expressed in terms of the structure functions:

$$\frac{d^2\sigma(\alpha) - d^2\sigma(\pi+\alpha)}{dx dy d\phi} = \tag{2.31}$$

$$\frac{e^4}{4\pi^2 Q^2}\left\{ \cos\alpha \left[\left(\frac{4 - 2y - y^2(4\frac{M^2x^2}{Q^2})}{4} \right) g_1(x,Q^2) - \frac{y}{2}\left(4\frac{M^2x^2}{Q^2}\right) g_2(x,Q^2) \right] \right.$$

[4]in the scaling limit no helicity flip of the nucleon is possible since $Q^2 \to \infty \gg M^2$ and $MG_1 + \nu G_2$ is similar to an helicity flipping amplitude, hence in the scaling limit G_2 must be negligible since $\nu \to \infty$ (see [Lea82] page 254 ff).

$$-\sin\alpha\cos\phi\sqrt{(4\frac{M^2x^2}{Q^2})\left(\frac{4-4y-y^2(4\frac{M^2x^2}{Q^2})}{4}\right)}\left(\frac{y}{2}g_1(x,Q^2)+g_2(x,Q^2)\right)\Bigg\} .$$

Experimental Determination of g_1

With longitudinal beam and target polarization the experimentally measured asymmetry $A_{||}$ is:

$$A_{||} = \frac{\sigma^{\overset{\rightarrow}{\Leftarrow}} - \sigma^{\overset{\rightarrow}{\Rightarrow}}}{\sigma^{\overset{\rightarrow}{\Leftarrow}} + \sigma^{\overset{\rightarrow}{\Rightarrow}}} , \tag{2.32}$$

and with a transversely polarized target:

$$A_{\perp} = \frac{\sigma^{\rightarrow\Uparrow} - \sigma^{\rightarrow\Downarrow}}{\sigma^{\rightarrow\Uparrow} + \sigma^{\rightarrow\Downarrow}} . \tag{2.33}$$

Since the polarization of the exchanged virtual photon is not exactly the same as for the incoming lepton, these two measured asymmetries have to be corrected [Dür95]:

$$\begin{aligned} A_{||} &= D(A_1 + \eta A_2) , \\ A_{\perp} &= d(A_2 - \xi A_1) , \end{aligned} \tag{2.34}$$

with the kinematical factors:

$$D = \frac{y(2-y)}{y^2 + 2(1-y)(1+R)} , \tag{2.35}$$

$$\eta = \frac{4\frac{Mx}{Q}(1-y)}{2-y} , \tag{2.36}$$

$$d = D\sqrt{\frac{2\epsilon}{1+\epsilon}} , \tag{2.37}$$

$$\xi = \eta\frac{1+\epsilon}{2\epsilon} , \tag{2.38}$$

$$\epsilon = \frac{1-y}{1-y+y^2/2} . \tag{2.39}$$

The virtual Compton scattering asymmetries $A_{1/2}$ are related to the polarized $g_{1/2}(x)$ and the unpolarized structure function $F_1(x)$ through:

$$\begin{aligned} A_1 &= \frac{g_1 - 4\frac{M^2x^2}{Q^2}g_2}{F_1} , \\ A_2 &= 2\frac{Mx}{Q}\frac{g_1+g_2}{F_1} . \end{aligned} \tag{2.40}$$

Since $g_2(x)$ is expected to be very small and suppressed by $4\frac{M^2x^2}{Q^2}$ and A_2 in equation 2.34 is also suppressed by the same factor, the structure function $g_1(x)$ can be determined using $A_{||}$, F_2 and R:

$$g_1 \approx \frac{A_{||}}{D} F_2 \frac{1 + 4\frac{M^2x^2}{Q^2}}{2x(1+R)} . \tag{2.41}$$

Figure 2.3 shows the world data on g_1 (as of December 1995) for the proton and neutron not including the preliminary HERMES measurement. A compilation of the world data

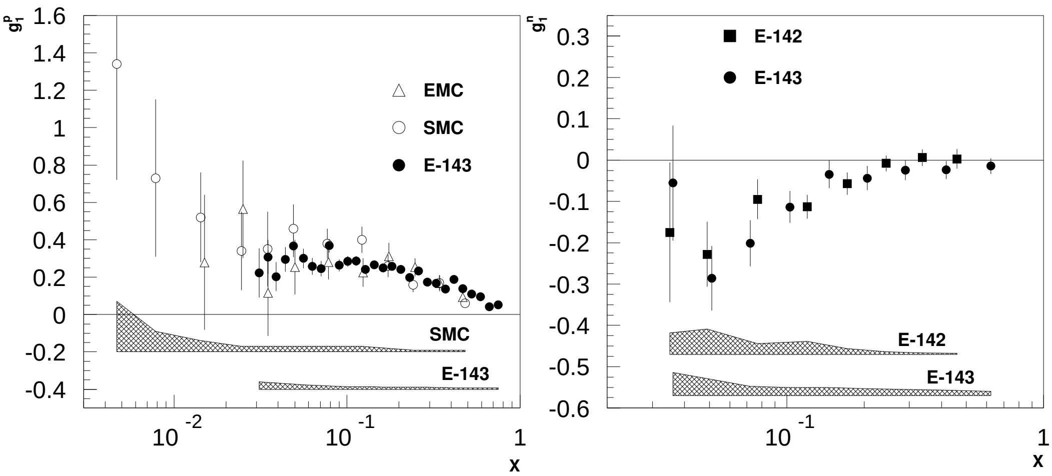

Figure 2.3: World data on g_1^{p} and g_1^{n} (as of 1995, from [Dür95]).

and the extraction of the contribution of the quarks to the spin of the nucleon yields about 27% [Ell95].

2.3 Semi-Inclusive DIS

The unpolarized and polarized structure functions measure integrals of parton and spin distributions in the nucleon. To obtain information on contributions of different partons separately one has to determine the type of the struck parton. Restricting the case to quarks as partons this means that one has to measure the flavor of the struck quark. This additional information on the DIS process can be retrieved by detecting hadrons produced in the scattering process. The basic assumption behind this idea is that the measured hadron reflects the flavor of the struck quark. The struck quark has to recombine into a hadron, therefore it has to pick up at least one anti-quark from the color field. Figure 2.4

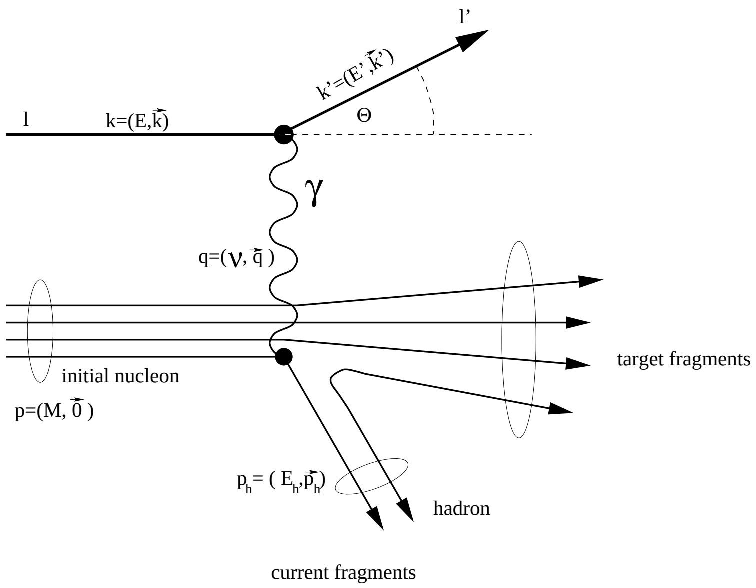

Figure 2.4: Semi-inclusive DIS scattering in the one photon exchange picture.

presents the semi-inclusive DIS process. In the leading order QPM only one parton is involved in the scattering process. The resulting hadron is assumed to carry most of the energy of the virtual photon and predominantly reflects its direction.

The probability for a quark of flavor i fragmenting into a hadron h is described by the fragmentation functions $D_i^h(z, Q^2)$, where z is the fractional energy of the hadron:

$$z = \frac{E_h}{\nu} \ . \tag{2.42}$$

This process is assumed to be independent of the absorption of the photon by the quark (*factorization*). Assuming that scaling holds also for the fragmentation functions, the semi-inclusive cross section for production of a hadron h on a nucleon N is then given by:

$$\frac{1}{\sigma_{tot}} \frac{d\sigma_{\mathrm{N}}^h(x, z)}{dz} = \frac{\sum_i e_i^2 f_{i/\mathrm{N}}(x) D_i^h(z)}{\sum_i e_i^2 f_{i/\mathrm{N}}(x)} \ . \tag{2.43}$$

Provided the fragmentation functions are known, the distribution functions $f_{i/N}(x)$ can be separately determined by the experiment. The most important question is how to separate the flavor reflecting hadron from the target remnants. An experimentally measured hadron can either come from the fragmentation process of the struck quark (*"current fragmentation region"*), or from the target fragments (*"target fragmentation region"*). Provided the struck quark has a large enough momentum these two regions separate in the measured z and the fractional longitudinal momentum x_{F} (*"x-Feynman"*):

$$x_{\mathrm{F}} = \frac{2p_l}{W} \ , \tag{2.44}$$

with p_l being the longitudinal momentum of the hadron with respect to the virtual photon momentum q. The larger z is, the higher the probability that the hadron contains the flavor of the struck quark, whereas a positive x_{F} is measured for those hadrons and negative for the target remnants[5].

The fragmentation functions $D_i^{\pi^\pm}$ for the light quarks of flavor i fragmenting into pions can be reduced to two different fragmentation functions D^+ and D^- using isospin and charge symmetry:

$$\begin{aligned} D^+(z) &= D_u^{\pi^+}(z) = D_d^{\pi^-}(z) = D_{\bar{d}}^{\pi^+}(z) = D_{\bar{u}}^{\pi^-}(z) \ , \\ D^-(z) &= D_d^{\pi^+}(z) = D_u^{\pi^-}(z) = D_{\bar{u}}^{\pi^+}(z) = D_{\bar{d}}^{\pi^-}(z) \ , \end{aligned} \tag{2.45}$$

which have been measured by the EMC.

In polarized semi-inclusive DIS the contribution to the nucleon spin of the different partons can thus be measured separately by comparing hadron rates for opposite spin states in different targets.

In the unpolarized case information on the different parton densities themselves can be extracted. In chapter 6 a first semi-inclusive analysis of the HERMES data is described.

2.4 Sum Rules

Since there is, as yet, no theory which is able to compute the x-dependent parton densities $f_i(x)$ the experimental data can only be compared to integrals whose values are predicted by theoretical models. These integrals or moments of the structure functions have the general form $M_{\mathrm{n}}(F) = \int dx\ x^{(n-1)} F(x)$. A few important sum rules are mentioned here:

The Gottfried Sum Rule

The 0^{th} moment for difference of the structure functions F_2 for lepton-nucleon scattering on protons and neutrons can be predicted under the assumption that the quark sea is flavor symmetric. As seen earlier the structure function can be expressed in terms of the valence and sea quarks like in equation 2.27. The integral over the quark distribution functions separately has to reflect the valence quark contents:

$$\int_0^1 u_v(x)dx = 2; \quad \int_0^1 d_v(x)dx = 1 \ . \tag{2.46}$$

According to these very basic assumptions the Gottfried sum rule [Got67] is:

$$S_G = \int_0^1 \frac{dx}{x}(F_2^{\mathrm{p}}(x) - F_2^{\mathrm{n}}(x)) = \frac{1}{3} \ . \tag{2.47}$$

[5]for a detailed discussion see [Ber87]

Current data from muon experiments at CERN (see [Arn94]) indicate a violation of this sum rule. A possible explanation of the defect in this sum rule is the sea quark flavor asymmetry. First results on the determination of the sea quark flavor asymmetry will be discussed in chapter 6.3.

The Bjørken Sum Rule

A similar sum rule for the difference of the spin structure functions $g_1(x)$ of the proton and neutron is their first moment, which can be predicted from fundamental QCD principles to be:

$$\int_0^1 dx\,(g_1^{\mathrm{p}}(x) - g_1^{\mathrm{n}}(x)) = \frac{1}{6}\left|\frac{g_{\mathrm{A}}}{g_{\mathrm{V}}}\right| + \text{(QCD-corrections)} = 0.21 + \text{(QCD-corrections)} \tag{2.48}$$

at $Q^2 = 10\ \mathrm{GeV}^2$. The Bjørken Sum Rule [Bjo66] is expressed in terms of fundamental quantities, g_A/g_V is the ratio of axial- and vector coupling in the weak neutron β-decay. This very fundamental sum rule has been supported by experiments at CERN and SLAC .

The Ellis-Jaffe Sum Rule

Another spin related sum rule is the Ellis-Jaffe sum rule which predicts the 0^{th} moment of $g_1(x)$ of the proton and neutron separately [Ell74]. Additional assumptions have to be made, namely the SU(3) flavor symmetry and the assumption that the strange sea is unpolarized:

$$\int_0^1 dx\, g_1^{\mathrm{p}}(x) = 0.185\ , \tag{2.49}$$

$$\int_0^1 dx\, g_1^{\mathrm{n}}(x) = -0.024\ . \tag{2.50}$$

First measurements at SLAC were in agreement with the predictions but suffering from large uncertainties. In 1987 the EMC published a new result on the Ellis-Jaffe sum rule for the proton. The value of $0.126 \pm 0.010 \pm 0.015$ is a significant deviation from the predicted value. This was a first hint that the simple picture that the nucleon spin is the quantum mechanical sum of only the three valence quark spins is not realized in nature. This measurement triggered a lot of efforts both on the theoretical and the experimental side to learn more about the other contributions to the nucleon spin. The HERMES experiment is the most recent experiment built to study this question.

2.5 Corrections

So far DIS has been idealized to the simple QPM picture. With increasing precision of experimental results deviations from this picture have been observed. On the one hand the QPM deals with ideal non-interacting partons which is a coarse simplification and on the other hand the nucleon is treated as a non interacting particle even if it is bound inside nuclei.

2.5.1 QCD Effects

The most severe simplification made is the assumption that the partons inside the nucleon are free and do not interact. The consequence of this assumption was the Q^2-independence of the parton distribution functions and hence the structure functions. At large Q^2 this picture has to be modified taking into account higher order effects like for example gluon radiation. Figure 2.5 shows two processes contribut-

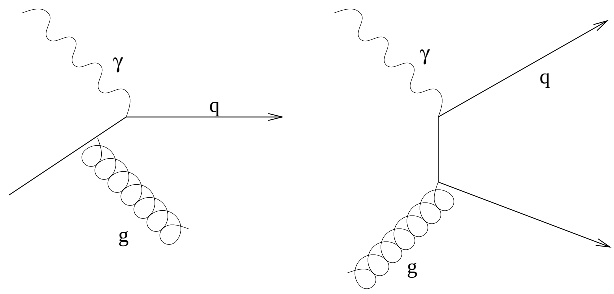

Figure 2.5: Higher order QCD processes, as example gluon Bremsstrahlung (left graph) and a gluon splitting into quarks (right graph).

ing in lowest order. To take these effects into account within the DIS framework introduced here the quark distribution functions have to be modified. The *Gribov-Lipatov-Altarelli-Parisi-equations* incorporate the corrections using splitting functions $P_{qq}(x/y),\ P_{qg}(x/y),\ P_{gq}(x/y),\ P_{gg}(x/y)$ which can be interpreted as the probability of finding a quark q or gluon g with momentum fraction x produced by a parton q or g with momentum fraction y. This means the Q^2-independent quark distribution functions of the QPM are replaced by Q^2-dependent distribution functions reflecting the interaction among the quarks and gluons:

$$\begin{aligned} \frac{df_i(x,Q^2)}{d\ln Q^2} &= \frac{\alpha_s(Q^2)}{2\pi}\int_x^1 \Big(f_i(y,Q^2)P_{qq}(x/y) + g(y,Q^2)P_{qg}(x/y)\Big)\frac{dy}{y}\,, \qquad (2.51) \\ \frac{dg(x,Q^2)}{d\ln Q^2} &= \frac{\alpha_s(Q^2)}{2\pi}\int_x^1 \left(\sum_i^{2n_f} f_i(y,Q^2)P_{gq}(x/y) + g(y,Q^2)P_{gg}(x/y)\right)\frac{dy}{y}\,, \end{aligned}$$

where $g(y,Q^2)$ is the gluon distribution function and the sum is over all quark and anti-quark flavors. As equation 2.51 shows the splitting is independent of the scattering process and in principle the DIS process can be described with the same formalism as introduced above only taking corrected distribution functions. A consequence is that partons in this picture have transverse momenta and the *Callan-Gross-Relation* (see equation 2.18) is no longer exactly valid since now also longitudinal photons contribute to the cross section. The structure functions become Q^2-dependent which is called *scaling violation* and can be expressed in terms of the new distribution functions and coefficient functions $C_i(x/y, \alpha_s(Q^2))$:

$$F_2(x, Q^2) = x \sum_{\text{flavours}} \int_x^1 f_i(y, Q^2) \times C_i(x/y, \alpha_s(Q^2)) \frac{dy}{y} , \tag{2.52}$$

where the sum is over quark, anti-quark flavors and the gluon distribution. The methods of calculating the coefficients for higher orders is beyond the scope of this work but measuring the Q^2-dependence of structure functions can prove perturbative QCD. Indeed, measurements of the Q^2-dependence of structure functions do agree well with the predictions and allow a determination of the strong coupling constant α_s.

2.5.2 Nuclear Effects

The assumption that the binding of the nucleons inside nuclei has no effect on DIS is based on the large energy difference of the two processes. As stated in the introduction the ratio of structure functions measured with different target nuclei deviates from unity. There are four x-regions of different deviations shown in figure 2.6:

Shadowing in the region of $x < 0.1$ the cross section is smaller for nucleons bound in nuclei than the expected sum of the nucleon cross sections. This region is called *shadowing-region* because one describes the effect as a shadowing of the inner nucleons by the nucleons on the surface of nuclei. The *vector-meson dominance model* VDM can explain the effect. Photons can fluctuate into vector mesons like the ρ-meson conserving the quantum numbers ($J^{PC} = 1^{--}$). This hadronic component of the photon has a much smaller interaction length in a nuclear medium so that shadowing becomes large.

Anti-shadowing in the region of $x \approx 0.1 - 0.2$ denotes the enhancement of the cross section per nucleon inside nuclei. There is no commonly agreed explanation of this effect and the data are not conclusive.

EMC-effect is a decrease of the structure function ratio at $x \approx 0.3 - 0.7$. This decrease is commonly explained with rescaling models. These models re-scale either $x = \frac{Q^2}{2M\nu}$ because the effective mass M is lower for bound nucleons or Q^2 because the radius of bound nucleons R_{N} is larger and hence the width of the Fermi-motion of the valence quarks $\delta x \sim \frac{1}{R_{\mathrm{N}} m_{\mathrm{q}}}$ becomes smaller.

Fermi-motion describes the increase of the structure function for bound nucleons at large x ($x > 0.7$) due to their Fermi-motion inside the nuclei.

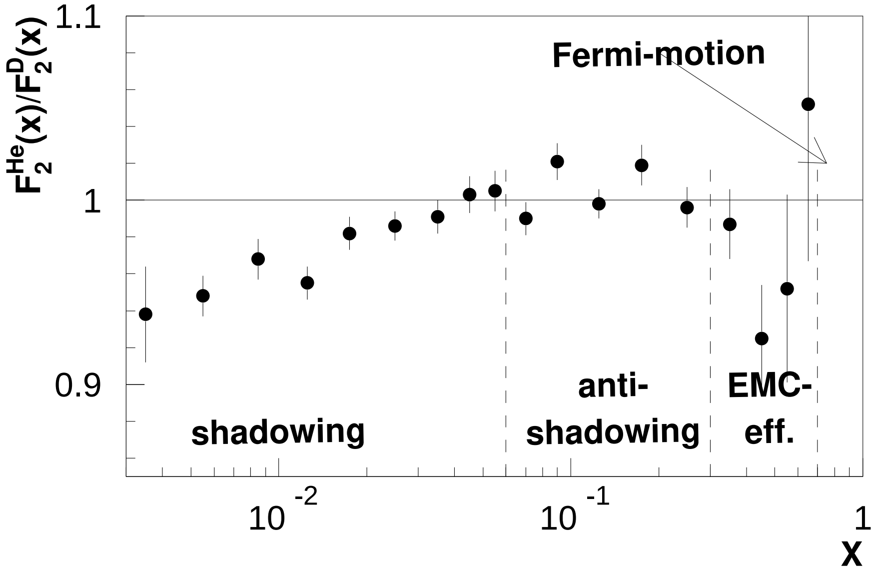

Figure 2.6: Nuclear effects in structure function ratios. The structure function ratio $F_2^{4\mathrm{He}}/F_2^{\mathrm{D}}$ is shown as measured by the NMC [Ama95] Shown are the four different x-regions described in the text.

All these nuclear effects have been observed for several nuclei and much theoretical effort went into the explanation of the effects and their dependence on Q^2 and the mass of the nucleus.

2.6 The HERMES Scope

In 1995 the main goal of HERMES has been to measure the spin structure function $g_1(x)$ of the neutron using a polarized $^3\mathrm{He}$ -target. The $^3\mathrm{He}$ atom is predominantly in an S-state with the spin of the two protons anti-parallel. In the first approximation the spin of the nucleus is dominated by the neutron spin. The deviations from a pure S-state results in a small proton polarization $P_{\mathrm{p}}^{^3\mathrm{He}}$ and a reduced neutron polarization $P_{\mathrm{n}}^{^3\mathrm{He}}$ (see [Cio93]):

$$P_{\mathrm{n}}^{^3\mathrm{He}} = 0.86 \pm 0.02 \quad , P_{\mathrm{p}}^{^3\mathrm{He}} = 0.028 \pm 0.003 \; . \tag{2.53}$$

To obtain the asymmetry A_1^{n} for the neutron from the measured asymmetry $A_1^{^3\mathrm{He}}$ for $^3\mathrm{He}$ the unpolarized structure functions for $^3\mathrm{He}$, the proton and the neutron are used:

$$A_1^{\mathrm{n}} = \frac{A_1^{^3\mathrm{He}} - \frac{2F_2^{\mathrm{p}}}{3F_2^{^3\mathrm{He}}} P_{\mathrm{p}}^{^3\mathrm{He}} A_1^{\mathrm{p}}}{\frac{F_2^{\mathrm{n}}}{3F_2^{^3\mathrm{He}}} P_{\mathrm{n}}^{^3\mathrm{He}}} \; . \tag{2.54}$$

As stated above A_1^{p} has been measured previously as well as the unpolarized structure function ratio $F_2^{\mathrm{n}}/F_2^{\mathrm{p}}$. The ${}^3\mathrm{He}$ structure function can be approximated by

$$F_2^{^3\mathrm{He}} = \frac{1}{3}(2F_2^{\mathrm{p}} + F_2^{\mathrm{n}}) \ . \tag{2.55}$$

This approximation assumes ${}^3\mathrm{He}$ to be the incoherent sum of two protons and a neutron; since the binding energy is very small compared to Q^2 one naively expects no influence of the binding of the nucleons in the nucleus in DIS. As stated in the previous section this is only an approximation and nuclear effects have to be taken into account. This can be done since the structure functions for ${}^4\mathrm{He}$ and deuterium are measured and an extrapolation for ${}^3\mathrm{He}$ can be used.

However HERMES has the possibility to measure the ratio $F_2^{\mathrm{n}}/F_2^{\mathrm{p}}$ and $F_2^{^3\mathrm{He}}/F_2^{D}$. For this purpose in 1995 data have been taken with unpolarized hydrogen and deuterium targets from which the ratio $F_2^{\mathrm{n}}/F_2^{\mathrm{p}}$ is deduced (see chapter 5). To extract the ratio $F_2^{^3\mathrm{He}}/F_2^{D}$ the polarized ${}^3\mathrm{He}$ data are spin averaged.

In addition the data taken with unpolarized targets give further insight into the structure of the nucleon by analyzing the semi-inclusive cross section. In chapter 6 first results on semi-inclusive physics are presented.

Chapter 3

The HERMES Experiment

The HERMES experiment has been designed to measure spin structure functions of the nucleons with high systematic and statistical precision. A figure of merit can be defined with all parameters entering the error of the measured asymmetry except those depending on the spectrometer (e.g. efficiencies and resolution):

- the longitudinal beam polarization P_{b},
- the target polarization (longitudinal or transverse) P_{t},
- the target dilution factor (polarizable nucleons in the target) f,
- the target density n,
- the beam current I and finally
- the total running time t.

The figure of merit

$$F = \sqrt{nIt}\; P_{\mathrm{b}} P_{\mathrm{t}} f \tag{3.1}$$

has to be maximized to increase the precision of the measurement. The first term describes the pure statistical precision. The second one is directly proportional to the size of the measured asymmetry and enters the error of the measurement linearly. Accordingly the total integrated luminosity and moreover the polarization of both, beam and target have to be maximized.

To fulfill these requirements the HERMES experiment uses polarized gas targets which are installed in the HERA electron/positron storage ring with its high currents and high beam polarization. In order to enhance the thickness the target gas is injected into a windowless, T-shaped aluminum tube, the so called *storage cell*.

HERA is the first high energy electron storage ring to achieve longitudinal electron polarization. The Sokolov-Ternov effect produces transverse electron polarization due to a small asymmetric spin flip amplitude in synchrotron radiation[Sok64]. The beam polarization grows asymptotically with a time constant of approximately 30 min at the HERA beam energy of 27 GeV. Since the experiment requires longitudinal beam polarization (see section 2.2.3) two spin rotators are mounted in front of and behind the HERMES experiment rotating the spin into the longitudinal direction and back. This is schematically shown in figure 3.1.

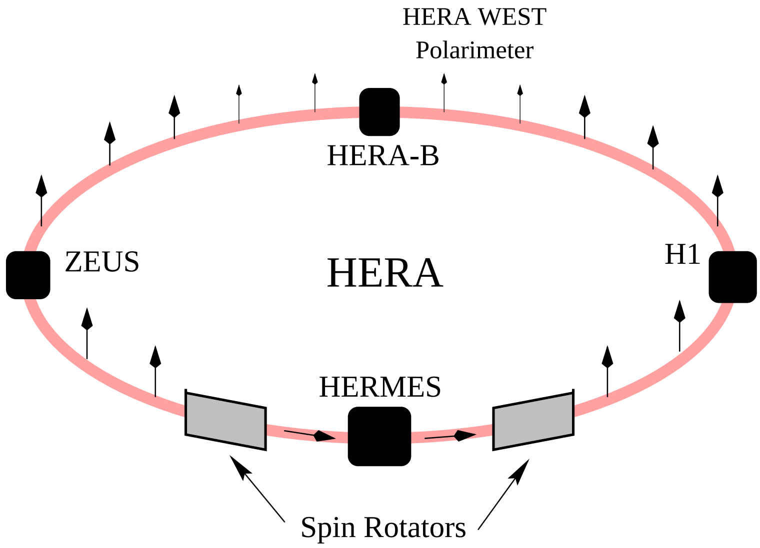

Figure 3.1: Schematical view of the HERA electron storage ring with its four experiments and the spin rotators at the HERMES interaction point, the arrows denote the spin direction of the electron beam.

The spin rotators were installed and tested in 1994. The measured transverse polarization exceeded 60 % [Bar95]. During the 1995 data taking the polarization was typically around 50 %. The longitudinal polarization can only be measured with a new polarimeter which is presently being installed in the HERMES region. However, since a stable spin tune in the HERA machine requires a perfect spin flip of both rotators compensating any net effect, the longitudinal polarization is expected to be the same as the transverse.

The interaction region in the HERA East Hall was modified to accommodate the HERMES requirements:

- The electron and proton beam line were separated by 72 cm horizontally.
- The space between the inner quadrupole magnets was enlarged to ± 8.5 m around the interaction point for the HERMES spectrometer and target.
- To minimize the synchrotron radiation hitting the HERMES target the electron beam line was straightened out over ± 90 m around the interaction point in addition

- a strong (2.6 mrad at ± 89 m) and a weak bend (0.5 mrad at ± 38 m) were installed to minimize synchrotron radiation in the HERMES region.

These changes and the installation of the spin rotators changed the optics of both the proton and electron machine. At the HERMES interaction region the β-function is adjusted to 3.0 m horizontally and 1.1 m vertically at low dispersion. This results in a small beam cross section which is crucial for the storage cell, since the target thickness is inverse proportional to the storage cell cross section and hence this cross section has to be minimized requiring a small beam cross section.

The target is mounted at the interaction point with the spectrometer installed in the downstream electron beam direction. HERMES uses polarized $^3\mathrm{He}$, hydrogen and deuterium gas targets. One of the unique and very important features of the HERMES experiment is its novel target technique. Instead of solid targets containing mixtures of polarized and unpolarized materials, introducing a high dilution and suffering from a rather long spin flipping time, HERMES uses highly polarized, windowless gas targets. These targets have no dilution and the spin can be flipped rapidly into any direction reducing systematic uncertainties. In addition this technology minimizes the multiple scattering of particles going into the acceptance of the spectrometer and hence improves the resolution.

3.1 The Test-Experiment

To study the impact of an internal gas target on the electron beam and the operating conditions of prototype detectors a test-experiment was installed in the HERA east section in 1994. An unpolarized internal gas target consisting of a storage cell, a gas feed system, the complete vacuum system and the final collimator system were installed into the modified electron beam line in the HERMES experimental region. Prototype versions of the major HERMES detector components were set up and tested under beam conditions.

The following sections introduce the basic setup of the target region including the collimator and vacuum system for the test-experiment. The basic design is the same as the one used for the 1995 data taking period. The results concerning beam-target interactions presented here are the combined experience of the 1994 test-experiment and the 1995 running period.

3.1.1 The Target

The HERMES gas targets make use of the storage cell technique to enhance the target thickness and hence the statistical precision of the measurements. Due to the limited intensities of the polarized target sources a simple atomic beam target cannot achieve the desired luminosities. Injecting the gas into a windowless storage cell raises the thickness by two orders of magnitude at a fixed flow rate[Hae85, Zap95a].

For the test-experiment a gas feed system providing three different gases: $^4\mathrm{He}$, nitrogen and hydrogen was installed. The gas flows from the manifold through an adjustable conductance into the storage cell.

The storage cell is a T-shaped aluminum tube as indicated in figure 3.2 with a wall thickness of 0.125 mm. It is 400 mm long and has an elliptical cross section of 30×10 mm. The storage cell acts as an impedance to the target gas while the stored electron beam passes the cell without interference. The resulting target density is triangular along the storage cell as indicated by the reconstructed vertex in figure 3.2.

During the test-experiment in 1994 the storage cell was not cooled. For the final $^3\mathrm{He}$ target the cell is cooled down to 20 K, for hydrogen and deuterium to 100 K by flowing

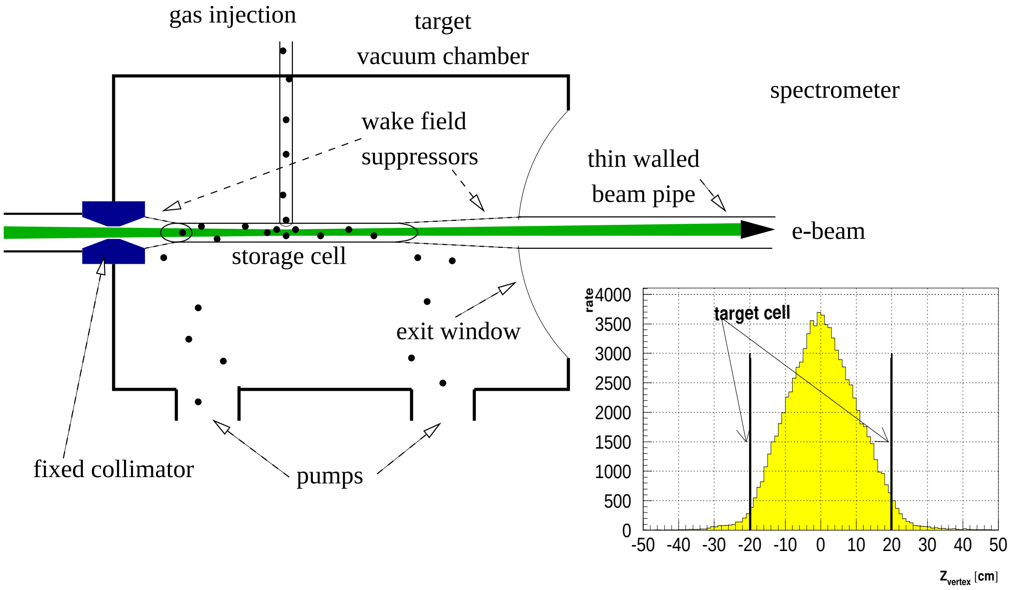

Figure 3.2: Schematical side view of the target chamber with storage cell, the resulting target density and hence the reconstructed vertex position is triangular.

cold $^4\mathrm{He}$ gas through the mounting rails of the storage cell. This slows down the gas atoms during wall bouncings and thus increase the time they stay in the cell.

There are two effects that can potentially warm up and destroy the storage cell [Zap95]:

The wake fields of short electron beam bunches of high intensity can lead to RF losses in the target chamber and thus heat up the storage cell. To avoid such losses the cross sections of the vacuum chambers along the beam are varied as smoothly as possible by using wake field suppressors; in the target chamber meshes made out of 0.125 mm thin titanium serve as electrical transition from the beam pipe cross section to the storage cell. They minimize the RF losses, ensure a good thermal isolation of the cell and still allow pumping out the target gas.

The synchrotron light generated by the electron beam passing the dipole magnets upstream of the HERMES interaction region is minimized by the beam line modifications mentioned above. In addition two movable and one fixed tungsten collimator prevent direct and single scattered photons from hitting the storage cell.

Without the collimator system about 100 W of synchrotron light would be incident on the storage cell [Dür91], in addition a huge amount ($10^{13} - 10^{14}$ Hz) of soft synchrotron photons would be scattered into the acceptance of the spectrometer, so that the wire chambers could not be operated. A set of two movable collimator pairs (C1) is mounted 2.1 m and 1.7 m upstream of the interaction point. They are made of 12 cm tungsten blocks with elliptical openings corresponding to the beam profile at the HERMES interaction point (see appendix A figure A.1 for details). A fixed collimator (C2) is installed directly in front of the storage cell which is the smallest fixed aperture in the HERA electron/positron ring. All collimator openings are tapered to reduce edge scattering.

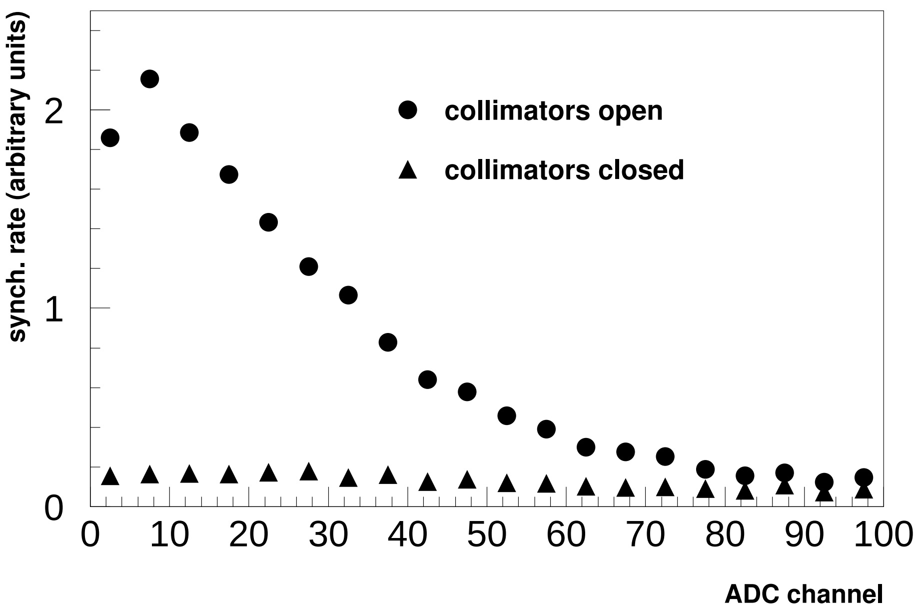

Figure 3.3: Synchrotron rate with opened and closed collimators, the remaining rate with closed collimators is mostly due to charged particle background.

During the test-experiment a silicon surface barrier detector (SSBD) with two scintillator fingers behind it was used to confirm the anticipated performance of the collimators (see appendix A figures A.3 and A.4). Figure 3.3 shows a comparison of the synchrotron rate behind the exit window for opened and closed collimators. The rate is measured by the silicon surface barrier detector in anti-coincidence with two scintillator fingers behind the active area. Charged particles cause a signal in the scintillator fingers and are vetoed out. Since these fingers did not cover the entire active area of the silicon detector a charged particle background remains in the measured spectra. The measurements indicate a large suppression of synchrotron light by closing the collimators especially in the region close to the beam pipe, whereas no reduction has been observed for angles larger than 100 mrad.

The synchrotron rate monitor was used to optimize the movable collimator settings. Moving the collimators into the position closest to the beam resulted in a maximum shielding of synchrotron light without any effect on the stored beam. The test-experiment as well as the 1995 operation showed that to optimize the background conditions the collimators had to be moved to a position where the synchrotron light and the charged particle rates were low enough to operate the wire chambers. The charged background originating from scraping of the beam halo at the collimators increased as the collimators were closed. This effect depends on the beam optics and in the 1995 beam tuning procedure flattening the beam upstream (> 39 m) resulted in a decrease of charged particles rates from scraping. In addition a further reduction of synchrotron rate was observed by careful adjustment of the beam upstream of the HERMES interaction region, centering it in all magnets. Since the beam optics for 1995 was not finalized during the test-experiment, this optimization procedure was done in 1995 at the beginning of each HERA fill.

Even with closed collimators the leakage current in the chambers during the test-experiment was too high to operate them at their design settings so a 4 mm lead curtain covering the acceptance of the chambers was set up upstream of the target. This reduced the leakage current of the chambers, which is a measure for the amount of ionizing particles passing the active area of the chamber. For the 1995 running a lead wall covering the complete tunnel cross section was set up to shield the experiment from synchrotron light out of the HERA tunnel [Pat94].

During the test-experiment, with the cell at room temperature, no changes of the cell temperature were observed. Figure 3.4 shows the storage cell temperature as measured in 1995 by temperature sensors attached to the cryogenic mounting rails of the storage cell during the filling procedure of the HERA positron ring. In 1995 the cell was cooled down to about 20 K and during filling and ramping of the HERA positron ring a slight increase of the temperature by a few degrees was observed.

Since the temperature falls off to its original value after ramping of the beam to it's full energy, the rise cannot be explained with synchrotron light heating up the cell. Instead this should cause a dramatic temperature rise when ramping the beam energy. The most probable cause is short range wake fields induced by *"long"* positron bunches or displacements during the injection phase which disappear after ramping since the bunch length decreases with the energy increasing. The lower plot in figure 3.4 shows also the

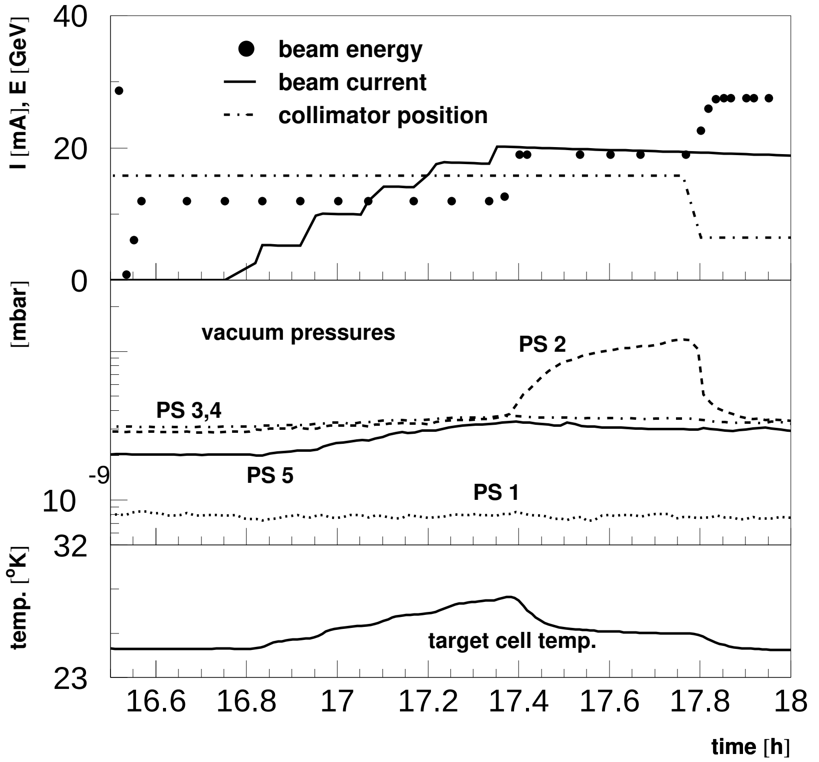

Figure 3.4: Target cell temperature and pressure during the filling of the HERA positron ring. The upper plot shows the beam current (solid line) and the beam energy (dots). The ramping of the energy for this fill occurred in two steps, during the second step the collimators (C1, C2) were closed. The middle plot shows the pressures measured along the beam line (PS1-5). At PS2 a slight increase of the pressure is observed. The pressure drops again once the collimators are closed. The lower plot shows the storage cell temperature rising proportional to the square of the beam current due to wake fields depositing energy which completely recovers once the beam energy reaches its maximum.

pressure in the beam line around the HERMES target. Before the collimators are closed, synchrotron light hits the limiting apertures, the fixed collimator C2 and the TOM mirror described in section 3.2 upstream of the target. This results in a pressure rise in this region (PS2-pressure) due to bake out of the material close to the beam. As soon as the collimators are closed the pressure drops back to the original value [Zap96].

3.1.2 The Vacuum System

The vacuum system installed during the test-experiment in 1994 only changed in minor technical details in 1995. It has to ensure that the target gas is entirely pumped out of the beam line since HERMES runs in parallel to the other experiments at HERA.

Especially for unpolarized targets, where there is no source limitation on the target thickness, the positron lifetime is the limiting factor for the achievable luminosity for HERMES. The internal target reduces this lifetime via beam losses due to atomic Bremsstrahlung. The lifetime $\tau_{\rm gas}$ of the stored positron beam due to the HERMES target depends on the target thickness n and the charge Z of the gas atoms [HER93]:

$$\tau_{\rm gas}(Z,n) \sim \frac{1}{\ln\{\frac{183}{Z^{1/3}}\}} \frac{1}{Z(Z+1)} \frac{1}{n}. \tag{3.2}$$

The actual lifetime τ depends on the beam lifetime without the HERMES target $\tau_{\rm beam}$ and the target related lifetime $\tau_{\rm gas}$ via:

$$\frac{1}{\tau} = \frac{1}{\tau_{\rm gas}} + \frac{1}{\tau_{\rm beam}}. \tag{3.3}$$

Figure 3.5 shows the dependence of the HERA positron beam lifetime on the HERMES target. With the simple unpolarized gas feed system which was used in the test-experiment the beam lifetime was measured for different target thicknesses. The data are in good agreement with the calculations based on atomic bremsstrahlung.

Figure 3.2 shows a schematic side view of the target chamber. The electron beam passes the fixed collimator (C2) and enters the target vacuum chamber traversing the gas target trough the storage cell. Scattered particles leave the target chamber passing the storage cell and a 0.3 mm thin stainless steel exit window. The target gas is pumped out of the storage cell and target chamber by two turbo pumps attached to the chamber. Gas passing the collimator or the thin walled beam pipe is pumped out of the HERA ring by three additional vacuum pumps mounted upstream and downstream. The pressure in the beam line is measured above each of the five pump stands (PS1-5) with ion gauges. Taking all conductances and pumping speeds into account the expected pressure profile in the beam line around the HERMES target has been calculated. Figure 3.6 shows the measured pressure profiles for different target thicknesses. For the design target thickness of the $^3{\rm He}$ target of about $1.0 \times 10^{15}{\rm nucl./cm^2}$ the pressure in the beam line above the

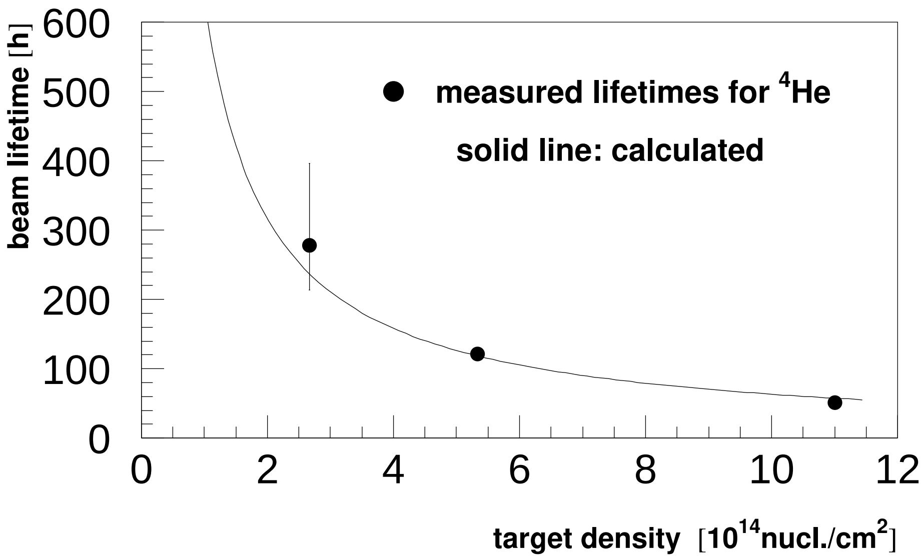

Figure 3.5: Measured and calculated HERA beam lifetime due to the HERMES target (for ^{4}He).

last downstream HERMES pump stand (PS5) does not rise significantly above the value without gas. The same is true for the first pump stand upstream. Only if the target thickness is increased significantly (factor 15) will the HERMES vacuum system not be able to maintain the base pressure at the transition to the machine vacuum.

3.1.3 Performance of Prototype Detectors

For the test-experiment prototype detectors were installed in the HERMES spectrometer region. No spectrometer magnet was present. The purpose of the test-experiment was to study the detector and trigger performance under realistic background conditions. The basic design of all prototype detectors is the same as for the final detectors except for their size and granularity. A detailed description of the basic detector design is given in section 3.3.

Figure 3.7 shows the event display of a reconstructed event for the test-experiment. Three prototype tracking chambers are used to reconstruct the track[1]:

1. a 10×10 cm^2 micros-trip gas chamber consisting of three planes with 512 wires with a spacing of 200 μm,

2. a 10×10 cm^2 drift chamber with six planes and a wire spacing of 15 mm and

[1]here only the differences with respect to the final detectors described in section 3.3 are listed

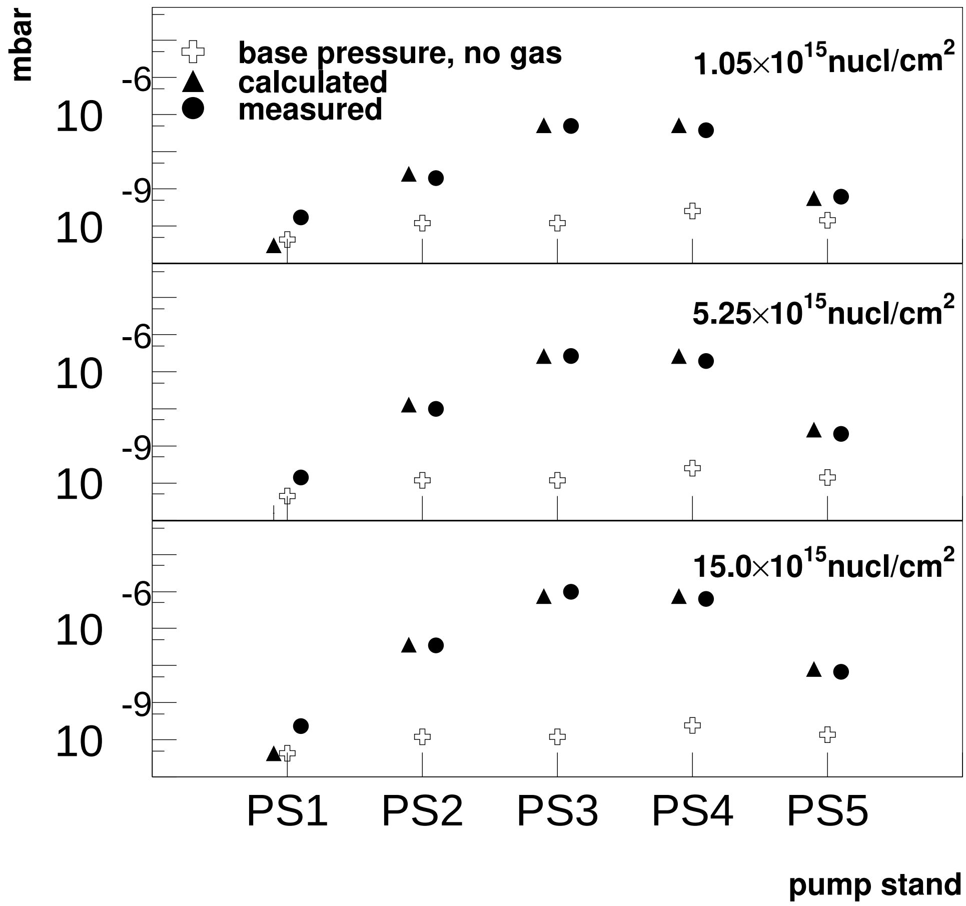

Figure 3.6: Pressure profile in the HERMES target region for three different target thicknesses ($^4\mathrm{He}$). The measured and calculated pressures are compared with the base pressure without target gas.

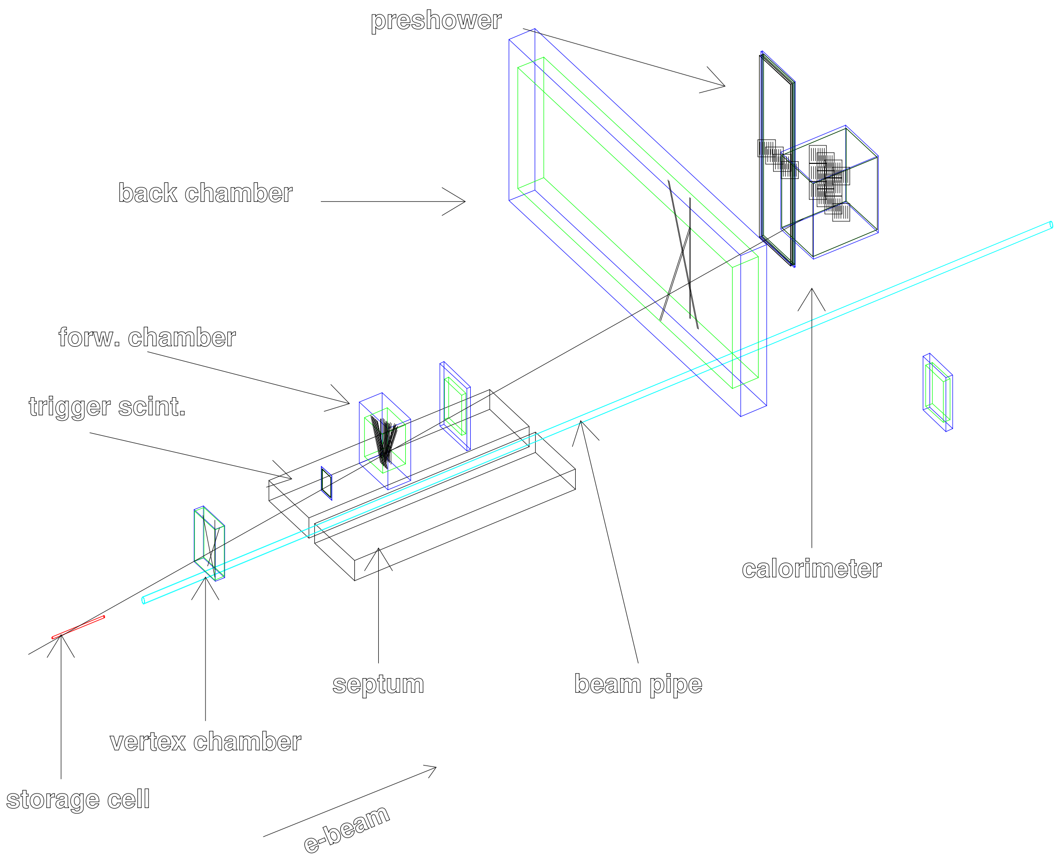

Figure 3.7: A reconstructed test-experiment event showing hits in the prototype detectors.

3. a large ($190 \times 50\ \mathrm{cm}^2$) drift chamber prototype with three planes and a wire spacing of 10 mm.

All chambers have an x-, u- and v-plane with wires oriented 0, -30 and 30 degrees with respect to the vertical direction. The reconstruction was done with the HERMES reconstruction program with the test-experiment geometry in the same way as it is done in the analysis of the 1995 data described in chapter 4.

A prototype of the calorimeter consisting of a 4×4 matrix of lead glass blocks and a prototype of the preshower detector with four scintillator slabs and a 5 mm lead sheet in front were used to trigger DIS events. A signal in the calorimeter and preshower detector corresponding to an electron with momentum above 4 GeV was required in coincidence with a signal in the forward trigger scintillator and the HERA clock which is synchronized to the bunch crossing the interaction point.

After the installation of a 4 mm lead shielding upstream of the HERMES interaction point all prototype detectors could be operated and DIS events could be reconstructed. Optimization of the beam position resulted in a decrease of the leakage current in the prototype back chamber by a factor of 3.

In addition to the above mentioned prototype detectors several scintillators have been mounted downstream of the HERMES experiment to monitor the background originating from the proton beam. Behind the prototype calorimeter a 1.6 m concrete shielding was set up. In front of and behind the shielding scintillators monitored the proton background requiring coincident signals in all counters. A detailed description of the setup, the analysis and Monte Carlo studies is given in [Fie95]. Here only the results are summarized:

- The proton beam induced background originates from beam protons scattering of the residual gas in the proton beam pipe downstream of the HERMES experiment resulting in hadronic showers with high multiplicity. No evidence for protons scattering off beam pipe apertures was found.

- The absolute rate of proton background events is 50 Hz per 1 mA of stored proton beam current which is in agreement with Monte Carlo studies. These events are shifted in time with respect to the DIS events from the HERMES target, so that they do not cause a physics trigger.

- During injection the proton induced background increases due to beam losses but is tolerable in terms of radiation damage of the detectors.

- The 1.6 m concrete shielding reduces the low energetic part of the background by a factor of 5 but does not reduce the high energetic part close to the proton beam pipe.

Based on these results no shielding against the proton background was set up for the final experiment.

In summary, all prototype detectors could be operated satisfactory during the test-experiment. The analysis software was able to reconstruct DIS events with only minor changes to the software. No considerable radiation damage could be measured to any of the components used in the test experiment. The operation of the wire chambers improves with careful tuning of the beam position at the HERMES interaction region.

3.2 The Polarized $^3\mathrm{He}$ Target

In 1995 the polarized $^3\mathrm{He}$ target was installed at the HERMES interaction point [Pat95]. The simple gas feed system used during the test-experiment was replaced. Figure 3.8 shows a schematic view of the target. The $^3\mathrm{He}$ gas flows into a quartz pumping cell through a temperature controlled needle valve. The pressure at the entrance to the pumping cell is measured and fed back into the adjustable needle valve to stabilize the flow into the cell against changes of the pressure in the gas feed system. A precision capillary (C1) in front of the pumping cell and another at the exit (C2) are chosen to maintain a constant pressure of 0.67 mbar at a flow rate of 10^{17} $^3\mathrm{He}$ atoms/sec. A heater in the helium transfer line cooling the storage cell is used to fine-adjust the target density which is inverse proportional to the square root of the cell temperature.

A small fraction (10^{-6}) of the $^3\mathrm{He}$ atoms inside the pumping-cell are excited to the meta-stable 2^3S_1 state with a radio frequency discharge. This state is optically pumped to the $2^3P_{0,1,2}$ levels. Therefore circular polarized laser light at 1083 nm wave length along a weak magnetic field is used to polarize the $^3\mathrm{He}$ atoms via angular momentum transfer. Meta-stability exchange transitions transfer the polarization of this sample to the ground state atoms.

To maintain the nuclear polarization of the target gas atoms a magnetic field is provided by large Helmholz coils outside the target chamber. The magnetic field serves at the quantization axis for the spin of the nuclei.

A fast spin flip is obtained by reversing the circular polarization of the laser light. The buildup time for up to 55% polarization in the HERMES target is approximately 12 seconds. The spin orientation is reversed every 10 minutes.

To measure the polarization of the $^3\mathrm{He}$ atoms inside the pumping cell the circular polarization of the 667 nm $^3\mathrm{He}$ transition induced by the discharge is measured. The relation between the $^3\mathrm{He}$ polarization and the circular polarization of the 667 nm line was calibrated previously [Lee93].

An independent direct method to measure the target polarization of the $^3\mathrm{He}$ atoms inside the storage cell is provided by the Target Optical Monitor (TOM) (see figure 3.9 [Pit95]). The stored electron beam traversing the target gas excites atomic levels in the target gas via Coulomb interaction. The $^3\mathrm{He}$ atoms are excited into the 4^1D state with a lifetime of 37 ns. Via hyperfine coupling, which takes place in the order of 1-2 ns, the nuclear polarization is transferred to the electronic system resulting in circularly polarized

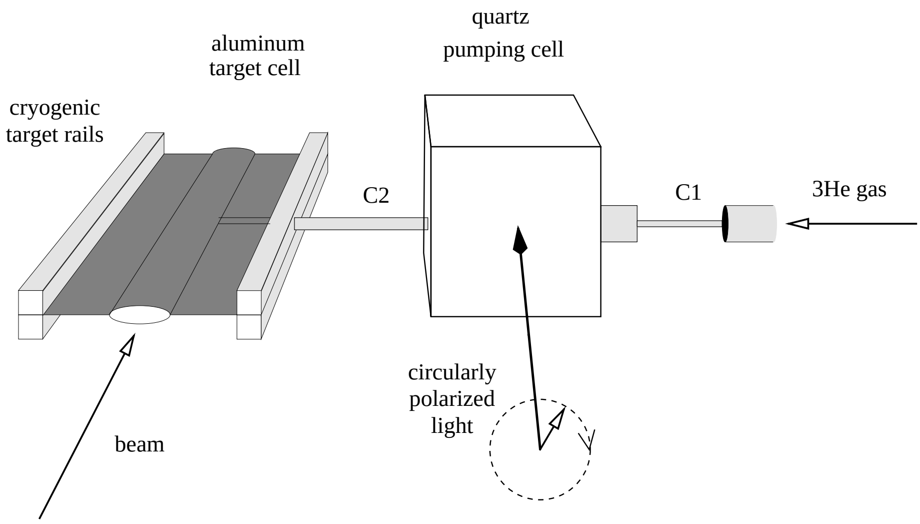

Figure 3.8: Schematical view of the polarized ^3He target with the gas inlet on the right side, the density regulating conductance C1 and the pumping cell. From the pumping cell the polarized gas enters the storage cell through C2.

light emitted on relaxation.

The degree of circular polarization is measured to determine the nuclear polarization. The emitted photons going upstream are deflected by a polished aluminum mirror and leave the vacuum system through a quartz vacuum window. They pass a lens focusing the target region and are reflected from a second mirror into a photo-tube. The second mirror is rotated by 90° relative to the first one to compensate the polarization phase shift. A rotating quarter wave plate and a fixed linear polarizer in front of the photo-tube measure the circular polarization of the light.

3.3 The Spectrometer

The HERMES spectrometer (see figure 3.10) is designed to detect scattered positrons from the target over a large kinematical range. Due to the fixed target and high beam energy the scattered particles are strongly forward peaked. With a maximum angular acceptance of ± 140 mrad vertically and ± 170 mrad horizontally the spectrometer detects scattered particles down to 0.4 GeV.

Both storage ring beam lines traverse the HERMES spectrometer. The detectors are each split into two symmetric parts mounted above and below the storage ring plane. The active area of the front detectors extends as close to the beam pipes as possible resulting in a minimum acceptance of 40 mrad.

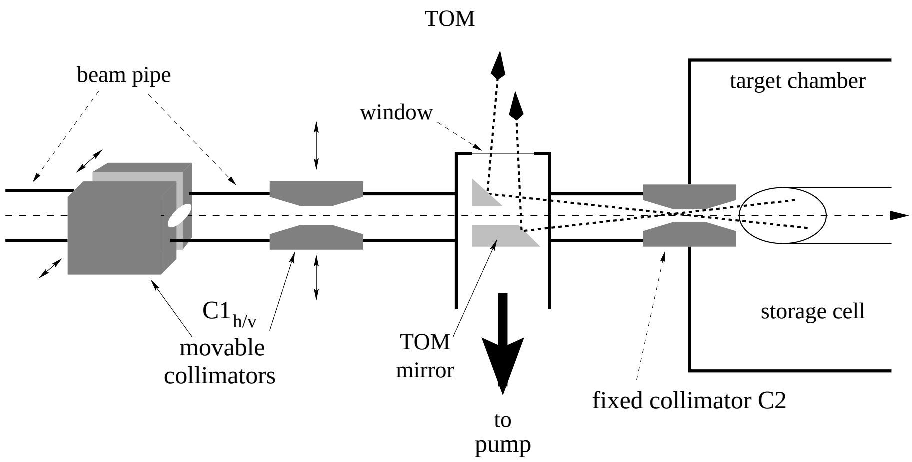

Figure 3.9: Schematical view of the upstream target area showing the TOM and the collimator setup.

3.3.1 The Tracking System

In order to measure particle momenta the tracks are determined in front of and behind a large spectrometer magnet. The dipole magnet provides an integrated field of 1.3 Tm in which particles are deflected according to their momenta. To keep distortions of the proton and positron beam due to this strong magnetic field low an iron septum plate is mounted in the horizontal plane housing the two beam tubes. In addition compensation magnets inside the septum plate keep the dipole field low. The front and back openings of the magnet are covered with field clamps to minimize stray fields in the detector regions.

The tracking detectors consists of different types of wire/micro-strip chambers. Each single plane of these chambers measures one out of three different coordinates in space which are tilted by 30^o. The horizontal coordinate denoted by x is measured with grids of vertical wires and two grids tilted by $\pm30^o$ measure the u- and v-coordinate. The tracking chambers cover three different regions (table 3.1 summarizes the technical parameters of all chambers):

Front Region

There are two different tracking chamber systems between the target and the spectrometer magnet, a micro-strip gas chamber called Vertex Chamber (VC) and a drift chamber called Front Chamber (FC) (see figure 3.11). The micro-strip gas chamber consists of two modules (VC1/2) with one plane for the u-, v- and x-direction respectively. Each plane is a 300 $\mu\mathrm{m}$ glass substrate covered with 7 $\mu\mathrm{m}$ wide aluminum anode strips. The spacing between the strips is 193 $\mu\mathrm{m}$. A 3 mm gap between the anodes and the cathode plane is filled with DME/CO_2 gas. The high voltage between the cathode and anode plane

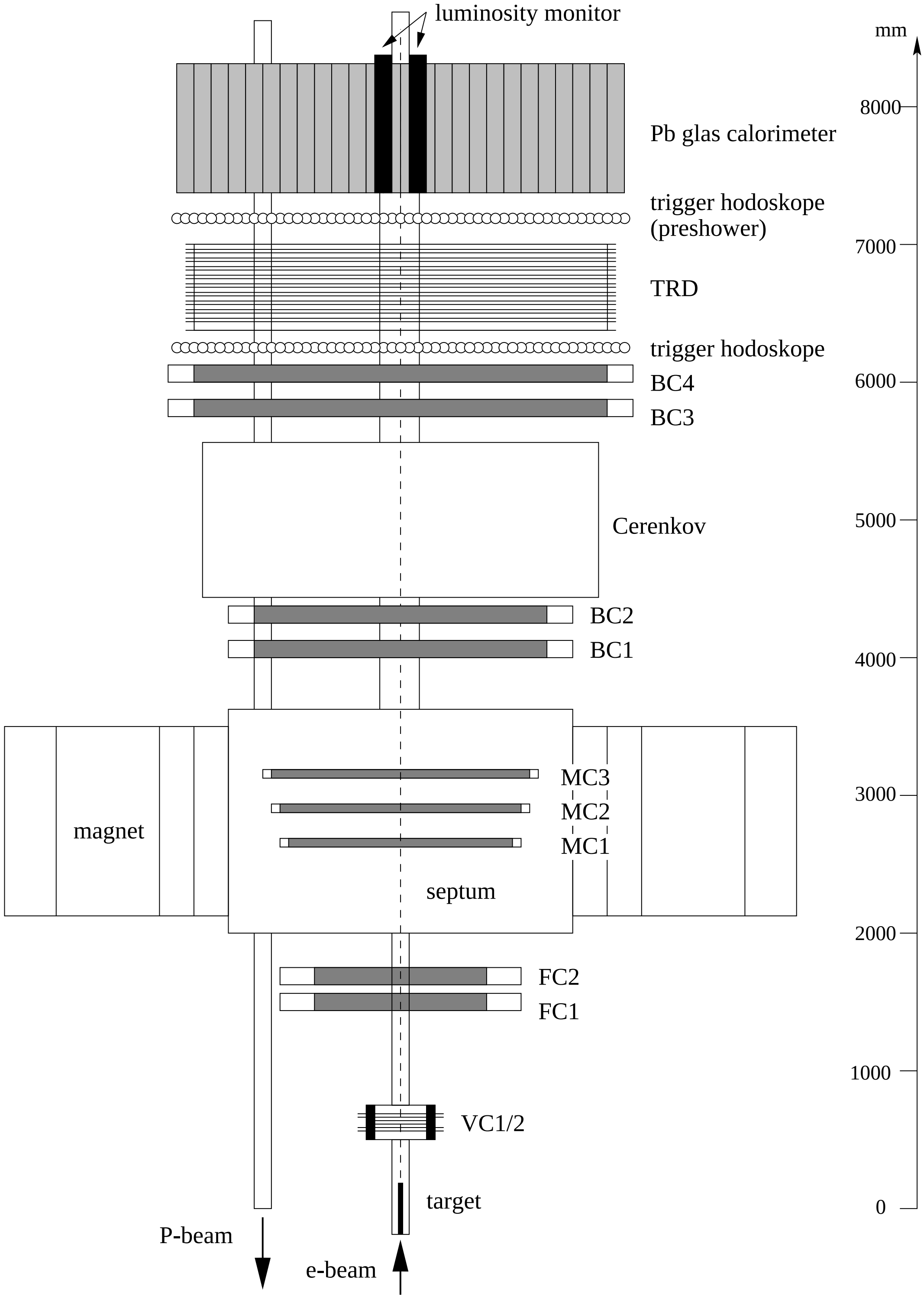

Figure 3.10: Top view of the HERMES spectrometer

accelerates atoms ionized by traversing particles. The charge of the resulting avalanche is measured with the anode strips resulting in a digital signal indicating if a particle went through the cell.

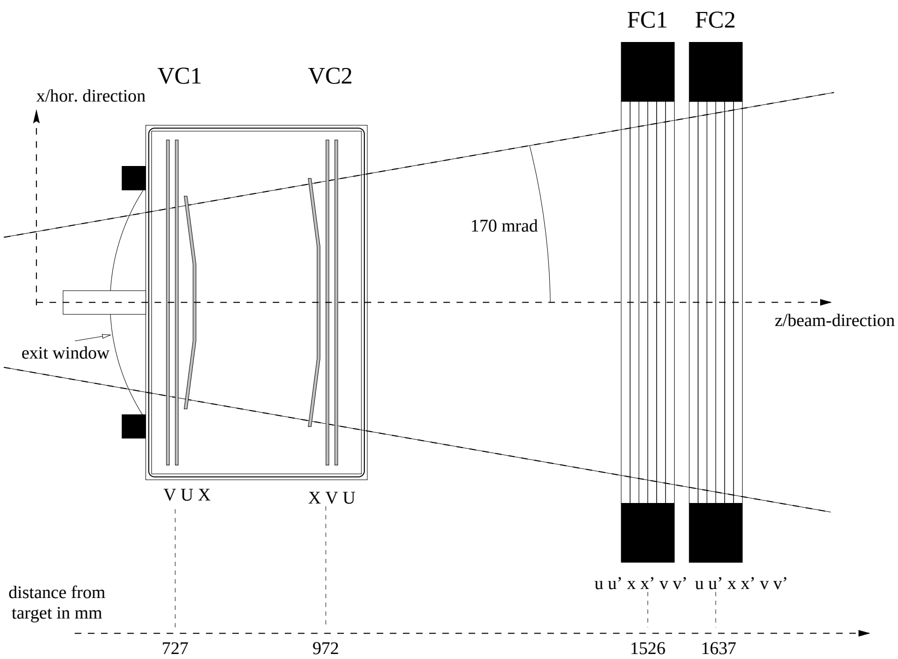

Figure 3.11: Top view on the front tracking detectors. The exit window of the target chamber is shown on the right with the VC housing directly downstream. The x-planes in the VC are tilted. The FC's are shown on the left with the maximum horizontal acceptance angle denoted by the dashed lines.

The front chambers consist of two modules of drift chambers. One module has 6 planes of sense/potential wires, two for each direction ($\mathrm{x}, \mathrm{x}', \mathrm{u}, \mathrm{u}', \mathrm{v}, \mathrm{v}'$) interleaved with cathode foils (aluminized mylar). The planes of one direction are staggered by half a cell size (3.5 mm). Between the sense wires there are potential wires producing a drift field for ionized gas atoms which results in an almost constant drift velocity over the entire cell size. The time between a pulse in the sense wires and a common stop signal is used to compute the position of a track traversing the drift cell.

The Magnet Chambers

Inside the magnet gap there are three proportional wire chambers called Magnet Chambers (MC1/2/3) each consisting of one x-, v- and u-plane. Each plane has two cathode foils and anode wires with a spacing of 2 mm in between yielding a resolution of 577 μm. The information of these chambers is used to match front and back tracks and resolve ambiguities.

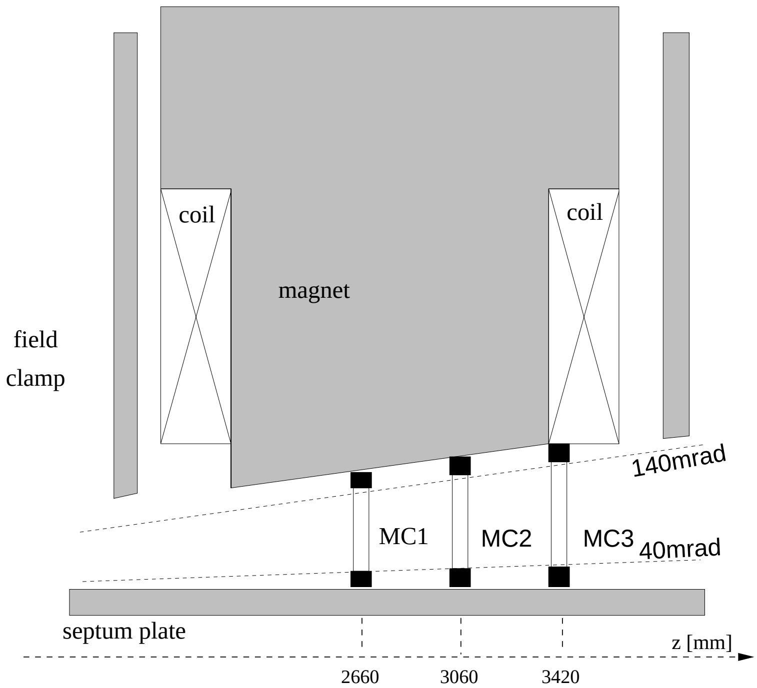

Figure 3.12: Side view of the upper magnet region with the magnet chambers. The upper part of the magnet with the coil is shown, in the space between the septum plate and the magnet the three MC's are mounted.

The Back Chambers

The Back Chambers (BC1-4) are drift chambers which are very similar to the FC's with a wire spacing of 15mm. There are two sets of chambers of different size (see figure 3.10); one behind the magnet, in front of the Cerenkov detector and one behind the Cerenkov, in front of the trigger hodoscope H1. The first set has an active area of 1880 $\times$ 520 mm and consists of two chambers with staggered $\mathrm{v}-\mathrm{v}', \mathrm{x}-\mathrm{x}'$ and $\mathrm{u}-\mathrm{u}'$ wire planes. The second set has an active area of 2890 $\times$ 710 mm. The spatial resolution was measured in a test setup and is below 150 $\mu\mathrm{m}$ under optimal conditions.

	Vertex		Front		Magnet			Back	
detector	VC-1	VC-2	FC-1	FC-2	MC-1	MC-2	MC-3	BC1/2	BC3/4
z-pos. (mm)	727	972	1526	1637	2655	3060	3423	4150	5900
active hor. (mm)	420	420	680	680	996	1216	1424	1888	2890
active vert. (mm)	137	145	220	220	263	306	347	520	710
type	micro-strip gas		hor. drift		proportional			hor. drift	
cell size	193 $\mu\mathrm{m}$		7 mm		2 mm			15 mm	
chamber gas	$\mathrm{DME/CO_2}$		$\mathrm{Ar\ CF_4\ CO_2}$		$\mathrm{Ar\ CF_4\ CO_2}$			$\mathrm{Ar\ CF_4\ CO_2}$	
gas mixing	60:40%		90:5:5%		65:5:30%			90:5:5%	
HV in Volt	2000		1400		2800			1750	
nominal resolution	45 – 56 $\mu\mathrm{m}$		150 $\mu\mathrm{m}$		460 – 570 $\mu\mathrm{m}$			150 $\mu\mathrm{m}$	
num. of planes	3	3	6	6	3	3	3	6+6	6+6
num. of wires (X)	1674	2046	96	96	496	608	720	120	192
num. of wires (U/V)	2170	2170	96	96	512	608	720	118	186
readout	digital (APC)		TDC		digital (PCOS)			TDC	
radiation length	1.2%		0.20%		0.29%			0.26%	

Table 3.1: The tracking chamber parameters.

3.3.2 The Particle Identification Detectors

For inclusive spin asymmetry measurements a very good positron hadron separation has to be guaranteed. To do further semi-inclusive measurements a separation of different hadrons is desirable. HERMES has four Particle Identification (PID) detectors.

The Lead Glass Calorimeter

The calorimeter like all other detectors is build in two similar halves, a top and a bottom module. One module consists of 42 $\times$ 10 lead glass blocks of 9 $\times$ 9 cm cross section and 50 cm depth, which corresponds to 18 radiation length. Each block is equipped with a photo-multiplier tube at the back plane (see figure 3.13). The nominal energy resolution for electro-magnetic showers induced by scattered positrons is energy dependent [Klei87,

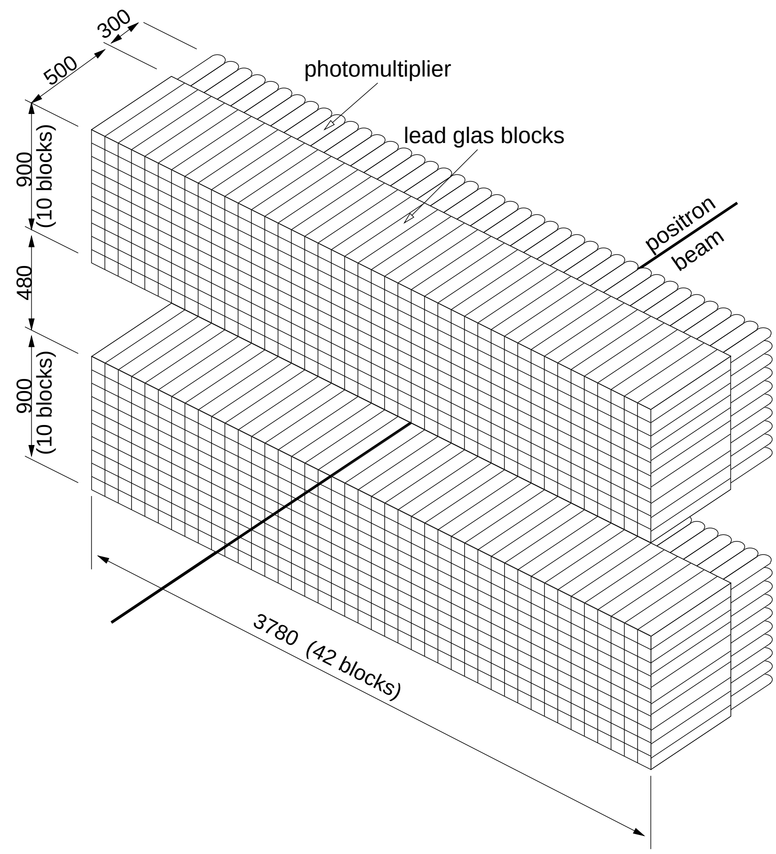

Figure 3.13: Schematical view of the two calorimeter modules (distances in mm). The two modules are mounted in a movable frame (not shown) which allows to move the modules away from the beam in vertical direction to reduce radiation damage during injection of the beams.

Dür95]:

$$\frac{\Delta E(E)}{E} = 1.47\% + \frac{5.14\%}{\sqrt{E/GeV}}. \tag{3.4}$$

Since the nuclear interaction length of lead glass is much higher than the radiation length hadrons deposit only a fraction of their energy in the calorimeter. A comparison of the momentum of a particle measured with the spectrometer with its energy deposited in the calorimeter allows a separation of hadrons and charged leptons.

The Hodoscopes

Two scintillator hodoscopes provide trigger signals (see section 3.3.3). The first (H1) is mounted in front of the TRD (see figure 3.10).

The second hodoscope called *preshower hodoscope* is mounted in front of the calorimeter and has two layers, an 11 mm thick lead sheet in front of a scintillator array. The scintillators are slabs of 90 $\times$ 9 cm covering one calorimeter block column. Positron showers originating from the lead are detected by collecting the scintillation light with photo-multipliers mounted to one end of each scintillator slab. Hadrons do not produce extensive showers in the lead and hence cause a minimum ionizing signal making a separation of positrons and hadrons possible.

The Transition Radiation Detector

The Transition Radiation Detector (TRD) is based on the principle that relativistic particles crossing a dielectric boundary cause transition radiation. The emitted photons have a typical energy of 2-15 keV for particles with $\gamma > 1000$. Positrons with energies above 3 GeV cause transition radiation ($\gamma > 5000$) whereas pions with $\gamma < 250$ do not. The TRD has six similar modules each consisting a radiator followed by an X-ray detector. The radiator is a 6.5 cm thick layer of randomly packed polypropylene fibers of 17-20 μm diameter. The transition radiation occurs at the boundary of the fibers and the surrounding gas (90%Xe, 10%CH_4). The X-rays are detected in a planar wire chamber filled with Xe gas to reach a high X-ray absorption factor (large Z). The wires are separated by 5 mm in the horizontal x-direction in between two cathode planes separated by 25 mm in the z-direction. The configuration of six consecutive modules reaches a positron-pion rejection of more than 1:100 in the HERMES energy range.

The Cerenkov Detector

Cerenkov radiation is caused by charged particles passing a medium with a velocity larger than the speed of light in this medium (c/n). Hence a separation of hadrons from positrons is possible due to their different β-factor. The HERMES Cerenkov is a threshold counter, the threshold for different particles in terms of their β is:

$$\beta_{\mathrm{thr}} = 1/n \quad \text{with dielectric constant} \quad \epsilon = n^2 \ . \tag{3.5}$$

Each detector half consists of 10 horizontally adjacent sets of two mirrors reflecting the

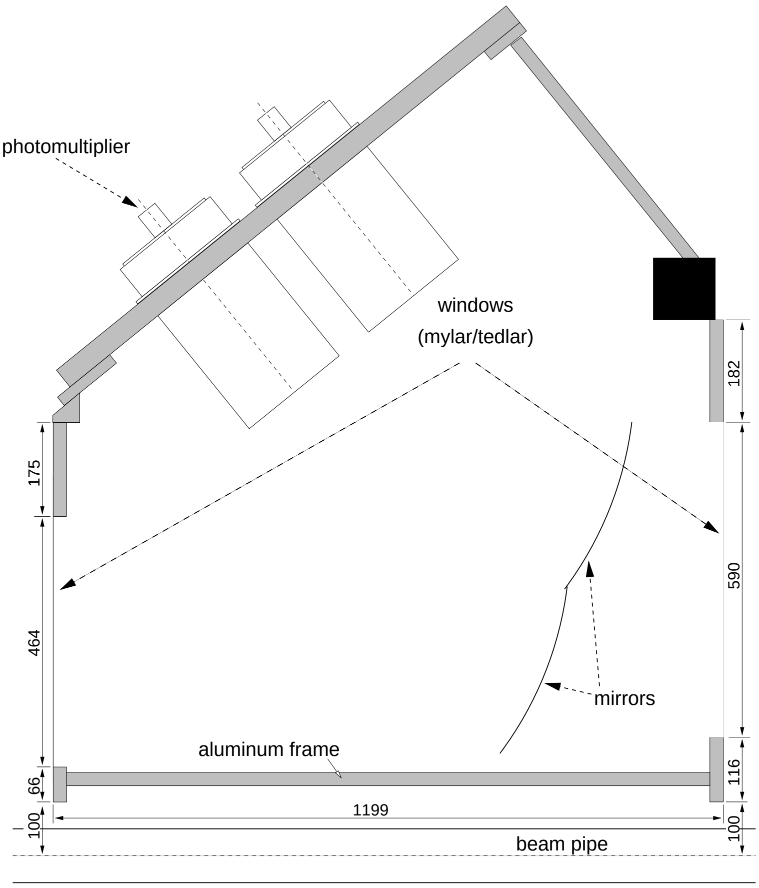

Figure 3.14: Side view of the Cerenkov detector showing one cell with two mirrors and the corresponding photo-multiplier tubes.

light into two corresponding photo-multiplier tubes (see figure 3.14). They are contained in a aluminum box with thin windows (mylar/tedlar) in the active area.

By choosing different radiator gases the momentum windows for particle identification can be adjusted. In 1995 nitrogen gas was used resulting in a pion threshold around 5.5 GeV, a kaon threshold of 19 GeV and a proton threshold of 38 GeV. Hence a clean pion sample can be identified between 5.5 and 19 GeV in the 1995 data.

3.3.3 The Trigger

To perform inclusive and semi-inclusive measurements the trigger has to select events containing the scattered positron in the detector acceptance. The expected rate of such events is, depending on the target thickness, in the order of several Hz. To achieve a maximum efficiency the major physics trigger requires four conditions [2]:

1. The signal sum of two neighboring columns of the calorimeter lead glass blocks has to be above the equivalent of a 3.5 GeV electro-magnetic shower signal.
2. The signal in the preshower detector has to be above the minimum ionizing signal.
3. A signal in the hodoscope H1 has to be present in coincidence with the above described signals.
4. All signals have to be in coincidence with a bunch crossing of a positron bunch, the HERA RF signal is used to synchronize to the bunch crossing time.

The rate of scattered hadrons in the acceptance is estimated to be roughly a factor of 400 higher than the DIS positron rate for energies around 4 GeV [HER93]. With the above described trigger setup this results in a hadron induced trigger rate which is in the order of the DIS positron triggers. The only considerable background on the trigger level which could cause problems in the Data Acquisition (DAQ), capable of recording events up to 200 Hz, comes from the proton beam. During the test-experiment in 1994 this background was studied intensively [Fie95]. As described in section 3.1 the proton background has its origin in beam rest-gas interaction upstream (in proton direction) of the HERMES experiment. These events cause hadron showers scattering into the HERMES experiment from the back side which have a high multiplicity and are time correlated to the proton bunch crossing. At the position of the calorimeter the time offset of the proton bunches with respect to the positron bunches is around 19 ns which allows a large suppression of proton background induced triggers via timing (trigger condition 4). The proton induced trigger rate is typically below 100 Hz with proton currents up to 60 mA. During the 1995 running the pure proton background related trigger rate without gas in the target was mostly below 100 Hz.

Apart from the major physics trigger described above several other triggers for calibration purposes are set up.

[2] see figure A.5 in appendix A for the electronic layout of the trigger.

3.3.4 The Luminosity Monitor

To be able to compare DIS rates and distributions with different spin configuration or target gases the luminosity for each configuration has to be known. This is achieved by monitoring a theoretically and experimentally well understood process:

Møller Scattering off the target gas electrons in case HERA runs with electrons or

Bhabha Scattering in case HERA runs with positrons (1995).

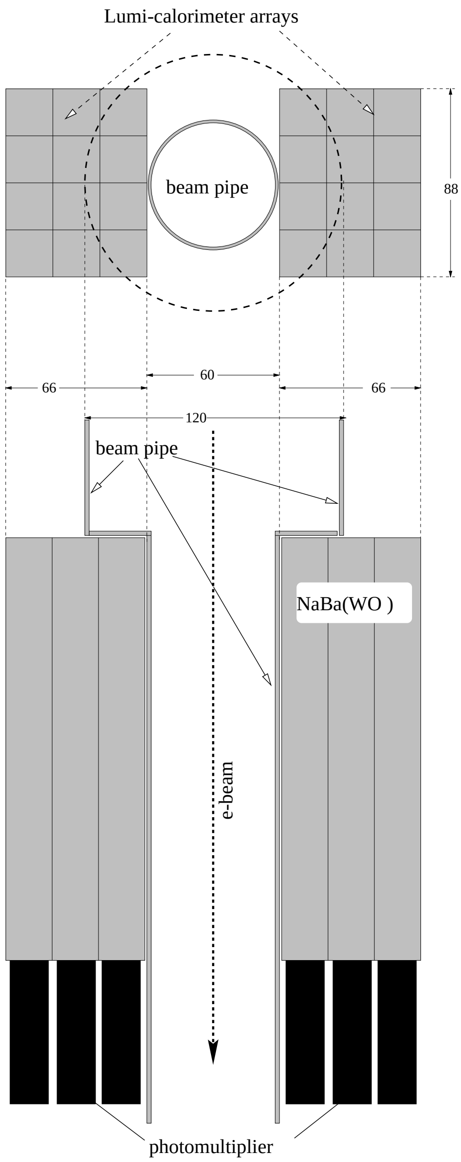

In both cases the two scattered particles are detected in coincidence in two NaBi(WO_4) arrays (see figure on the left). The two modules are located to the left and right side of the positron beam pipe 30 mm away from the nominal beam axis. The coincidence rate has practically no background and varies between 40 and 220 Hz at typical target densities of $1 \times 10^{15} \frac{\text{nucl.}}{\text{cm}^2}$ and beam currents between 10 and 35 mA. In order to measure spin asymmetries and structure function ratios only the relative luminosities of the two different target spin states or target gas types are important. Hence a precise knowledge of the absolute acceptance of the luminosity detector is not necessary. From the analysis of the 1995 data it is known that the coincidence rate is largely independent of vertical beam position and slope movements. The horizontal beam slopes and positions do affect the luminosity measurement but up to now no evidence of an effect larger than 1% has been observed. The beam position and slope normally are kept constant and if they vary it is on a time scale of hours whereas the target spin is flipped on the 10 min scale.

Chapter 4

Data Analysis

The data analysis involves the interpretation of the raw detector output in terms of physics quantities like energy or momenta. The information from the different detectors has to be transformed and calibrated using external data from the slow control system and other monitoring devices. To ensure a safe and fast analysis a common software frame for all data processing modules has been designed. All HERMES data processing software is based on the ADAMO [CER94] entity relationship model.

4.1 Software

The HERMES event builder provides the raw data in EPIO[EPIO93] format on an event by event basis. For the analysis these data are transferred into data tables organized in data-flows. Each record of a data-flow for example contains the information of one event. In addition quantities like tracks for example are related to the corresponding hits in the detectors via relationships. ADAMO ensures a safe data handling through highly organized data structures[1].

Another advantage of the system is the compatibility, it provides a common interface between the different analysis modules. Figure 4.1 shows schematically the data flow in the analysis chain. The common data exchange interface enables all programs to be used modularly:

HMC: the HERMES Monte Carlo is a GEANT based program delivering simulated detector response together with the original physics events generated by various physics generators [Dür95].

HDC: the HERMES Decoder reading raw data in EPIO format transferring them into physics quantities in ADAMO data structures while applying first level calibration

[1]for a detailed description of the software packages concerning ADAMO developed at HERMES see [CER94], [Wan95], [Ack95], [Fun95] and [Fun96]

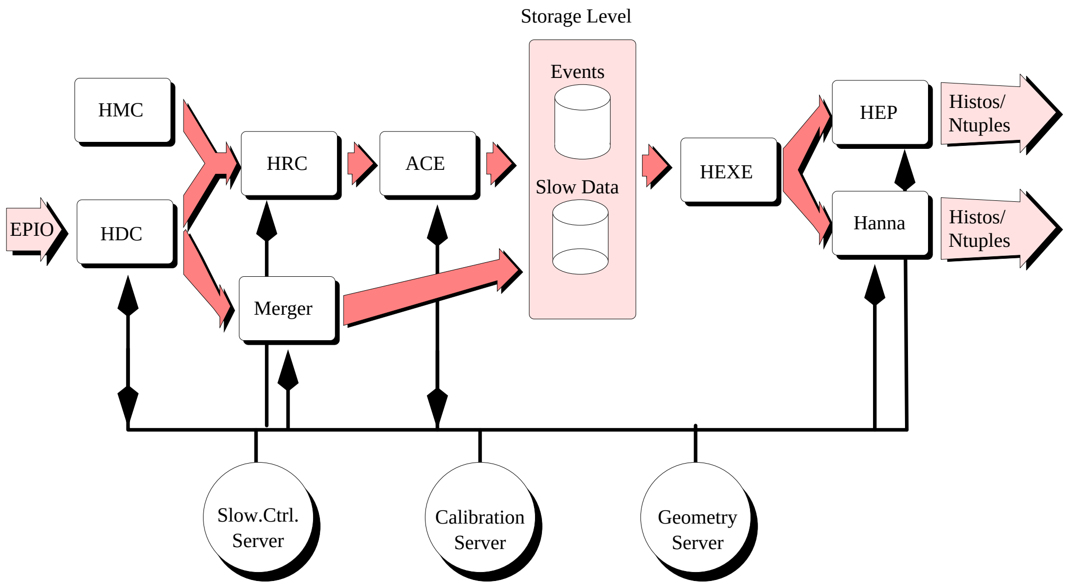

Figure 4.1: The HERMES analysis chain. The output of HDC or HMC splits into physics events and slow data being processed by different modules and stored in different files from where the data can be accessed for final analysis. The grey arrows denote the data flow in one analysis chain, whereas the black arrows denote network connections to DAD servers.

and corrections. Calibration and geometry data are retrieved in a time-dependent manner for each single event via the appropriate DAD servers.

HRC: the HERMES Reconstruction program reads events in ADAMO data structures either from HDC or HRC . Using a tree search algorithm [Wan96] it reconstructs tracks and provides particle identification using the PID-detectors for each track. The program also provides further calibration procedures.

ACE: the Alignment, Calibration and Efficiency program calculates calibration constants and efficiencies in various ways. It can connect to DAD servers to retrieve and store alignment and calibration data.

HEXE: the HERMES Event Mixer is a data filter capable of filtering multiple ADAMO or DAD input data-flows into one or several output data-flows. It is used to select special events for example.

HEP: the HERMES Event Processor incorporates all ADAMO features together with PAW . It merges slow control data like the luminosity with each single reconstructed event and increments histograms and ntuples. The final physics analysis can be done using this package.

HANNA: is an event driven analysis frame providing a library of user callable functions to access slow control and calibration data. Using the library the analysis has synchronized access to the entire slow control data necessary for the final physics analysis [Fun96].

DAD SERVERS: are part of the Distributed ADAMO Database package[Wan95] and provide an intelligent access to the HERMES database across different platforms. The DAD client server concept is also used for online monitoring and is the basis of the HERMES slow control system.

The entire HERMES data are visualized and manipulated using graphical user interfaces. A special package has been developed to create online and off-line data handling tools called PINK [Ack95] (see appendix C).

4.2 Analysis Chain

The data for analysis can be divided into three different types:

Physics Events, are the triggered events containing the entire detector output for each event along with some statistical information like event number, run number, time etc.,

Slow Data contain information on everything which is monitored on a longer time scale than the triggered events, this includes information monitored by the slow control system online as well as information generated during off-line analysis of these data.

Reconstruction Input which is all information needed to reconstruct an event, e.g. drift velocities for each drift chamber cell, pedestals etc.

The slow control information is retrieved from the hardware online and fed into online DAD servers providing access to multiple users across the network for online monitoring. The data kept in the servers is regularly written to a file based database by a taping client. Some of the slow control information is also written into the online event stream as a so called *user event* which can be decoded during analysis (using HDC, see above). The synchronization of all three data types during analysis is done via time stamps. Each event and each entry in the slow control database contains a time stamp in seconds, faster synchronization is provided for certain data within the online event stream on a $10\,\mu\mathrm{sec}$ level. This is valid for the scaler events for example which contain trigger counts and Bhabha event counts from the luminosity monitor. The scalers are read out and reset every ten seconds, these intervals are called *bursts*. In addition to the time synchronization, the physics events are also tagged with the burst number they belong to.

4.3 Reconstruction

The reconstruction of decoded events (HDC output) is done by HRC [Wan96]. The program uses a *tree search algorithm* to find tracks from hits in the tracking chambers, these are then related to the information of the PID detectors.

4.3.1 Tracking

As described in section 3.3.1 the tracking chambers provide position information in u, v and x direction. For each direction hits belonging to one track are found using a lookup table. The lookup table contains all independent patterns and sub-patterns which belong to a possible physics track in the detectors. The finite resolution and possible miscalibrations are taken into account by choosing a road width in which hits are searched for. The recursive binary tree search algorithm finds the appropriate pattern called tree line for each direction and calculates from u and v direction track parameters in the x direction which are then compared with all tree lines in x direction. The algorithm takes into account the resolution and efficiency for each single plane. As input parameters HRC gets the maximum number of missing hits allowed per tree line and track. The optimal set of reconstruction parameters has been retrieved from Monte Carlo simulations and studies of real data. The tracks found in the region in front of and behind the magnet are then combined to full tracks. A momentum lookup table generated with precision measurements of the magnetic field inside the spectrometer magnet is used to assign each track its momentum [Wan96].

4.3.2 Resolution

The tracking chambers have a finite resolution which depends on the individual chamber, calibration and alignment constants. Provided the alignment and all calibration constants are well known a Monte Carlo analysis yields an overall angle and energy resolution, however the Monte Carlo simulation uses the same magnetic field map which is based on measurements and which is known to be exact within . On the other hand the resolution can be estimated using known physics processes. To be independent of the PID the reconstructed K_s^0-mass is chosen to determine the angular and energy resolution. The K_s^0 decays into two oppositely charged pions with a probability of 69%, a mass of $m_K = (497.672 \pm 0.031)$ MeV and a lifetime of $\tau = (0.8926 \pm 0.0012) \times 10^{-10}$ s [PDG94]. The $\mathrm{K_s^0}$-mass m_K is given as:

$$m_K^2 = 2m_\pi^2 + 2\sqrt{m_{\pi^+}^2 + p_{\pi^+}^2}2\sqrt{m_{\pi^-}^2 + p_{\pi^-}^2} - 2p_{\vec{\pi}^+} \cdot p_{\vec{\pi}^-} \ . \tag{4.1}$$

For the analysis the two pionic tracks have to have a common vertex which is at least 40 cm behind the primary vertex which is defined by the reconstructed scattered positron. This condition suppresses the combinatorial background since pions not originating from K_s^0-decays mostly come from the initial scattering process and have a common vertex with the scattered positron. The reconstructed direction of the kaon momentum has to point to the primary vertex which again suppresses the background. Figure 4.2 shows the reconstructed $\mathrm{K_s^0}$-mass peak. The deviation from the literature value is 0.08%. The width is a measure of the angular and energy resolution, a comparison with a Monte Carlo, where the resolution is a variable parameter yields an energy resolution of better than 1% and an angular resolution of 1 mrad for 4 GeV pions.

4.3.3 Particle Identification

After a track is found the corresponding hits in the PID detectors are related to it. From the response of the preshower, TRD and calorimeter together with the momentum of a track a PID likelihood is calculated taking the expected flux of positrons and hadrons and their expected detector response into account. The PID likelihoods for a single detector is:

$$\mathcal{L}_{det}^e = \frac{\mathcal{P}_{det}^e}{\mathcal{P}_{det}^e + \mathcal{P}_{det}^h} \ , \tag{4.2}$$

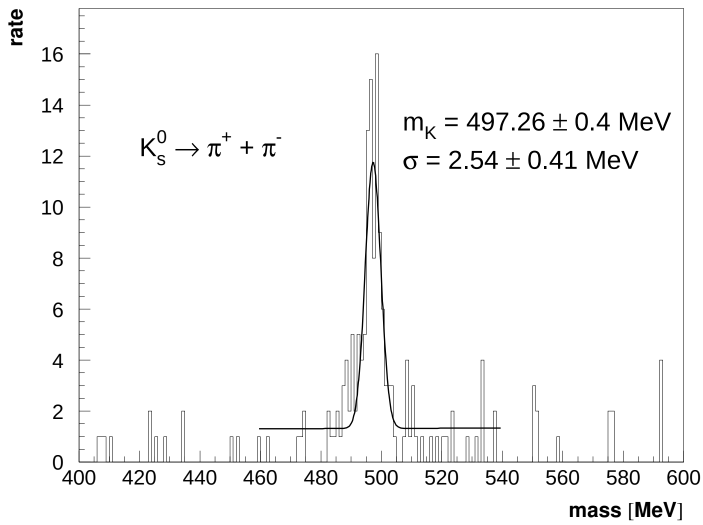

Figure 4.2: Reconstructed $\mathrm{K_s^0}$-mass from the $\mathrm{H_2/D_2}$ data used for this analysis. A cut on the distance between DIS vertex and $\mathrm{K_s^0}$ decay vertex has been applied to reduce the combinatorial background.

where $\mathcal{P}_{det}^{e/h}$ are the probabilities for pion/hadrons. The combined likelihood for the three PID detectors is given by:

$$\mathcal{L}^{e/h} = \frac{\mathcal{P}_{Pre}^{e/h} \quad \mathcal{P}_{TRD}^{e/h} \quad \mathcal{P}_{Calo}^{e/h}}{\mathcal{P}_{Pre}^{e}\mathcal{P}_{TRD}^{e}\mathcal{P}_{Calo}^{e} + \mathcal{P}_{Pre}^{h}\mathcal{P}_{TRD}^{h}\mathcal{P}_{Calo}^{h}} \,. \tag{4.3}$$

Figure 4.3 shows the preshower pulse, the ratio of calorimeter energy over the momentum determined with the spectrometer and the TRD pulse for all tracks (upper plots) and compares it with the PID-likelihood (lower plots). The vertical lines correspond to electron hadron separating cuts on each PID signal separately, the horizontal line corresponds to the PID-likelihood cut used for this analysis yielding a much higher efficiency and lower contaminations. For separating the pions from other hadrons the Cerenkov detector is used. As stated in the previous chapter the threshold for pions to generate Cerenkov light was 5.5 GeV in 1995. Figure 4.4 compares the PID-likelihood versus the number of photoelectrons detected in the Cerenkov for particles with a momentum lower (left) and higher (right) 5.5 GeV. For a clean pion identification a signal corresponding 0.25 photoelectrons is required for the hadrons above threshold. Using this pion PID 12% of all hadrons can be identified as pions. In 1996 a different Cerenkov gas will lower the threshold to 3.5 GeV so that more than 40% of the hadrons can be identified as pions. The TRD can not be used consistently for all periods of the unpolarized data, however

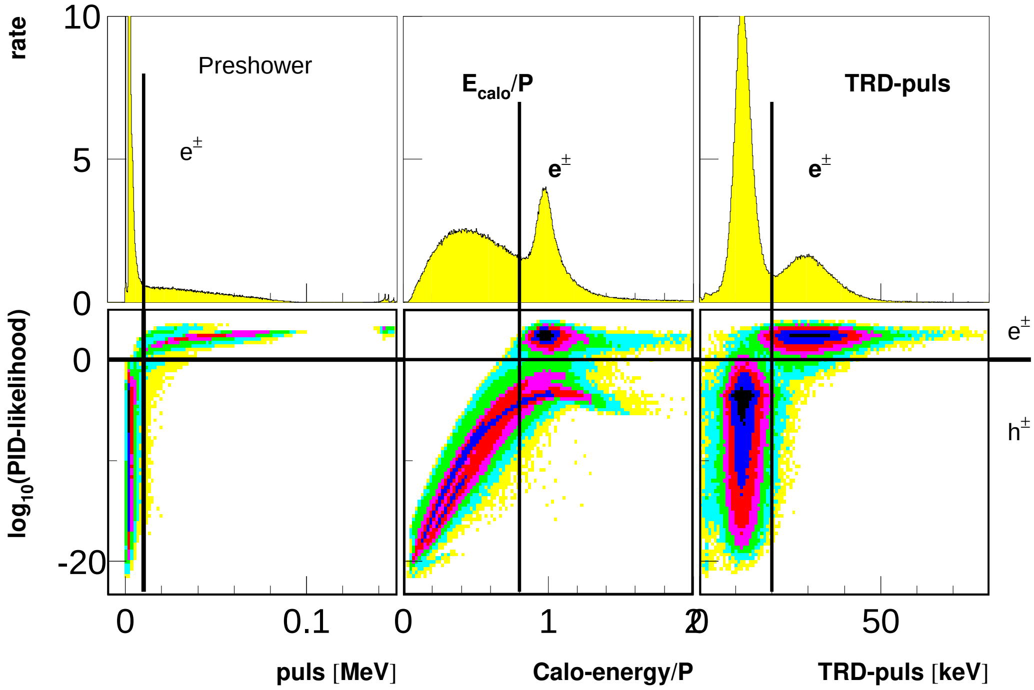

Figure 4.3: The detector responses of the three PID detectors preshower, calorimeter and Cerenkov compared with the PID-likelihood. The upper row shows the detector response for the preshower, the ratio of the energy measured by the calorimeter over the reconstructed momentum and the TRD response. The vertical line corresponds to cut separating electrons from hadrons for each single detector. The lower row shows the logarithm of the PID-likelihood for electrons versus the above plotted values for each detector. The electron hadron separation is indicated by the horizontal line in the lower plots.

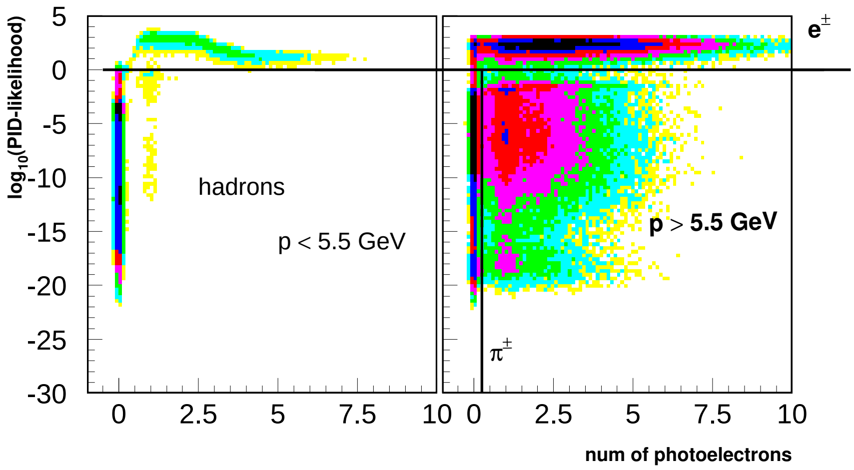

Figure 4.4: Cerenkov pulse versus PID likelihood ratio. The left plot contains all tracks with a momentum below the pion threshold of the Cerenkov of 5.5 GeV, the right plot contains all tracks above threshold. The vertical line denotes the additional cut applied to identify a track as a pion.

with a cut only on the PID likelihood without TRD a positron efficiency of at least 95% with a hadron contamination of below 3% is obtained.

4.4 The 1995 data

The major physics goal for HERMES in the 1995 data taking period was the extraction of the spin structure function g_1^n using a polarized $^3\mathrm{He}$ target. Unpolarized data were taken in order to measure the structure function ratio $F_2^{\mathrm{n}}/F_2^{\mathrm{p}}$ and compare it to previous measurements. From July to November three periods of data taking with unpolarized $\mathrm{H_2}/\mathrm{D_2}$ targets took place. The analysis described here is based mainly on these three periods. To compare data from hydrogen and deuterium targets the gas type has been changed frequently to keep systematic errors small. During a typical HERA positron fill which lasts about 6-10 h the target has been changed up to 15 times. The three unpolarized data taking periods have been analyzed separately, in the following they are referred to as period I-III (see table 4.1) From 56 h of data taking 43 h have been selected for the final analysis. As mentioned in section 3.1.2 the target density for unpolarized targets is only limited by the HERA positron beam lifetime. Since the lifetime depends solely on the electron density of the target a constant lifetime reduction for $\mathrm{H_2}$ and $\mathrm{D_2}$ is maintained by keeping the molecular flow into the storage cell constant. The maximum target thickness tolerable for running in parallel with the other HERA experiments is $1 \times 10^{15} \frac{\mathrm{nucl.}}{\mathrm{cm}^2}$ for $\mathrm{H_2}$

period	$H_2 \to D_2$	$\int_t H_2$	$\int_t D_2$	% of H_2	% of D_2	% of total	# e^+	# h
I	$\approx$ 50 min	6.3 h	4.9 h	26.4	25.5	26.0	265K	120K
II	$\approx$ 40 min	11.1 h	11.0 h	46.4	57.3	51.3	429K	207K
III	$\approx$ 130 min	6.5 h	3.2 h	27.2	16.7	22.7	285K	132K

Table 4.1: Statistics accumulated during three periods of unpolarized data taking, note that the last column represents only the hadrons where a positron was found in the event defining the kinematics

and twice as much for D_2. This results in twice as much statistics for the D_2 target at a constant target change interval. This results in comparable statistics on the neutron inside the deuteron which is important to keep the statistical errors comparable when extracting neutron data from deuterium and hydrogen targets.

In order to extract unpolarized structure function ratios for $F_2^{^3\mathrm{He}}/F_2^{\mathrm{D}}$ the data taken with the polarized $^3\mathrm{He}$ target are used. The data are spin averaged by selecting the same relative luminosity for both spin states weighted with the mean target polarization.

4.5 Data Selection

All data taken with H_2 and D_2 target are reconstructed and the appropriate slow control data are merged and synchronized with the physics events like described in section 4.2. There are different levels of data quality checks, some run periods are rejected because of known problems with the target or spectrometer, other criteria can be applied in the 10 sec burst level.

4.5.1 Normalized Yields

The information on the target gas for each burst is taken from two independent sources, the bottle valve status bit of the gas feed system which indicates which gas bottle was open at a time and the target gas change bit which is flipped whenever the target gas is changed. These data are compared to the normalized yields defined as:

$$Y_n \equiv \left[\frac{N^{e^+} T_{gen}/T_{acc}}{L_c}\right]_{\text{(per burst)}} , \tag{4.4}$$

where T_{gen}/T_{acc} is the ratio of generated over accepted triggers per burst and N^{e^+} is the number of reconstructed positrons per burst. Figure 4.5 compares the information of the bottle valve status and the normalized positron yield. Since the yield is normalized with the Bhabha coincidence rate and the molecular target gas flow is kept constant (see section 4.4) one expects roughly a factor of two in the yield between H_2 and D_2 targets because

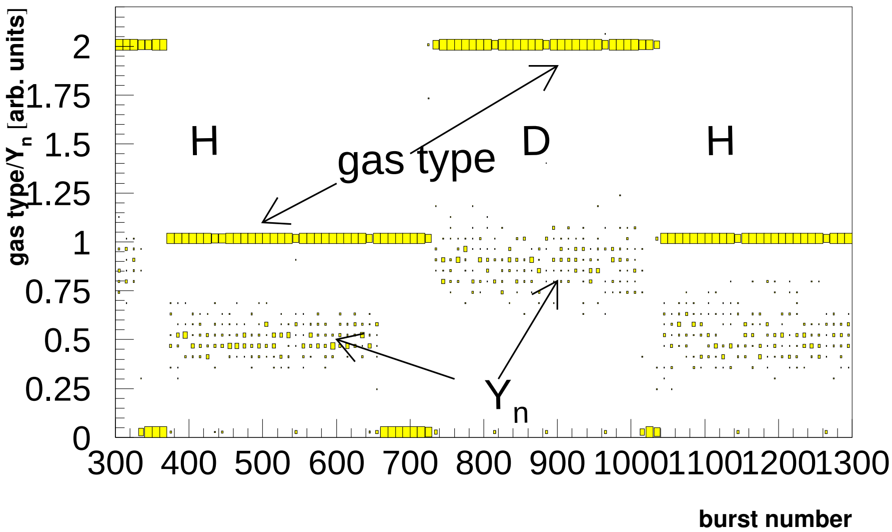

Figure 4.5: The normalized positron yield and the status information on the gas type (arbitrary units).

the DIS positron rate depends on the parton and hence the nucleon density of the target. The graph shows this factor of two; additionally there are empty bursts at the start of a run when several detector equipments are initialized which causes a high dead-time of the DAQ-system.

The yield Y_n is calculated separately for positrons and hadrons in the upper and lower detector half. A sample of runs is checked for detector trips, target gas type, and stability of all detector signals and used to calculate the mean values for the normalized yields. Provided the spectrometer including the luminosity monitor is stable the normalized yield is target density independent and fluctuations should be statistical. This is confirmed by fitting the yields with a Gaussian which for good runs results in a χ^2 per degree of freedom around 1. Figure 4.6 shows the normalized positron yield for the upper detector for a sample of deuterium runs with a Gaussian fit. The shaded histogram represents bursts which are rejected by requiring the yield of the burst to lie in a two sigma range around the mean for the upper and lower detector separately. Applying such a cut for each target rejects empty bursts as well as bursts where detectors tripped or the overall efficiency including the trigger efficiency dropped.

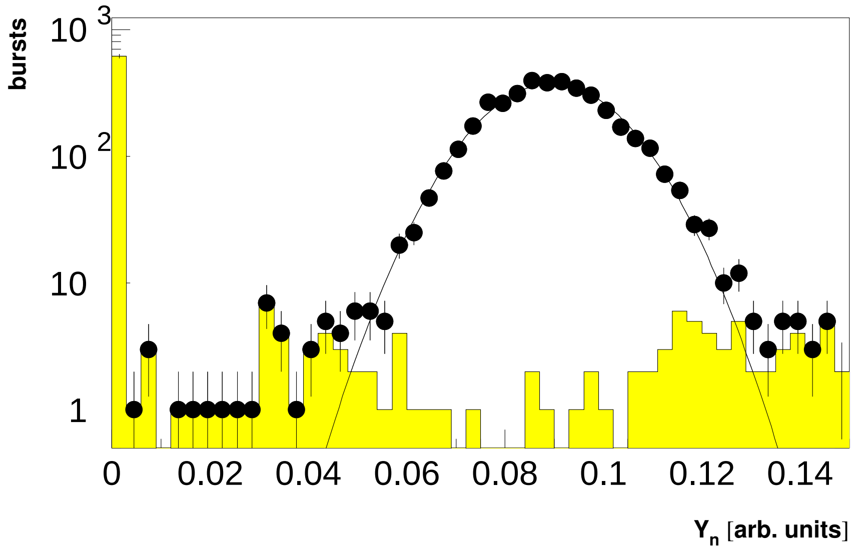

Figure 4.6: The normalized positron yield in the entire detector fitted with a Gaussian (data points). The shaded histogram shows bursts which are rejected by applying two sigma cuts on the yield in the upper/lower detector separately (log. scale, arbitrary units).

4.5.2 Luminosity and Normalization

The stability of the luminosity monitor is a prerequisite for the above described quality check, hence it has to be checked independently. This is done using the information on the target density from the target gas feed system which is the gas flow rate into the storage cell and its temperature (see section 3.2). The target density multiplied with the beam current which is measured by integrating the current for each single positron bunch (data provided by HERA) is proportional to the luminosity. This value $L_{\mathrm{T}} = n_{\mathrm{target}} I_{\mathrm{beam}}$ can be used to check the luminosity monitor. Figure 4.7 shows the ratio of the relative

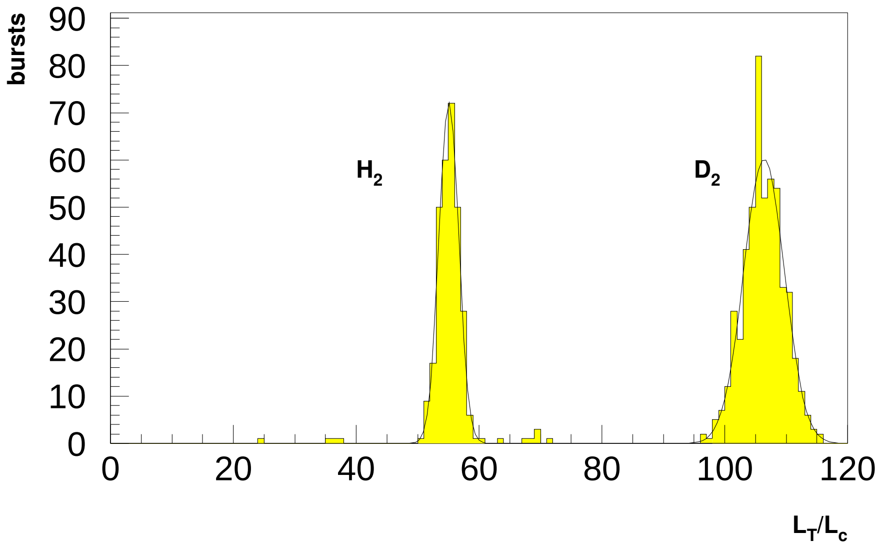

Figure 4.7: Luminosity determined with target density and beam current divided by luminosity taken from the luminosity monitor (arbitrary units).

luminosities determined with target density and beam current over luminosity obtained by measuring the Bhabha coincidence rate with the luminosity monitor. For both targets a Gaussian fit yields a σ of 3%. The ratio is calculated for every burst, although the target density information can only be retrieved on a 30-60 sec update interval which is the reason for the width of the distributions. The mean value for the H_2 target is expected to be exactly half as high as the mean for the D_2 target. The fit indicates a 3.5% deviation which is due to an approximation made in the target density calculation assuming the ratio of molecular to viscose flow to be independent of the gas type and pressure. This ratio is needed to calculate the gas flow using a known conductance and a pressure difference.

The Luminosity monitor is stable over several days. Over longer time scales the measured Bhabha coincidence rate has to be corrected for gain drops in the two calorimeters and other effects which lead to uncertainties in comparing data from different time periods (see section 5.2).

4.5.3 PID Detector Checks

As an independent check on the PID detectors their mean response for hadrons and positrons versus time is checked. This is done using three of the four PID detectors (see section 4.3.3) to identify a track as a positron or hadron and plotting the corresponding PID signal of the fourth detector versus time or run number. As figure 4.8 shows the PID

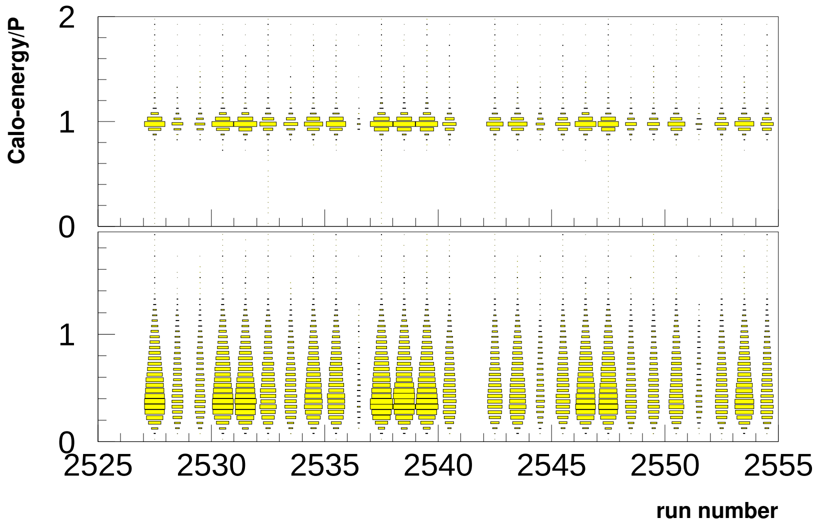

Figure 4.8: PID stability versus run number, the upper plot shows the ratio E_{calo}/P for tracks identified as electrons/positrons by the other PID detectors. The lower plot shows the same for hadrons.

detector response is very stable versus time for the selected runs. Runs where the mean PID detector response fluctuates are taken out of the analysis and are analyzed separately. Most of this data can be recovered by re-calibration.

4.5.4 Efficiencies

As a cross check for the yield analysis the efficiencies of the tracking chambers are calculated and mean efficiencies per burst and run determined. The ACE program therefore analyzes the front and back region separately. For each track and chamber plane the hits in the corresponding plane are compared with the track impact point. The tracking parameters are taken into account in this procedure. Separately for the front and back region a maximum number of missing chamber hits per tree line and track is specified as input to the reconstruction program (see section 4.3.1). The efficiency for a plane is only calculated if the hits in this plane were not necessary to reconstruct the track, this ensures that there is no bias in the efficiency calculation. In a region around the track impact point which is defined by the wire spacing hits are counted and the number of hits per track is a measure for the efficiency of the particular plane. Figure 4.9 shows the mean

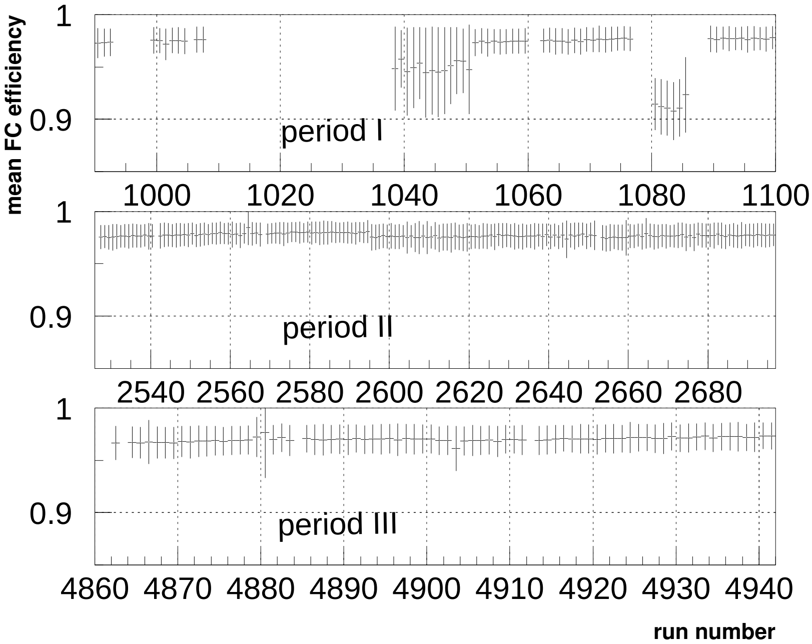

Figure 4.9: The mean front chamber efficiency versus run number for the three periods of unpolarized H_2 /D_2 data taking. The vertical bar indicates the error on the mean. The efficiency is stable above 95% except for period I where it drops slightly for two run samples (1038-1050 and 1080-1086).

chamber efficiency for the front chambers for all unpolarized runs used for this analysis. The efficiency is stable at 98% except for two periods where it drops down to 94% and 90% respectively. Figure 4.10 shows the same efficiency for the back chambers, which is very stable around 95.5% for period I and II with a slight drop at the end of period I, in period III an increase to 97.5% has been achieved by optimizing the high voltage of the chambers.

Since the VC's can not be used for this analysis due to hardware and software problems, the redundancy in the front region is lower with 4 planes for each wire direction compared to 8 planes in the back region. Therefore the effect of decreasing chamber efficiency on the overall reconstruction efficiency is larger in the front region as can be seen

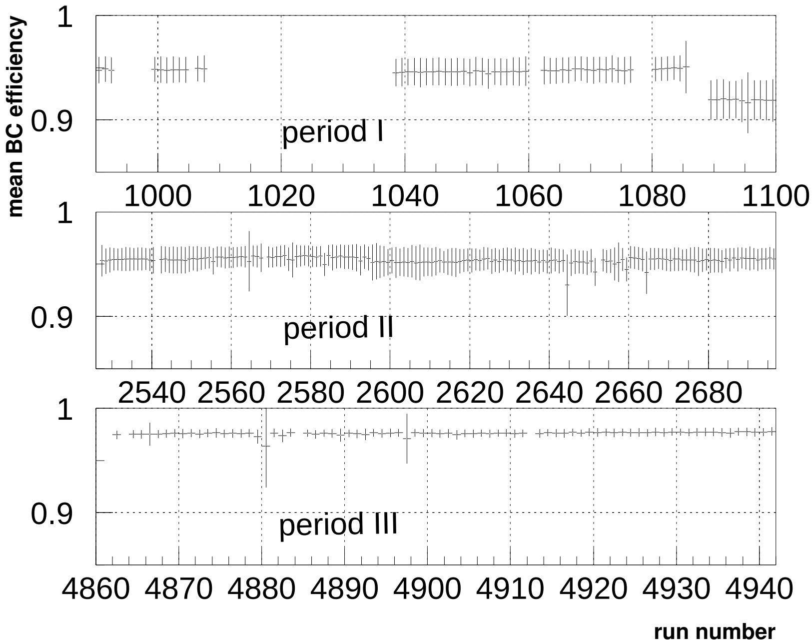

Figure 4.10: The mean back chamber efficiency versus run number for the three periods of unpolarized H_2 /D_2 data taking. The vertical bar indicates the error on the mean. The efficiency in period I is 95% and drops to 92% for the last runs. In period II it is stable at 95%, an increase to 97% achieved by optimization of the HV settings is seen for period III.

in figure 4.11[2]. From the efficiencies for each plane an overall reconstruction efficiency

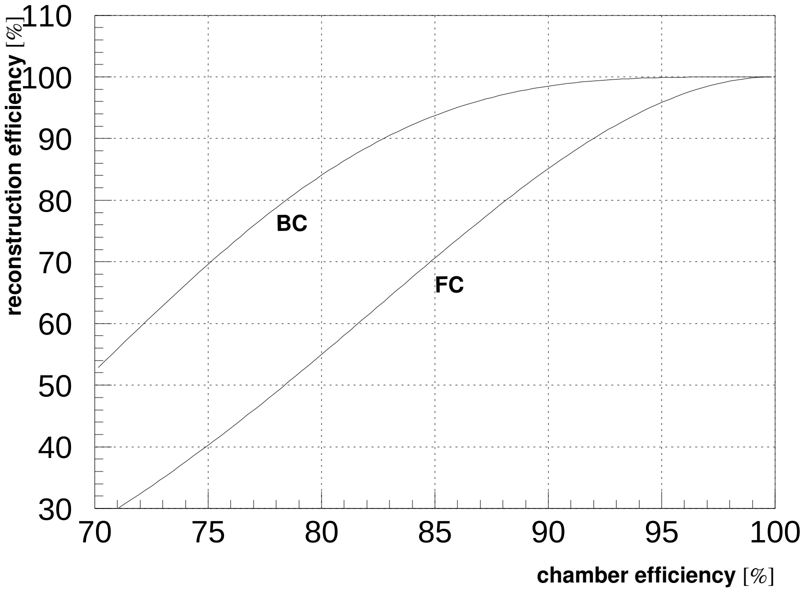

Figure 4.11: Calculated reconstruction efficiency versus mean chamber efficiency for the selected reconstruction parameters, 1/3 missing hits per tree-line/track allowed in the FC's, 3/9 for the BC's.

is calculated for the upper and lower detector separately. The measured rates are then corrected for efficiency fluctuations.

It should be pointed out here that the exact absolute value of the efficiencies is not important for the analysis of structure function ratios.

[2]for a detailed discussion the reader is referred to [Wan96]

Chapter 5

Structure Function Ratios

This chapter describes the analysis and results from inclusive measurements with unpolarized H_2 , D_2 and spin averaged $^3\mathrm{He}$ data taken 1995. The structure function ratio $F_2^{\mathrm{n}}/F_2^{\mathrm{p}}$ is extracted using data from the three unpolarized $\mathrm{H}_2/\mathrm{D}_2$ periods. The ratio $F_2^{^3\mathrm{He}}/F_2^{\mathrm{D}}$ is extracted using the $\mathrm{H}_2/\mathrm{D}_2$ and spin averaged $^3\mathrm{He}$ data samples. The advantage of measuring ratios of structure functions instead of extracting the absolute structure functions is that only the relative luminosity and acceptance for two different targets have to be known. Since the targets are changed frequently this reduces the systematic error significantly.

5.1 $\mathrm{F}_2^{\mathrm{n}}/\mathrm{F}_2^{\mathrm{p}}$

Using data from both the H_2 and D_2 target taken by HERMES in 1995 the ratio $F_2^{\mathrm{n}}/F_2^{\mathrm{p}}$ can be deduced under certain assumptions. In section 2.2 (equation 2.22) the unpolarized one photon exchange cross section is expressed in terms of the structure function $F_2(Q^2, x)$ and the ratio of the longitudinal and transverse cross section $R(Q^2, x)$. Hence in the one photon exchange case the ratio of cross sections σ for deuterium and proton at any fixed x and Q^2 is:

$$\frac{\sigma^d}{\sigma^p} = \frac{F_2^d}{F_2^p}\frac{1+R^p}{1+R^d}\frac{1+\xi R^d}{1+\xi R^p} \ , \tag{5.1}$$

with:

$$\xi = \left(1 + \frac{y^2 + Q^2/E^2}{2(1-y-Q^2/4E^2)}\right)^{-1} \ . \tag{5.2}$$

As stated before $R(Q^2, x)$ is small and the difference in $R(Q^2, x)$ for deuterium and hydrogen has been determined experimentally ([Bal95, Whi90]) to be negligibly small. The deviation from the mean $R(Q^2, x)$ is well below 3%, the effect on $F_2^{\mathrm{n}}/F_2^{\mathrm{p}}$ was determined to be below 0.5% for $x > 0.01$ by the NMC [Bal95]. This means that the structure function ratio is proportional to the cross section ratio.

Since the energies in DIS are much higher than the binding energy of deuterium the structure function of deuterium should be equivalent to the sum of the neutron and proton structure function: $F_2^d = \frac{1}{2}(F_2^n + F_2^p)$ and the ratio $F_2^{\mathrm{n}}/F_2^{\mathrm{p}}$ is then:

$$\frac{F_2^{\mathrm{n}}}{F_2^{\mathrm{p}}} = \frac{2F_2^{\mathrm{d}}}{F_2^{\mathrm{p}}} - 1 \ . \tag{5.3}$$

In the HERMES experiment the number of scattered positrons in x- and Q^2-bins is counted along with the relative luminosity measured with the luminosity detector for both targets. The number of coincidence events $L_c^{\Delta t}$ (see section 3.3.4) in a certain time interval Δt is proportional to the positron flux ϕ and the target charge density n_Z:

$$L_c^{\Delta t} \sim \int_{\Delta t} \phi n_Z dt \ , \tag{5.4}$$

hence the cross section is proportional to the number of scattered positrons $N^{\Delta t}$ during a time interval Δt divided by the number of luminosity coincidence events during that time:

$$\sigma \sim \frac{N^{\Delta t}}{L_c^{\Delta t}} \ . \tag{5.5}$$

Finally the ratio $F_2^{\mathrm{n}}/F_2^{\mathrm{p}}$ in terms of directly measured quantities becomes:

$$\frac{F_2^{\mathrm{n}}}{F_2^{\mathrm{p}}} = \frac{2N^{\mathrm{d}}}{N^{\mathrm{p}}\frac{2L_c^{\mathrm{d}}}{L_c^{\mathrm{p}}}} - 1, \tag{5.6}$$

where $N^{\mathrm{d/p}}$ is the number of detected scattered positrons and $L_c^{\mathrm{d/p}}$ is the integrated luminosity coincidence rate for the D_2 , H_2 target respectively. The factor 2 in front of the luminosity counts for deuterium reflects the correction $\mathrm{A/Z}$ to get the nucleon density from the density of the electrons of the target gas atoms. A number of corrections have to be applied to these raw counts.

5.1.1 Corrections

There are two major corrections which have to be applied to the measured structure function ratio, radiative corrections and corrections to the measured kinematic variables due to the finite detector resolution, Bremsstrahlung losses and multiple scattering in detector materials.

Radiative Corrections

The structure function F_2 is proportional to the one photon exchange cross section $\sigma_{1\gamma}$, the measured cross section σ_{all} contains all processes contributing to lepton nucleon scattering. The higher order processes have to be subtracted from the measured cross section in order to determine F_2. The radiative corrections either change the kinematics of the events or change the cross section. This is customarily taken into account by multiplying the measured cross section with the inverse of the radiative correction factor η which depends on the kinematics:

$$\eta(x,y) = \frac{d^2\sigma_{all}}{d^2\sigma_{1\gamma}} \,, \tag{5.7}$$

The corrections are calculated with the program TERAD [Brü93] which makes use of the Ahkundov, Bardin and Shumeiko model [Akh86]. The electro-magnetic processes are calculated to the order α^4, the electro-weak γZ interference to the order $\alpha \mathrm{G_F}$ plus higher order electro-weak corrections[1]. The most important processes are indicated in figure 5.1.

The radiative corrections can be divided into several major classes of corrections:

leptonic current correction which consists of Bremsstrahlung radiated by the incoming or outgoing lepton, changing the kinematics and cross section of the event,

lepton vertex correction due to a photon exchanged between the incoming and outgoing lepton,

hadronic current correction which is similar to the leptonic one in the sense that the quarks are considered free charged particles which can radiate Bremsstrahlung photons,

hadronic vertex correction similar to the leptonic,

vacuum polarization where the virtual photon fluctuates into a lepton anti-lepton or quark anti-quark pair resulting in a change of the cross section,

electro weak correction which consists of the exchange of a virtual Z_0-boson. This process can be treated as a small correction at $Q^2 \ll M_{Z_0}$.

Radiative tails describe the contribution of elastic scattering where similar to the lepton current corrections real photons radiated by the incoming or outgoing lepton change the kinematics and cross section.

In order to calculate these different processes the structure functions and nuclear form factors have to be known over the entire kinematic range contributing to the measured range. Since the determination of exactly this structure functions is the goal of the correction, an iterative process is used. The structure functions of the proton and deuterium have been measured in previous experiments so that they can be used as input for this analysis, the iteration only involves tuning the structure function to the HERMES kinematical range.

[1] for a detailed description and comparison with other radiative correction programs see [Brü93]

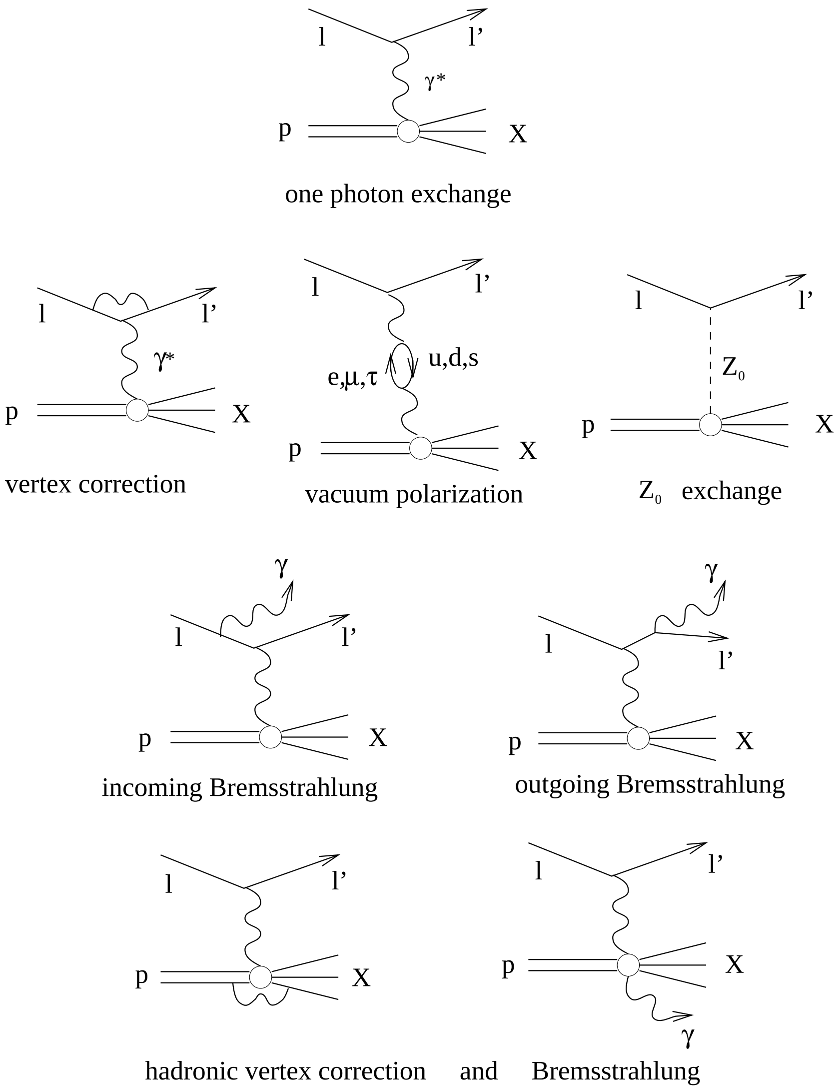

Figure 5.1: The most important processes contributing to the lepton nucleon cross section. The upper diagram corresponds to the one-photon exchange cross section, the lower ones denote the radiative processes.

For a scattered positron with a measured relative energy transfer y an integration over all kinematically allowed processes yields the radiative correction factor. This means that for large values of y the integration region and hence the magnitude of the correction and the uncertainties rise. Figure 5.2 shows the radiative correction factor versus $log(x)$ and y,

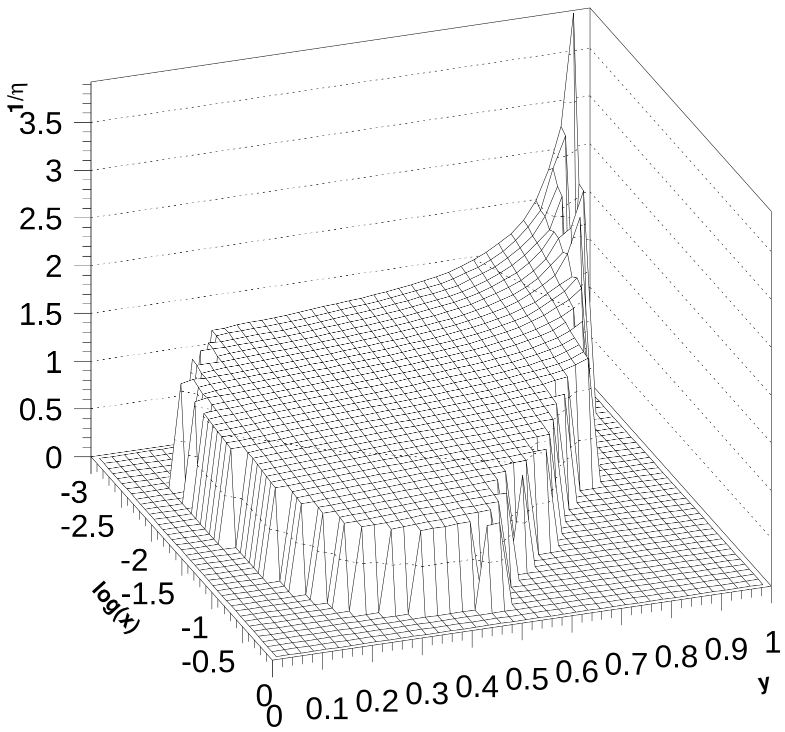

Figure 5.2: The radiative correction factor $1/\eta(x, y)$ for the HERMES kinematical range, a cut on $y < 0.85$ avoids applying large corrections with large uncertainties.

for small x and large y the integration region is very large resulting in a large correction. For this analysis only events with $y < 0.85$ are considered to keep the systematic error small.

Unfolding

The measured kinematic variables are smeared due to the finite detector resolution, Bremsstrahlung and multiple scattering (see section 4.3.2) the measured distributions therefore have to be corrected. In principle if the detector resolution would be constant over the entire kinematic range and the events would be distributed uniformly this smearing would cancel. As soon as a distribution differs from uniformity smearing of the kinematic variables causes a distortion of the measured compared to the original distribution.

If the smearing is not uniform itself, but has preferred directions and magnitudes in the kinematic plane even a uniform original distribution will be deformed which is the case for measuring x and Q^2 for example. In the simplest case the smearing depends only on the smearing in the two independent kinematic variables Q^2 and x. To unfold distributions in the Q^2-x plane it is segmented into bins b_{ij} which are selected in a way that the bins are populated as even as possible. Smearing is now a discrete process, it causes events originating from bin b_{ij} to be actually measured in another bin $b_{i'j'}$ which is mostly but not necessarily a neighboring bin dependent on the choice of the binning.

In principle the exact knowledge of the migration matrix $M_{iji'j'}$ could be used to unfold the measured distributions. The migration of original bin contents into the measured bins can only be determined using a Monte Carlo simulation. Therefore the detector response as well as interaction of the scattered particles with material for each detector have to be put into the Monte Carlo as realistic as possible. The Monte Carlo result on the migration matrix will be uncertain to a certain extend due to the imperfect detector implementation and limited statistics so that the matrix can not be inverted or suffers from large uncertainties. For this analysis the distributions have been unfolded in the Q^2-x plane using an algorithm based on Bayes' Theorem [Ago94][2]. The program uses reconstructed Monte Carlo events as input from which the migration matrix is calculated in a variable binning, then an iterative procedure unfolds the original distribution from the measured one and calculates statistical and systematical uncertainties for each bin.

DAQ-dead-time Correction

The DAQ dead-time is defined as the number of physics events written to tape $\mathrm{T_{acc}}$ divided by the number of physics triggers generated $\mathrm{T_{gen}}$, $\mathrm{D_{DAQ}} = \mathrm{T_{acc}}/\mathrm{T_{gen}}$. Alternatively one defines the DAQ correction factor $\mathrm{C_{DAQ}} = 1/\mathrm{D_{DAQ}}$. The DAQ system is capable of taking data up to 200 events per second, however depending on the proton background conditions and beam current the trigger rates either exceeds this or the statistical distribution of events leads to dead-time. In addition initialization procedures running at the beginning of each run cause a rise of the dead-time during the first 1-4 bursts of a run. In order to take this into account, the DAQ correction factor is calculated for each burst so that each event can be weighted with it. This ensures that the comparison of distributions and rates are independent of the DAQ system.

[2] implemented by M. Ferstl [Fer96]

5.1.2 Kinematical Cuts

variable	minimum	maximum
Q^2	0.1 GeV^2	-
W^2	6.0 GeV^2	-
y	0.0	0.85
θ_y	0.04 rad	-
Z_{vertex}	-20 cm	20 cm
DAQ-lifetime	30%	100%

Certain kinematic cuts have to be applied to the data in order to avoid regions where corrections get too large (see previous section). Most important for the low x region is the y cut. A cut on W^2 removes particles from the resonance region which especially at large x will dilute the measurement of the nucleon structure with resonances.

A Q^2 cut has to be applied for the semi-inclusive measurements to ensure that assumptions about the fragmentation process are valid (see section 6).

5.1.3 Extraction Procedure

The extraction of the structure function ratio involves two main steps of analysis:

- binning of the identified positrons in bins of Q^2 and x within the kinematic cuts described in section 5.1.2 without corrections in order to unfold the raw distributions and

- binning of DAQ-dead-time and radiative corrected data into x bins and calculating $F_2^{\rm n}/F_2^{\rm p}$.

The unfolding of distributions has to be done on the raw count rates per bin. This is done for the $\mathrm{H_2}$ and $\mathrm{D_2}$ data of each data taking period separately. $F_2^{\rm n}/F_2^{\rm p}$ is then determined via equation 5.6 for each x-bin integrated over Q^2 for both the unfolded and raw distributions yielding $[\mathrm{F_2^n/F_2^p}]_{\mathrm{unf}}(\mathrm{x})$ and $[\mathrm{F_2^n/F_2^p}]_{\mathrm{raw}}(\mathrm{x})$. The unfolding correction $\mathrm{C_{unf}}$ for each x-bin x_i is then:

$$C_{\mathrm{unf}}(x_i) = \frac{[F_2^n/F_2^p]_{\mathrm{unf}}(x_i)}{[F_2^n/F_2^p]_{\mathrm{raw}}(x_i)}. \tag{5.8}$$

It is a multiplicative correction. The bin centers x_{c^i}, $Q^2_{c^i}$ are determined by calculating the mean x, Q^2 for each x- and Q^2-bin. Figure 5.4 (lower plot) shows the unfolding correction to $F_2^{\rm n}/F_2^{\rm p}$. The error bars are still dominated by the Monte Carlo statistics. In addition the Monte Carlo generators for HMC are limited in the kinematical range. The lowest Q^2 accessible is 0.5 GeV^2 which leads to an error in the unfolding procedure since there are not all bins populated with MC events which potentially can contribute to smearing into and out of the lowest x-bins. The unfolding correction is below 3%.

As a cross check an alternative smearing correction is obtained by generating Monte Carlo events for both targets where the NMC parameterization for $F_2^{\rm n}/F_2^{\rm p}$ is used. The detector resolution is simulated as realistic as possible (only average chamber efficiencies and resolutions are used, no single plane or wire resolutions). The same extraction

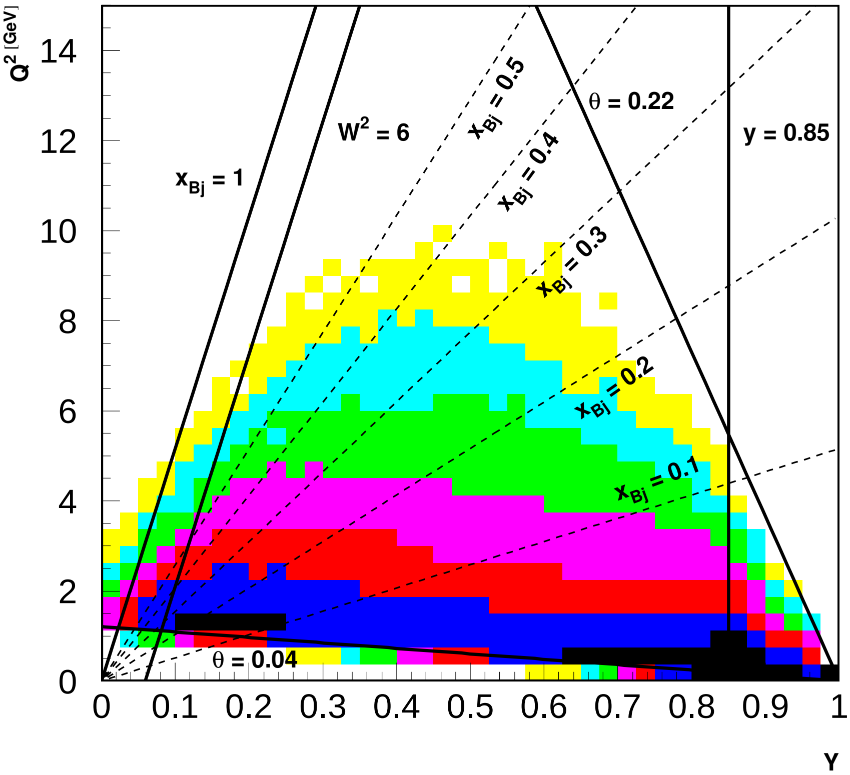

Figure 5.3: Kinematic cuts in the Q^2-y plane. The acceptance of the HERMES spectrometer is indicated by the lines labeled with the minimum/maximum scattering angle acceptance, $\theta = 0.04/0.22$. The kinematic cuts in W and y are shown as solid lines. The diagonal dashed lines labeled with $x = 0.1 - 1.0$ indicate the variation in x. The shaded area shows the distribution of reconstructed events in the Q^2-y plane. The Q^2-cut at $Q^2 = 0.1$ is not shown.

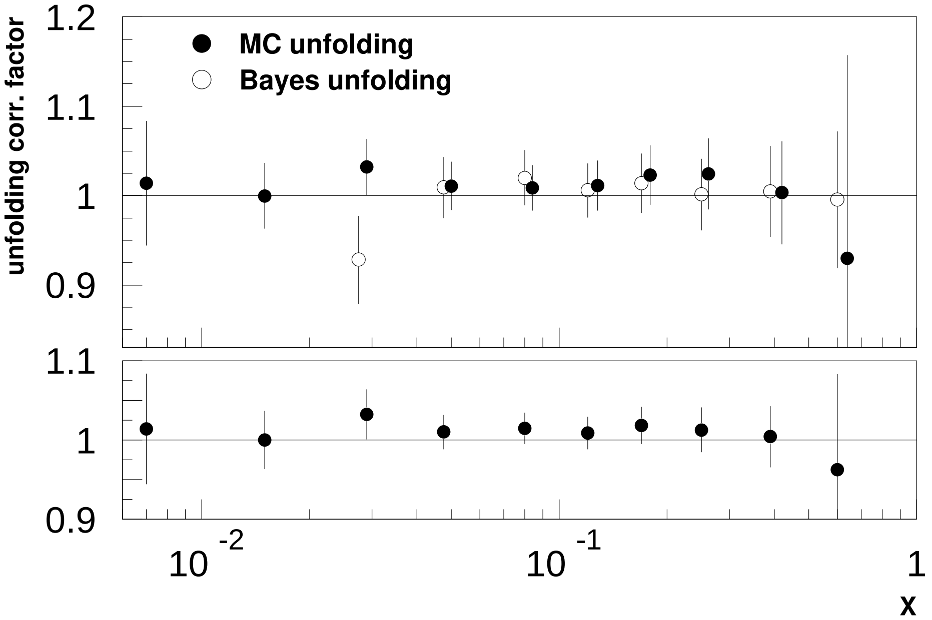

Figure 5.4: Unfolding correction for the ratio $F_2^{\rm n}/F_2^{\rm p}$ versus x. The two methods described in the text are shown, the direct Monte Carlo method points have been shifted to the right for better visibility. The lower plot shows the weighted mean of the two correction factors. The lowest x point of the Bayes method (open circle) has a large systematic error and is not considered in the calculation of the weighted mean of the two methods.

procedure as used for the real data is used to extract $F_2^{\mathrm{n}}/F_2^{\mathrm{p}}$, both for the generated and reconstructed Monte Carlo distributions. Dividing the two sets of $F_2^{\mathrm{n}}/F_2^{\mathrm{p}}$ yields a smearing correction factor for $F_2^{\mathrm{n}}/F_2^{\mathrm{p}}$ for each bin.

The two methods agree well within their errors, the unfolding method using Bayes' algorithm can not compute a correction for the lowest x-bins because of low statistics. The simple Monte Carlo method gets a correction factor for these low bins, but the error is quite large and it has to be stressed that the structure functions which are used to simulate the distributions are not well known for such low Q^2 values ($\ll 1$). The unfolding correction applied to the data is the weighted mean of the two methods (see figure 5.4, lower plot) since the Monte Carlo sample is different for both methods. The lowest point of the Bayes' correction is not taken into account because of the above described uncertainty.

Additionally the positrons are binned into x-bins (the same binning as in the unfolding distributions) applying the DAQ dead-time correction and radiative correction for each event. The bin content $S(x_i)$ for the x-bin x_i is given by:

$$\begin{aligned} S_{\mathrm{H/D}}(x_i) &= \sum_{\mathrm{H/D}} e^{+}(x, Q^2, ..., t) C_{\mathrm{rad}}(x, y) C_{\mathrm{DAQ}}(t) \\ & \quad \text{with } (\mathrm{x}, \mathrm{Q}^2, ..., \mathrm{t}) \text{ inside bin and cuts! .} \end{aligned} \tag{5.9}$$

The index H/D refers to the different targets, the sum is over all events from one target in a data taking period which fulfill the cuts on kinematic variables and the data selection criteria described in section 4.5. Finally the unfolding correction factor is applied to the corrected ratio:

$$[F_2^n/F_2^p]_{\mathrm{final}} = [F_2^n/F_2^p]_{\mathrm{corr}}(x_{c^i}) C_{\mathrm{unf}}(x_{c^i}) \; . \tag{5.10}$$

This procedure is possible since all corrections applied are multiplicative.

The same procedure as described above is applied to the electron events in the data sample. The electrons detected can only originate from pair production and misidentified negative hadrons, all other processes like J/ψ-decay are negligible. Since pair production is symmetric with respect to the charge, subtracting the electron bin contents from the positron bin contents is an appropriate correction for pair production positrons in the scattered positron sample. The production of hadrons is not charge symmetric (see section 6) but subtracting the misidentified fraction from the positron sample is a first order correction for misidentified positive hadrons in the positron sample. The difference of negative and positive hadrons enters only as a second order effect into a small correction. In figure 5.5 the relative electron rate for both targets is plotted versus x, the rate at low x is below 8%, at high x the rate is negligible. The correction to $F_2^{\mathrm{n}}/F_2^{\mathrm{p}}$ is well below 1% for the used bins.

The ratio $F_2^{\mathrm{n}}/F_2^{\mathrm{p}}$ is determined for the three unpolarized $\mathrm{H_2/D_2}$ periods separately, figure 5.6 shows the result separately.

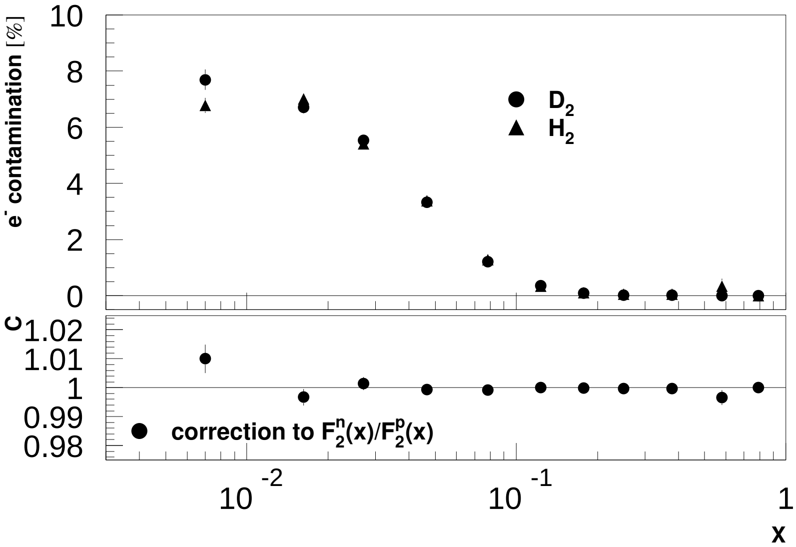

Figure 5.5: The electron contamination in the data sample for $\mathrm{H_2}$ and $\mathrm{D_2}$. The lowest and highest x-bin is not used for extraction of $F_2^{\mathrm{n}}/F_2^{\mathrm{p}}$ because of low statistics and high systematic errors. The lower plot shows the correction factor to $F_2^{\mathrm{n}}/F_2^{\mathrm{p}}$.

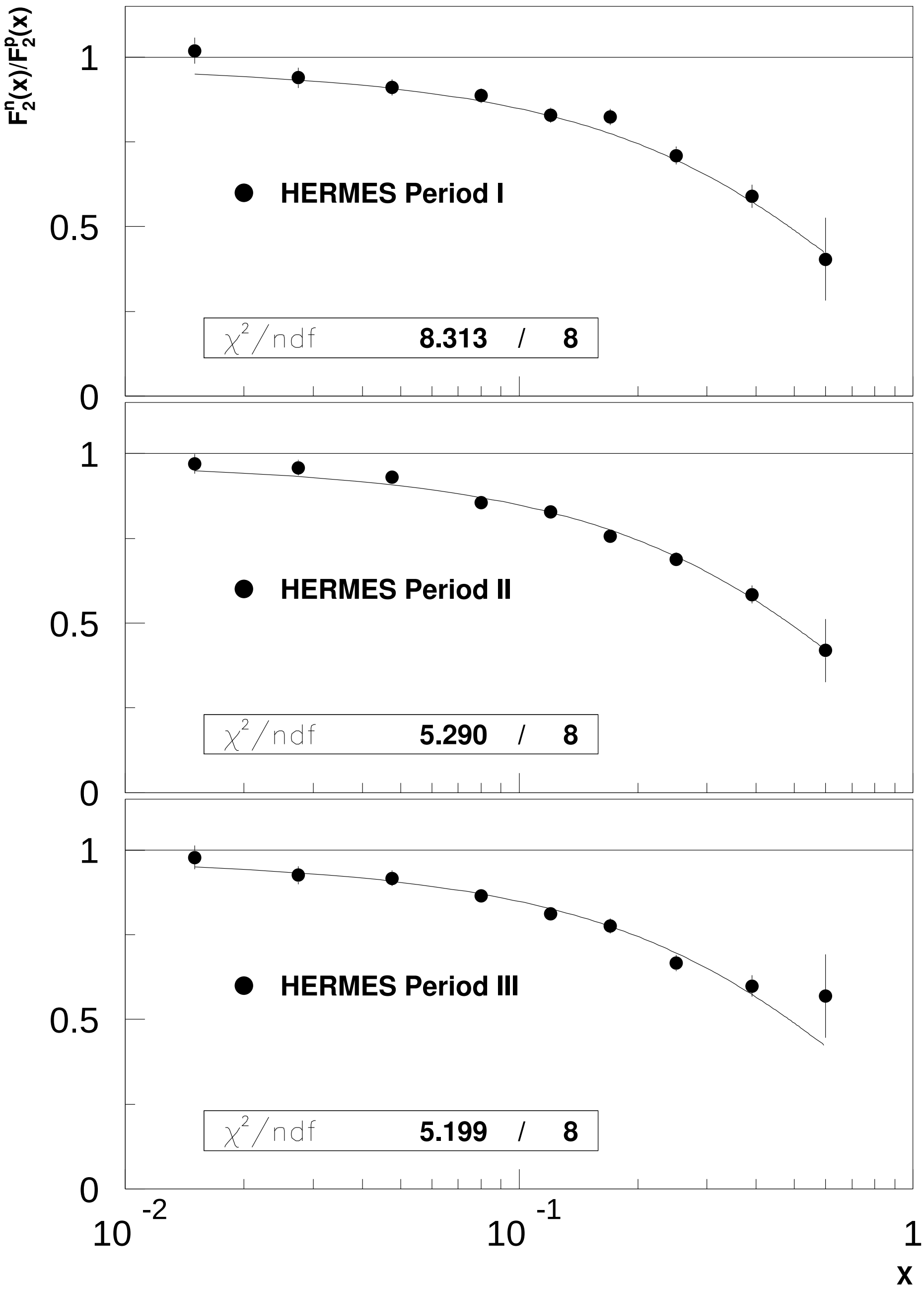

Figure 5.6: The ratio $F_2^{\mathrm{n}}/F_2^{\mathrm{p}}$ versus x from the three data taking periods described in section 4.4 compared with a fit to the NMC data, the χ^2 represents the deviation from the NMC fit. The HERMES data are unfolded and radiative corrections have been applied. Only statistical errors are shown.

a_1	0.67225
a_2	1.6254
a_3	-0.15436
a_4	0.048301
a_5	0.41979
a_6	0.047331
a_7	-0.17816

The HERMES data are plotted together with a fit to the NMC data, the χ^2 indicates a good agreement with the NMC fit for all three periods independently (see figure 5.6). The fit function yielding the fit parameters for the NMC data listed in the table on the left is [Brü96]:

$$f_{\mathrm{n/p}}(x) = a_1(1-x)^{a_2} + a_3 x^{a_4} + a_5 + a_6 z + a_7 z^2$$
$$\text{with } z = \frac{1}{2}\ln(1+e^{(2-1000x)}). \tag{5.11}$$

Finally the data on $F_2^{\mathrm{n}}/F_2^{\mathrm{p}}$ for the three periods are added according to their statistical weight and compared to the NMC and SLAC [Whi92] data in figure 5.7.

5.1.4 Q^2 Dependence

In the QPM the structure functions are predicted to scale. Only higher order QCD processes can lead to a violation of scaling. A similar Q^2-dependence for the proton and neutron with only small deviations due to the different quark composition is expected. Therefore the Q^2 dependence of the structure function ratio should scale and can be used to confirm the predictions. The NMC measured the Q^2 dependence of $F_2^{\mathrm{n}}/F_2^{\mathrm{p}}$ over a wide kinematic range. The NMC experiment (see [Brü93, Kab95]) not only measured at higher energies and hence higher Q^2 but they also could vary the beam energy and cover a broader range. HERMES can not determine a Q^2 dependence due the relatively small range in Q^2 (see figure 5.3, page 66), however the comparison with high precision data using a different experimental method confirms both measurements.

The extraction of the Q^2 dependence is similar to the above described extraction of $F_2^{\mathrm{n}}/F_2^{\mathrm{p}}$. The same binning and correction procedure is applied. After calculation of the weighted bin centers in Q^2 and x, $F_2^{\mathrm{n}}/F_2^{\mathrm{p}}$ is calculated for each bin. Figure 5.8 shows the binning and the raw population (left plot) of the bins, the right plot shows the bin centers after cuts are applied. To compare the results with NMC data the values of $F_2^{\mathrm{n}}/F_2^{\mathrm{p}}$ have to be shifted to the appropriate x-values at which the NMC data are available. This is done using the NMC parameterization $f_{\mathrm{n/p}}(x)$ of the measured $F_2^{\mathrm{n}}/F_2^{\mathrm{p}}$. The x-bin centers of the data are shifted to the desired x value using the measured value $F_2^{\mathrm{n}}(x_m)/F_2^{\mathrm{p}}(x_m)$ at the bin center x_m and the first derivative $f'_{\mathrm{n/p}}(x_m)$ to extrapolate to the desired x-value $x_d = x_m + \Delta x$:

$$\frac{F_2^n(x_d,Q^2)}{F_2^p(x_d,Q^2)} = \frac{F_2^n(x_m,Q^2)}{F_2^p(x_m,Q^2)} + \Delta x f'_{\mathrm{n/p}}(x_m) \tag{5.12}$$

Figure 5.9 shows the results on the Q^2-dependence of $F_2^{\mathrm{n}}/F_2^{\mathrm{p}}$ for the HERMES data compared with the NMC measurements. Within the error bars the HERMES data agree with the NMC data in most of the x-bins. As stated before, the kinematic range of HERMES is

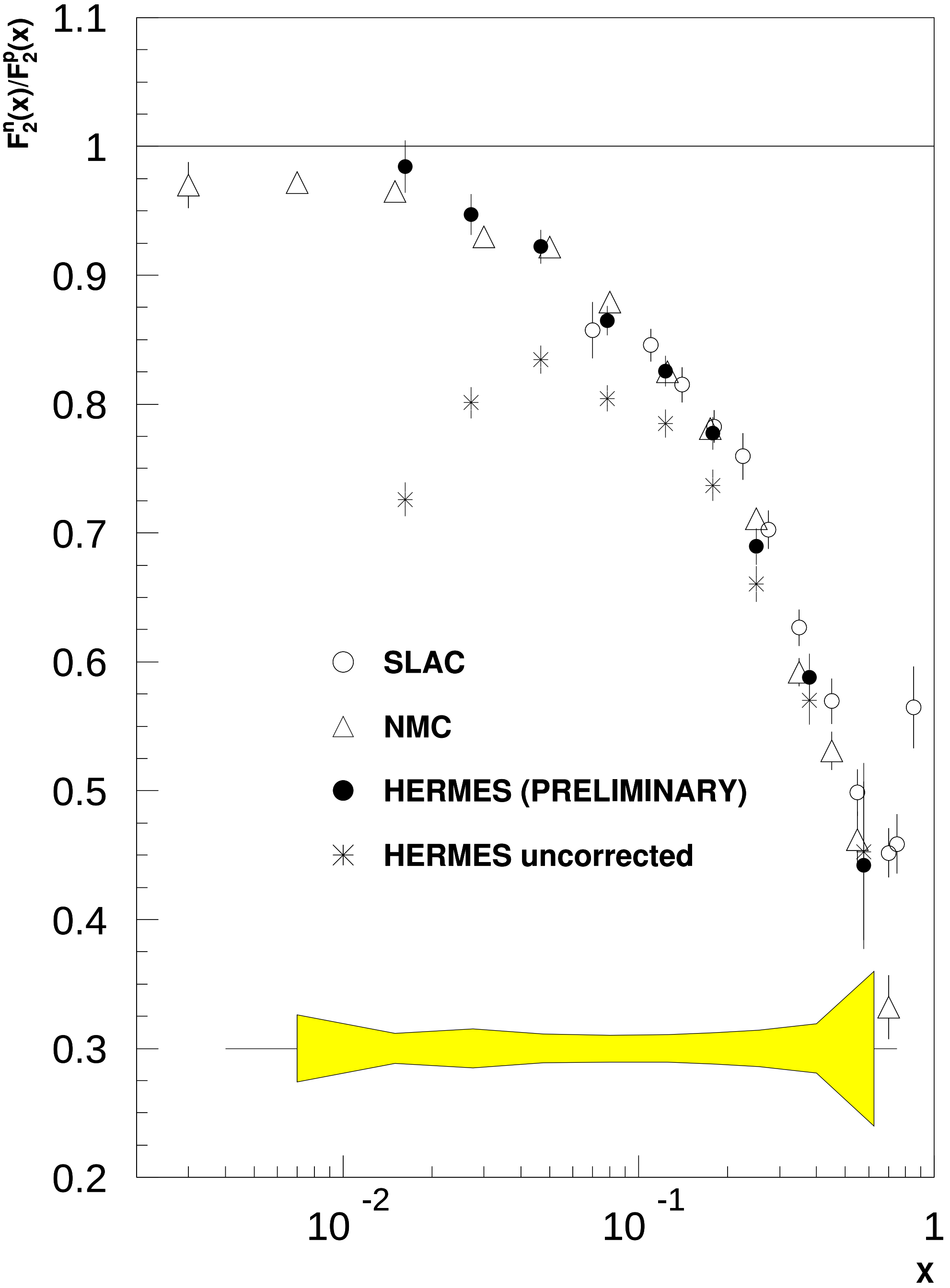

Figure 5.7: The ratio F_2^n/F_2^p versus x from this analysis compared with previous measurements at CERN and SLAC . The fully corrected data are shown as solid dots, for comparison the uncorrected data are shown as stars. The grey area gives an upper bound of the systematic uncertainties.

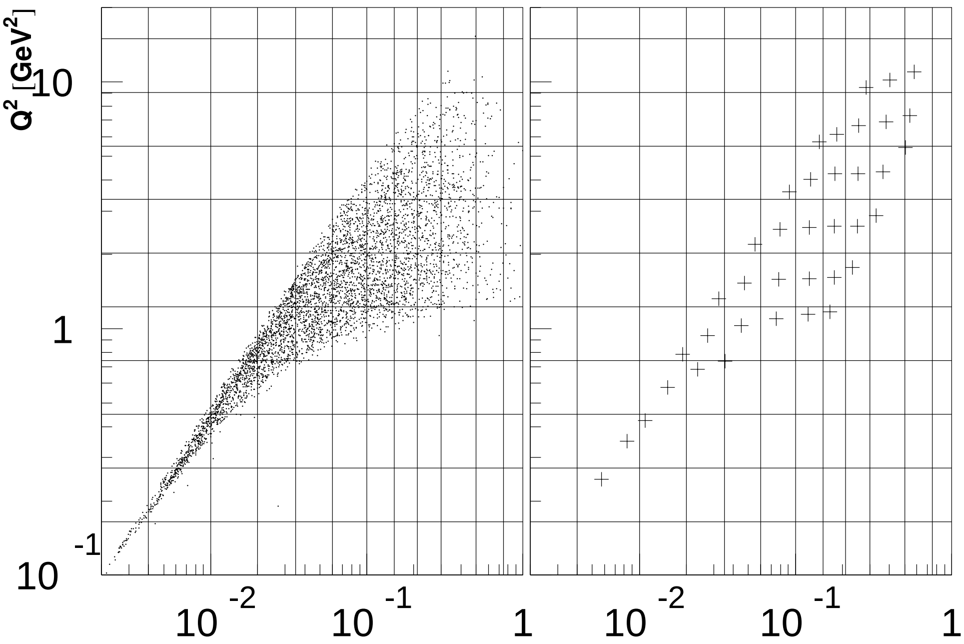

Figure 5.8: The binning in Q^2 vs x (log scale), and the distribution of 5000 events without kinematical cuts (left plot). The right plot shows the weighted bin centers for each bin after applying cuts on the entire data sample.

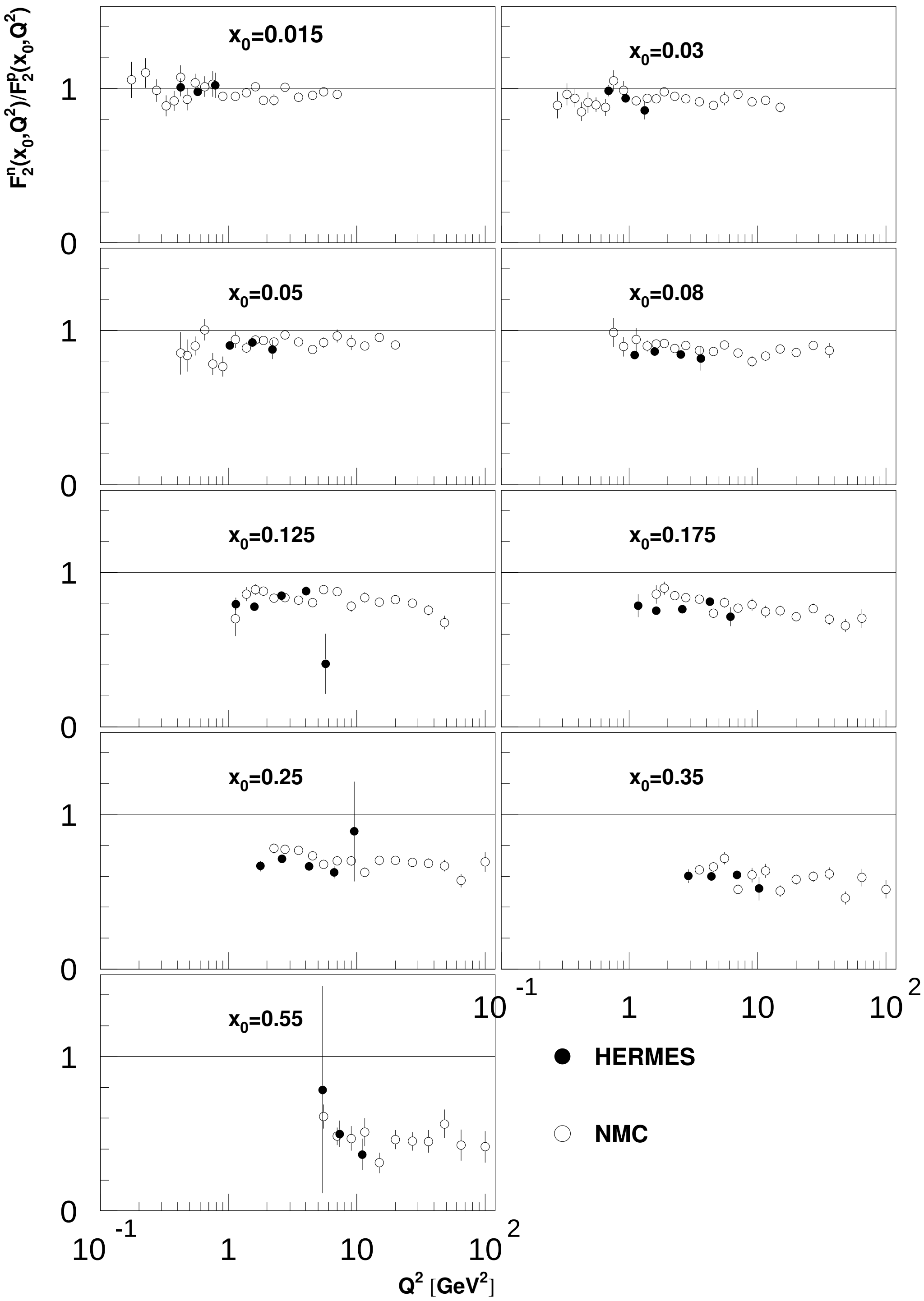

Figure 5.9: Q^2 dependence of F_2^n/F_2^p in different x-bins. For the HERMES data only statistical errors are shown.

limited, within this range no Q^2-dependence of $F_2^{\mathrm{n}}/F_2^{\mathrm{p}}$ is observed taking the statistical error bars into account. However no disagreement with the Q^2-dependence observed in the NMC data can be seen.

5.1.5 Systematic Errors

The first step in checking $F_2^{\mathrm{n}}/F_2^{\mathrm{p}}$ for systematic effects is the check of variations taking subsamples of the data to extract $F_2^{\mathrm{n}}/F_2^{\mathrm{p}}$. This has been done not only for the three independent data taking periods, but also for each HERA fill and random samples within each period. Within the resulting statistical error no variation has been observed.

Error in Radiative Corrections

The radiative correction program needs several input parameters (see section 5.1.1). For the ratio $F_2^{\mathrm{n}}/F_2^{\mathrm{p}}$ only the difference of the radiative corrections between the H_2 and D_2 targets is important and the most important input parameters are the structure functions itself as well as nuclear form factors. Since the structure functions and form factors have been measured no iterative procedure is necessary. The agreement of the structure function ratio $F_2^{\mathrm{n}}/F_2^{\mathrm{p}}$ with previous measurements by the NMC indicates that taking their parameterization of the absolute structure functions is the best input. Nevertheless varying the input parameters and comparing the resulting correction $\eta(x, y)$ yields an upper limit for the uncertainties on the radiative corrections. Figure 5.10 shows the absolute uncertainty versus x.

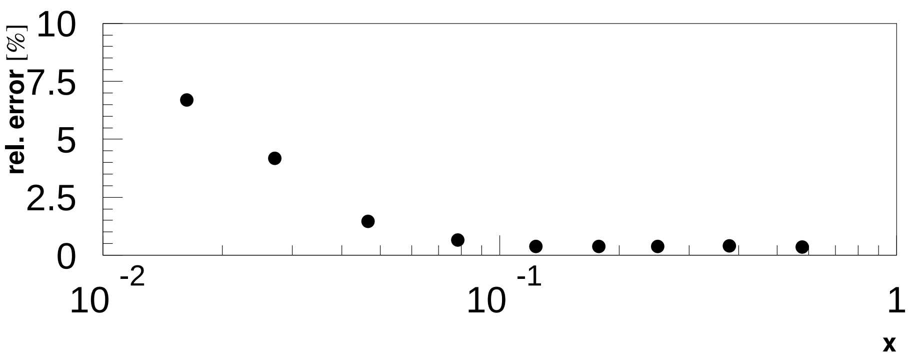

Figure 5.10: The upper limit for the uncertainty in the radiative corrections versus x.

Normalization

As equation 5.6 shows only the relative normalization between data taken with hydrogen and deuterium targets has to be known to extract $F_2^{\mathrm{n}}/F_2^{\mathrm{p}}$. On the other hand the relative normalization goes into $F_2^{\mathrm{n}}/F_2^{\mathrm{p}}$ directly and will influence the result linearly. The most severe error in the normalization would be a dependence of the Bhabha scattering rate on the target gas. Since the ionization energy of the electrons of the target molecules is in the order of eV there is no direct effect. Hence any effect concerning the target gas electrons is independent of the gas molecules.

The target gas has been changed every 40-130 min which defines the time scale on which possible fluctuations in the luminosity monitor signal have an influence on the extraction of $F_2^{\mathrm{n}}/F_2^{\mathrm{p}}$. The observed gain drop of the luminosity monitor calorimeters and photo-multipliers is a smooth decrease of about 10% over 100 days, compared to 1-4 days of data taking in one period and rapid gas changes this can cause a 0.1% effect at most. The overall error of the relative luminosity measurement is 0.64% [Pot96].

The normalization is done using coincidence rates counted with a scaler module which is independent of the DAQ-dead-time, so there is no effect from the DAQ system.

The normalization error within one data taking period is below 0.7%, adding up the three periods results in a final normalization error of 0.4%.

Target Contamination

The gas purity in the target cell depends on the purity of the gas in the gas bottle attached to the gas feed system and on the residual gas in the cell before injection of the target gas. The contamination in the H_2 gas is negligible (1-10 ppm), the contamination of D_2 consists of 0.5% hydrogen and 1-12 ppm tritium. The ratio $F_2^{\mathrm{n}}/F_2^{\mathrm{p}}$ has to be corrected for the hydrogen contamination in the deuterium gas only. The measured number of scattered positrons from the deuterium target with a hydrogen contamination N_m^{D} depends on the partial atomic densities for deuterium and hydrogen ($n_{\mathrm{D}}/n_{\mathrm{H}}$), the measured Bhabha coincidences L_m^{D} depends on the partial electron densities $n_{\mathrm{H/D}}^{\mathrm{e}}$:

$$\begin{aligned}
N_m^{\mathrm{D}} &= F_2^{\mathrm{D}} n_{\mathrm{D}} + F_2^{\mathrm{H}} n_{\mathrm{H}} \\
&= C[F_2^{\mathrm{D}}\xi + F_2^{\mathrm{H}}(1-\xi)] \, , \\
L_m^{\mathrm{D}} &= C(n_{\mathrm{D}}^{\mathrm{e}} + n_{\mathrm{H}}^{\mathrm{e}}) \\
&= C'(\frac{1}{2}n_{\mathrm{D}} + n_{\mathrm{H}}) \\
&= C''(\frac{1}{2}\xi + (1-\xi)) \, ,
\end{aligned} \tag{5.13}$$

with $C/C'/C''$ being constant factors and ξ being the relative deuterium purity of the target gas. Assuming a pure ($\xi = 1$) hydrogen target yields $F_2^{\mathrm{n}}/F_2^{\mathrm{p}}$ is given as: (equation

5.6):

$$\frac{F_2^{\mathrm{n}}}{F_2^{\mathrm{p}}} = \frac{2F_2^{\mathrm{d}}}{F_2^{\mathrm{p}}} - 1$$
$$= \frac{N_m^{\mathrm{D}} L_m^{\mathrm{H}}}{N_m^{\mathrm{H}} L_m^{\mathrm{D}}} \frac{2-\xi}{\xi} - 2\frac{1-\xi}{\xi} - 1 \tag{5.14}$$

For a hydrogen contamination of 0.5% $F_2^{\mathrm{n}}/F_2^{\mathrm{p}}$ is

$$\frac{F_2^{\mathrm{n}}}{F_2^{\mathrm{p}}} = \frac{N_m^{\mathrm{D}} L_m^{\mathrm{H}}}{N_m^{\mathrm{H}} L_m^{\mathrm{D}}} \times 1.0101 - 1.0101 \tag{5.15}$$

which is about a 1% correction. With an uncertainty of 20% on the hydrogen contamination in the deuterium target this results in a 0.2% uncertainty in $F_2^{\mathrm{n}}/F_2^{\mathrm{p}}$.

Another critical issue is the transition between gas changes. After closing of the gas feed system gas bottles the entire system (gas feed system and target chamber) is pumped down to a pressure below 10^{-10} mbar which is 5 orders of magnitude below the cell pressure with target. Since the pressure is proportional to the gas density there is no measurable dilution of the target gas left over after the transition from one target to another.

Momentum Calibration

The beam energy, respectively the beam positrons momentum has only a negligible uncertainty [Gro94, Oel95], only the uncertainty in the scattered positrons momentum contributes to systematic errors. The uncertainty in the determination of the momentum comes from the finite tracking chamber resolution, multiple scattering and from the imperfectness of the implementation of the magnetic field of the spectrometer magnet. The finite tracking chamber resolution and multiple scattering effects are taken into account in the unfolding of the measured distributions (see section 5.1.1), the systematic error is described in the next section. The relative imperfectness of the magnetic field is 10^{-4} [Roe94] and is not taken into account in this analysis.

Uncertainties in the Unfolding

The main error in the unfolding comes from the limited Monte Carlo statistics for both methods, the simple Monte Carlo comparison and the Bayes' algorithm. Another source of systematic errors is the resolution which is put into the Monte Carlo simulation. Varying this input changes the resulting unfolding correction within 1%. The Bayes' method suffers from the low statistics in the edge bins more than the simple method so that at low x the error is bigger. Altogether the statistical errors on both methods give an upper limit for the total error in the unfolding.

The total systematic uncertainty shown in figure 5.7 is the quadratic sum of all contributing systematic uncertainties which gives an upper bound for the total uncertainty.

5.1.6 Discussion of Results

The result on $F_2^{\rm n}/F_2^{\rm p}$ allows a qualitative interpretation according to the arguments discussed in section 2.2.2, chapter 2:

1. for small x the ratio is close to 1 which indicates that the sea quarks, which are assumed to have the same distribution function in the proton and neutron, dominate (see equation 2.27),

2. For large x the ratio goes down indicating that the u-quarks dominate in this region.

The agreement of the HERMES data with previous measurements can also be seen as a confirmation of the analysis techniques.

The Gottfried Sum

As mentioned in section 2.4 the Gottfried sum rule result obtained by the NMC indicates a deviation from the QPM expectations. In the QPM the sum

$$S_G = \int_0^1 \frac{dx}{x}(F_2^{\rm p}(x) - F_2^{\rm n}(x)) = \frac{1}{3} \tag{5.16}$$

can be interpreted in terms of quark distribution functions. Using equation 2.27 on page 9 assuming isospin symmetry between proton and neutron the sum becomes:

$$S_G = \frac{1}{3} + \frac{2}{3}\int_0^1 dx\, [\bar{u}(x) - \bar{d}(x)]\ . \tag{5.17}$$

If the sea is symmetric the last term vanishes and the sum should be 1/3.

The NMC extracted a value for the Gottfried sum using the measured structure function $F_2^{\rm D}(x)$ and the structure function $F_2^{\rm n}/F_2^{\rm p}$:

$$F_2^{\rm p} - F_2^{\rm n} = \frac{1 - F_2^{\rm n}/F_2^{\rm p}}{1 + F_2^{\rm n}/F_2^{\rm p}} 2F_2^{\rm D}\ . \tag{5.18}$$

The data were evaluated at a fixed Q^2 = 4 GeV and yield:

$$S_G = 0.235 \pm 0.026\ , \tag{5.19}$$

which is a definite deviation from the QPM with a symmetric sea. Since the HERMES data agree very well with the NMC data this value of the Gottfried sum is supported also by the HERMES data.

A possible explanation is the asymmetry of the sea which can be measured in semi-inclusive DIS. HERMES in principle will be able to measure a sea quark flavor asymmetry using high density unpolarized targets. In chapter 6, section 6.3 the method and prospectives will be introduced.

5.2 $F_2^{^3\mathrm{He}}/F_2^{\mathrm{D}}$

As mentioned earlier there are two motivations for HERMES to measure $F_2^{^3\mathrm{He}}/F_2^{\mathrm{D}}$, to get a measurement of $F_2^{^3He}$ which enters directly into the extraction of g_1^{n} from the observed spin asymmetry on $^3\mathrm{He}$ and as a measurement of nuclear effects on the structure function for $^3\mathrm{He}$.

To be able to compare F_2 for different nuclei one normalizes it to the *"mean"* F_2 of proton and neutron which is assumed to be the structure function F_2^{D} of the deuteron. The comparison of isoscalar targets is done comparing the ratios $F_2^{\mathrm{A}}/F_2^{\mathrm{D}}$, whereas for non-isoscalar targets it involves an isoscalar correction function to the measured $F_2^{\mathrm{N,Z}}$. The correction function only depends on $F_2^{\mathrm{n}}/F_2^{\mathrm{p}}$:

$$\frac{1}{2}(F_2^{\mathrm{n}}+F_2^{\mathrm{p}}) \equiv f_{\mathrm{iso}}(F_2^{\mathrm{n}}/F_2^{\mathrm{p}})\frac{1}{N}(ZF_2^{\mathrm{p}}+NF_2^{\mathrm{n}})\ . \tag{5.20}$$

The isoscalar correction function then is:

$$f_{\mathrm{iso}}(F_2^{\mathrm{n}}/F_2^{\mathrm{p}}) = \frac{A}{2}\frac{1+F_2^{\mathrm{n}}/F_2^{\mathrm{p}}}{(Z+NF_2^{\mathrm{n}}/F_2^{\mathrm{p}})}\ . \tag{5.21}$$

With the luminosity coincidence rate L_{c} being proportional to the electron density ($\rightarrow$ Z) the isoscalar structure function ratio $F_2^{^3\mathrm{He}}/F_2^{\mathrm{D}}$ ($F_2^{^3\mathrm{He}}/F_2^{\mathrm{D}}$ in this text always refers to the isoscalar corrected ratio) is determined from experimental quantities using:

$$F_2^{^3\mathrm{He}}/F_2^{\mathrm{D}} = \frac{N_{\mathrm{e+}}^{^3\mathrm{He}}\cdot f_{\mathrm{iso}}(F_2^{\mathrm{n}}/F_2^{\mathrm{p}})}{N_{\mathrm{e+}}^{\mathrm{D}}\cdot\frac{3/2L_{\mathrm{c}}^{^3\mathrm{He}}}{2L_{\mathrm{c}}^{\mathrm{D}}}} \tag{5.22}$$

using a parameterization for $F_2^{\mathrm{n}}/F_2^{\mathrm{p}}$. For HERMES this means that by taking the data on $^3\mathrm{He}$, D_2 and H_2 one does not have to explicitly apply a correction but one can divide the $^3\mathrm{He}$ structure function data by the sum of the D_2 and H_2 data:

$$F_2^{^3\mathrm{He}}/F_2^{\mathrm{D}} = \frac{3N_{\mathrm{e+}}^{^3\mathrm{He}}\frac{2L_{\mathrm{c}}^{\mathrm{D}}}{3/2L_{\mathrm{c}}^{^3\mathrm{He}}}}{2N_{\mathrm{e+}}^{\mathrm{D}}+N_{\mathrm{e+}}^{\mathrm{H}}\cdot\frac{2L_{\mathrm{c}}^{\mathrm{D}}}{L_{\mathrm{c}}^{\mathrm{H}}}} \tag{5.23}$$

which directly gives the corrections to be applied when approximating $^3\mathrm{He}$ with the sum of deuteron and proton to extract the spin structure function g_1^{n}. Usually the isoscalar correction is used with a parameterization of $F_2^{\mathrm{n}}/F_2^{\mathrm{p}}$ to compare structure function with F_2^{D}, comparing $^3\mathrm{He}$ with $2F_2^{\mathrm{D}}+F_2^{\mathrm{H}}$ is actually the same as using the HERMES $F_2^{\mathrm{n}}/F_2^{\mathrm{p}}$ parameterization. For this analysis only HERMES data are used to obtain $F_2^{^3\mathrm{He}}/F_2^{\mathrm{D}}$.

5.2.1 Results

The extraction of the ratio $F_2^{^3\mathrm{He}}/F_2^{\mathrm{D}}$ is similar to the extraction of $F_2^{\mathrm{n}}/F_2^{\mathrm{p}}$. The same analysis software is used to obtain distributions in Q^2 and x. The radiative correction input parameters have been adjusted assuming that $F_2^{^3\mathrm{He}}$ is the sum of the deuteron and proton structure function. Parameterizations for the elastic and quasi-elastic tails for $^3\mathrm{He}$ have been taken from [Whi74] and [Shi64]. The data of the three $\mathrm{H_2/D_2}$ periods are compared with spin averaged $^3\mathrm{He}$ data from different data taking periods. Since the deviation of the

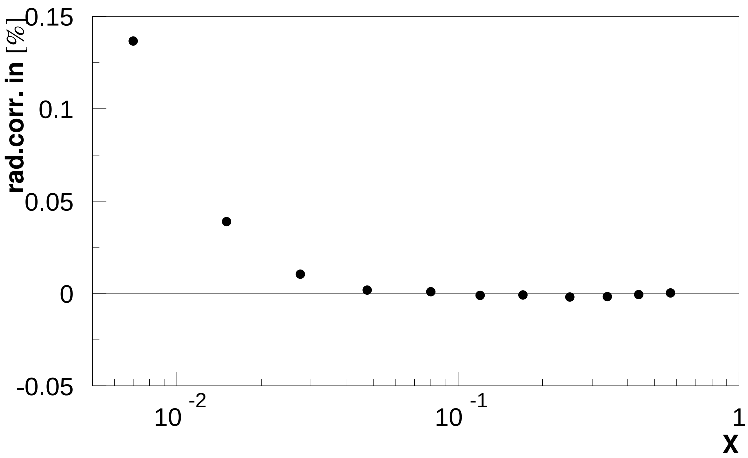

Figure 5.11: Relative radiative corrections to $F_2^{^3\mathrm{He}}/F_2^{\mathrm{D}}$ for each x-bin.

structure function $F_2^{^3\mathrm{He}}$ from the structure function $F_2^{\mathrm{D+H}}$ for the combined $\mathrm{H_2/D_2}$ data is very small, the radiative corrections as well as unfolding corrections are smaller than for $F_2^{\mathrm{n}}/F_2^{\mathrm{p}}$. The unfolding corrections are below 1% and are not applied here since the uncertainty itself is in the order of 1%. The radiative corrections are applied, figure 5.11 shows the relative correction for each x-bin. Except for the lowest x-bin the correction is below 5%.

The major difference in the extraction of $F_2^{^3\mathrm{He}}/F_2^{\mathrm{D}}$ with respect to the extraction of $F_2^{\mathrm{n}}/F_2^{\mathrm{p}}$ is that the $^3\mathrm{He}$ data sample has to be taken from a different data taking period. Variations in the luminosity monitor response as well as in the overall spectrometer efficiency with time do not cancel out since the data sets for $\mathrm{H_2}$, $\mathrm{D_2}$ and $^3\mathrm{He}$ are taken at different times. The normalization between the $\mathrm{H_2/D_2}$ and $^3\mathrm{He}$ data is done using the luminosity monitor including a gain correction, other corrections for DAQ-lifetime and efficiencies are applied in the same way to the $^3\mathrm{He}$ data as to the $\mathrm{H_2/D_2}$ data. The $^3\mathrm{He}$ data taken between period I and II are spin averaged and analyzed in the same way as the $\mathrm{H_2/D_2}$ data described in the previous chapter. The statistics of the $^3\mathrm{He}$ data is the same as the one for the combined $\mathrm{H_2/D_2}$ data.

In figure 5.12 the result on $F_2^{^3\mathrm{He}}/F_2^{\mathrm{D}}$ is plotted for each of the $\mathrm{H_2/D_2}$ periods separately. The ratio is expected to be close to one. The data for the three independent data

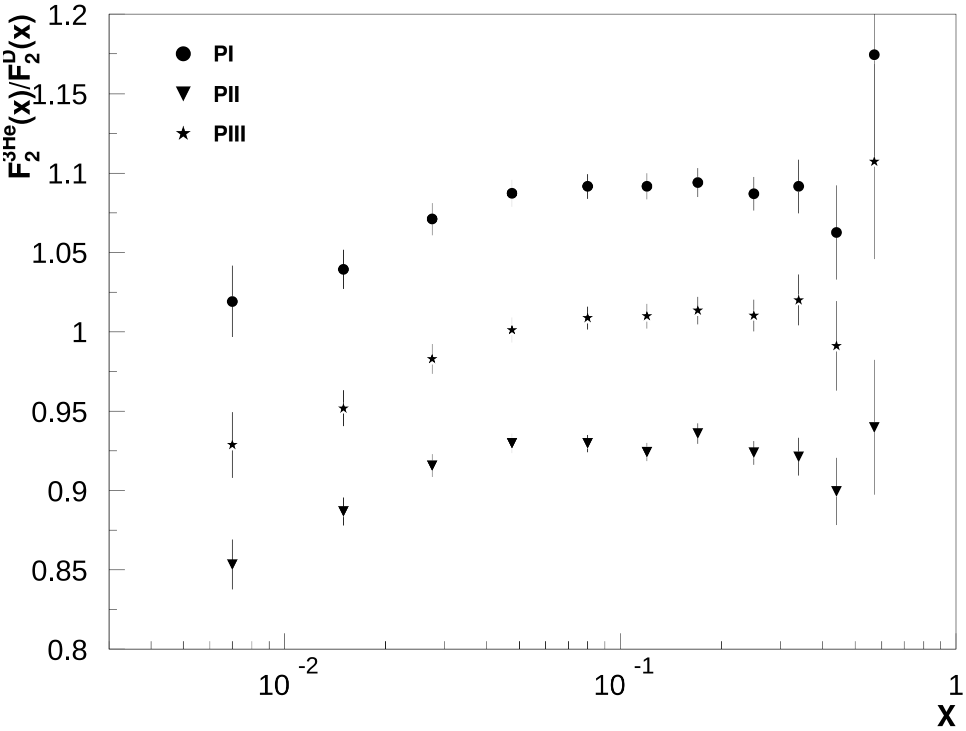

Figure 5.12: The ratio $F_2^{^3\mathrm{He}}/F_2^{\mathrm{D}}$ using HERMES data on $^3\mathrm{He}$, $\mathrm{H_2}$ and $\mathrm{D_2}$ for the three $\mathrm{H_2/D_2}$ periods separately. The gain correction to the luminosity monitor is used in the normalization, the errors are only statistical.

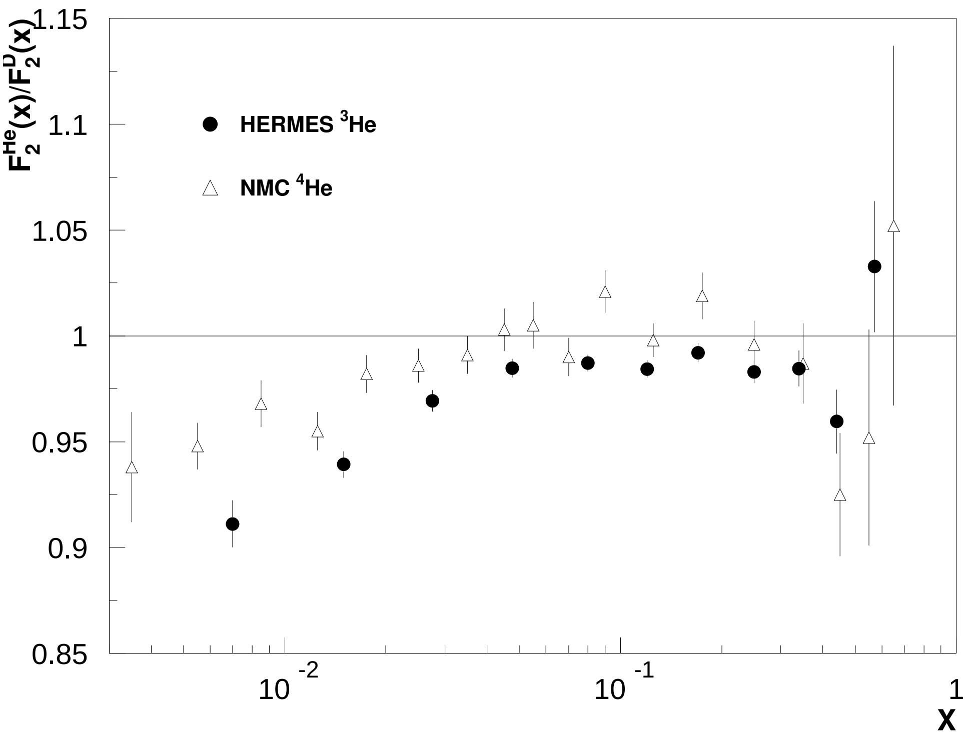

Figure 5.13: The ratio $F_2^{^3\mathrm{He}}/F_2^{\mathrm{D}}$ using HERMES data on $^3\mathrm{He}$, H_2 and D_2 . For comparison the NMC data on $F_2^{^4\mathrm{He}}/F_2^{D}$ is plotted, the errors are statistical. The HERMES data have a large (10%) normalization uncertainty which is not shown!

taking periods do not agree in their normalization and the ratio deviates about 10% from its expected value 1 for period I and II. This clearly indicates normalization difficulties when comparing results from different data taking periods. As discussed in the previous chapter the normalization over short time periods is very precise. In contrast to the measurement of $F_2^{\mathrm{n}}/F_2^{\mathrm{p}}$, where the structure function ratio itself is combined from the three periods and the normalization of the periods against each other drops out, for the extraction of $F_2^{^3\mathrm{He}}/F_2^{\mathrm{D}}$ the normalization of the $\mathrm{H}_2/\mathrm{D}_2$ and the $^3\mathrm{He}$ data taking periods has to be known. The uncertainties are large if one compares data taken under different detector conditions. The observed discrepancy between period I, II and III can be explained with a variation in the measured luminosities with time. The gain correction applied is not yet finalized and has to be studied further. In addition a detailed analysis of the variation of detector and DAQ efficiencies over large time scales has to be done.

Figure 5.13 shows the result for $F_2^{^3\mathrm{He}}/F_2^{\mathrm{D}}$ as determined with the full $\mathrm{H}_2/\mathrm{D}_2$ data and approximately the same statistic of spin averaged data on $^3\mathrm{He}$. Apart from the normalization uncertainty of about 10% the data indicate nuclear effects on the structure function for $^3\mathrm{He}$. The decrease of the structure function ratio at low x is an indication of shadowing, whereas the decrease for $x \approx 0.3 - 0.5$ shows the EMC-effect for $^3\mathrm{He}$. Compared to the $^4\mathrm{He}$ data from the NMC with the current uncertainty in the normalization one can not deduce further quantitative results, although the data indicate a slightly smaller EMC-effect for $^3\mathrm{He}$.

In 1996 HERMES is taking data with unpolarized hydrogen, deuterium and helium with comparable statistics to the here described data sample. It is planned to switch between all three gases during a HERA positron fill every 10 days. This avoids the large normalization uncertainties and will give a precise measurement of the structure function ratio.

For the extraction of the spin structure function g_1^{n} from the 1995 polarized data, a normalization correction of 3% to the combined data on $F_2^{^3\mathrm{He}}/F_2^{\mathrm{D}}$ can be used.

Chapter 6

First Semi-inclusive Results

This chapter describes the first analysis of semi-inclusive data taken with the unpolarized targets in 1995. The semi-inclusive analysis of these data is still in progress and there is no final result yet. Nevertheless a few qualitative remarks to these first semi-inclusive data show the possibilities HERMES has. The main problem with the semi-inclusive analysis of the 1995 data is the pion identification. Since the threshold of the Cerenkov detector was relatively high the fraction of hadrons which can be identified as pions is low (12%). Nevertheless instead of using a pure pion sample and the known fragmentation functions of quarks into pions (see figure 6.3) a hadron sample can be used. The charge of hadrons detected also reflects the flavor of the struck quark. For the valence region positive hadrons originate mostly from u-quarks, negative mostly from d-quarks. To increase the statistics the analysis described here is mostly based on the entire hadron sample from the $\mathrm{H}_2/\mathrm{D}_2$ data taken in 1995.

As described in section 2.3 the measurement of hadrons in addition to the scattered lepton yields information on the flavor of the struck quark. The multiplicity of a hadron h in the final state of DIS off the nucleon N is given by:

$$\frac{1}{\sigma_{\mathrm{tot}}}\frac{d\sigma^h_{\mathrm{N}}(x,z)}{dz} = \frac{\sum_i e_i^2 f_{i/\mathrm{N}}(x) D_i^h(z)}{\sum_i e_i^2 f_{i/\mathrm{N}}(x)} = \frac{1}{N_e}\frac{dN^h}{dz}\ , \tag{6.1}$$

with N_e being the total number of scattered positrons and N^h the total number of detected hadrons of type h. Here factorization and scaling is assumed.

The major difference in measuring these hadron multiplicities on different targets with respect to inclusive measurements is that there is no normalization involved. The hadron multiplicities are hence independent of detector efficiencies provided there is no charge or space dependence of the efficiency. Since the distribution of hadrons is expected to be symmetric in φ and the spectrometer is symmetric the acceptance of oppositely charged hadrons is expected to be the same. As a cross check the ratio of negative and positive hadrons in the right and left detector is plotted in figure 6.1. Since the vertical magnetic field of the spectrometer magnet deflects oppositely charged hadrons into opposite direc-

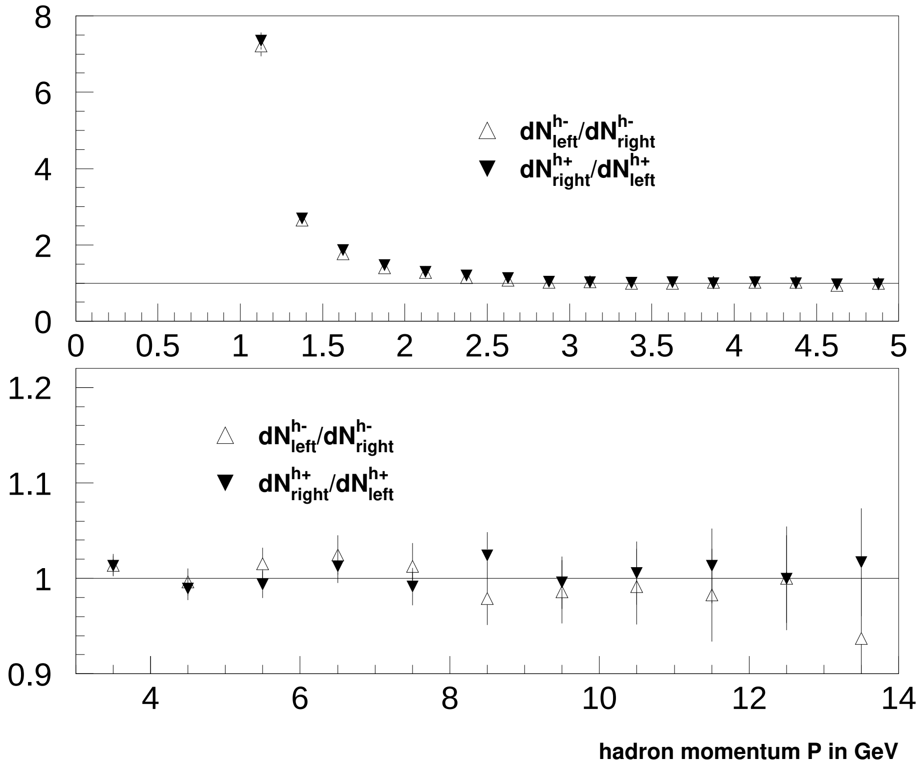

Figure 6.1: Acceptance for opposite charged hadrons in the left and right detector half. The upper plot shows the region for low hadron momenta, the lower shows the high momentum region (see text). All errors are statistical.

tions, the ratio of positive(negative) hadrons in the right and left detector half is expected to deviate from one as the momentum decreases and hence the deflection angle increases. For a momentum lower than 2 GeV the hadrons with large scattering angles are partially deflected out of the acceptance of the back part of the spectrometer, depending on the charge, hadrons are predominantly lost in the left or right detector part. The upper plot in figure 6.1 shows the low momentum region, the ratio *left/right* for positive and *right/left* multiplicity for negative hadrons exactly reflects the expectation, nevertheless the effect on the integral number of measured hadrons for each charge cancels since the loss is symmetric so that there is no charge dependent acceptance within the statistical error bars.

As mentioned above, a crucial issue for semi-inclusive physics is the identification of different hadrons. Since the major goal of HERMES in 1995 was the extraction of g_1^n. The PID has been optimized for positron-hadron separation. As explained in section 4.3.3 the Cerenkov detector can be used to separate pions from heavier hadrons. Figure 6.2 shows

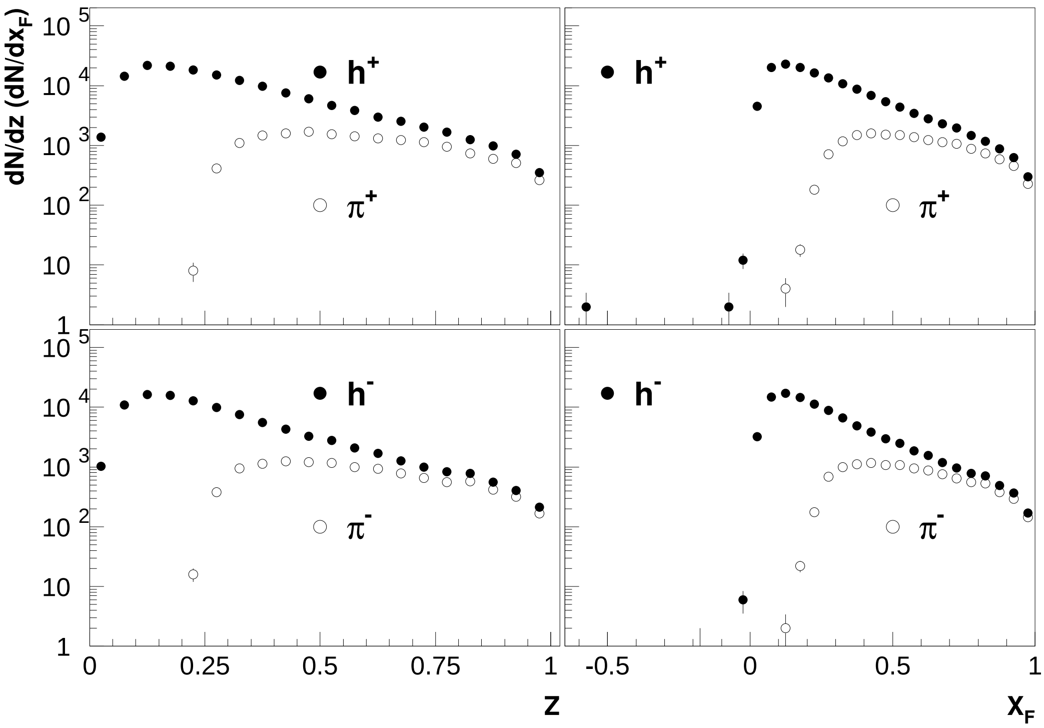

Figure 6.2: Absolute number of hadrons/pions. The pion sample (open circles) are identified with the Cerenkov with a high (5.5 GeV) threshold. The upper plots show positive, the lower negative charged yields.

total yield of hadrons and the identified pions using the Cerenkov detector. The yields for positive and negative charged hadrons/pions are plotted versus z (right plots) and x_{F} (left plots). There are no hadrons detected for $x_{\mathrm{F}} < 0$ which indicates that they predominantly originate from the *current region*. The momentum threshold of 5.5 GeV of the Cerenkov detector corresponds to a minimum z of 0.25 for identified pions. This is reflected in the x_{F}-distribution of the pions which shows a steep rise of the yield for $x_{\mathrm{F}} < 0.1$. The identified pions hence are most likely from the current region. For large values of z and x_{F} most of the hadrons can be identified as pions.

In order to obtain information on the quark distributions $f_{i/\mathrm{N}}(x)$ one has to know the fragmentation functions $D_i^h(z)$. Figure 6.3 shows the favored and unfavored fragmentation functions for pions ($D^+,\ D^-$ as defined in equation 2.45) measured by the EMC [Arn89]. At high values of z the favored fragmentation function is is much larger than

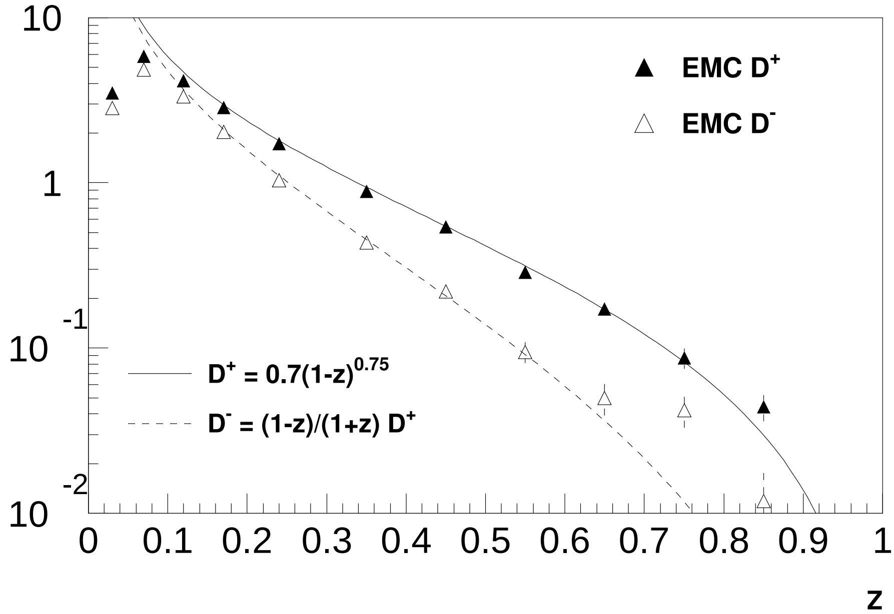

Figure 6.3: Pion fragmentation functions as measured by the EMC. The solid line corresponds to parameterization fitted to the favored (D^+) fragmentation function, the dashed line is suppressed by a factor of $(1-z)/(1+z)$ for the unfavored fragmentation function.

the unfavored, a fit to the data suggested by Feynman and Field [Fie78] indicates that $D^+ = (1+z)/(1-z)D^-$ which is confirmed by the EMC data for intermediate values of z, for very small values of z the fragmentation model fails to describe the data and the *target region* dilutes the pion sample. HERMES is able to measure the fragmentation functions using only the pion multiplicities obtained with the isoscalar deuteron target. However a detailed Monte Carlo study has to be performed in order to be able to get a precise acceptance for semi-inclusive events. These studies also involving detailed studies of existing Monte Carlo generators for the HERMES kinematic range are currently in progress [Ihs96].

Kinematic cuts have been applied to all semi-inclusive data used for this analysis:

1. a Q^2-cut at $Q^2 > 1 \text{ GeV}^2$ has been applied to ensure that the assumptions made for the fragmentation process do hold,

2. a cut on $y < 0.85$ ensures that radiative effects are small,

3. a cut on $W^2 > 6.0 \ GeV^2$ makes sure that no hadrons from resonance decays dilute the hadron multiplicities and

4. an acceptance cut on $\theta_y > 0.04 \ mrad$ as well as a cut on the vertex position, $-20 \ cm < Z_{vertex} < 20 \ cm$ avoids regions where the acceptance could differ for differently charged hadrons.

Except for the higher Q^2-cut these cuts correspond to the cuts used for the inclusive analysis (see section 5.1.2). The data analysis is similar to the inclusive analysis described in chapter 4 with respect to the PID and detection of scattered positrons. All events with a scattered positron and at least one hadron are selected. The logarithm of the PID likelihood (see section 4.3.3) for a hadron has to be below -1 ($\log(\mathcal{L}^e) > 0$ for positrons) to reduce the lepton contamination in the hadron sample. The charge of the hadron is determined via its deflection in the spectrometer magnet. For identification of the pions the method described in section 4.3.3 using the Cerenkov signal for hadrons with momenta larger than 5.5 GeV is used.

6.1 Charge Multiplicity Ratios

The QPM assigns each nucleon three valence and additional sea quarks, as the measurement of $F_2^{\rm n}/F_2^{\rm p}$ shows (see section 5.1), the sea quarks dominate at low x whereas the valence quarks dominate at large x with an excess of u-valence quarks at very large x. In a simplified picture this result can be verified qualitatively with a semi-inclusive measurement of charge multiplicity ratios on different targets.

Assuming the fragmentation of positively charged quarks yields predominantly positive hadrons, the hadron charge multiplicity ratio dN^{h^+} and dN^{h^-} should be different at large x for the proton and neutron. To obtain this ratio for the neutron one has to combine the deuteron and hydrogen data under the assumption that the deuteron is the sum of the proton and the neutron using the measured ratio $F_2^{\rm n}/F_2^{\rm p}$:

$$\frac{1}{N_{e+}^{\rm n}}\frac{dN_n^{h\pm}}{dz} = \left(1+\frac{F_2^{\rm p}}{F_2^{\rm n}}\right)\frac{1}{N_{e+}^{\rm d}}\frac{dN_d^{h\pm}}{dz} - \frac{F_2^{\rm p}}{F_2^{\rm n}}\frac{dN_{\rm p}^{h\pm}}{dz} \tag{6.2}$$

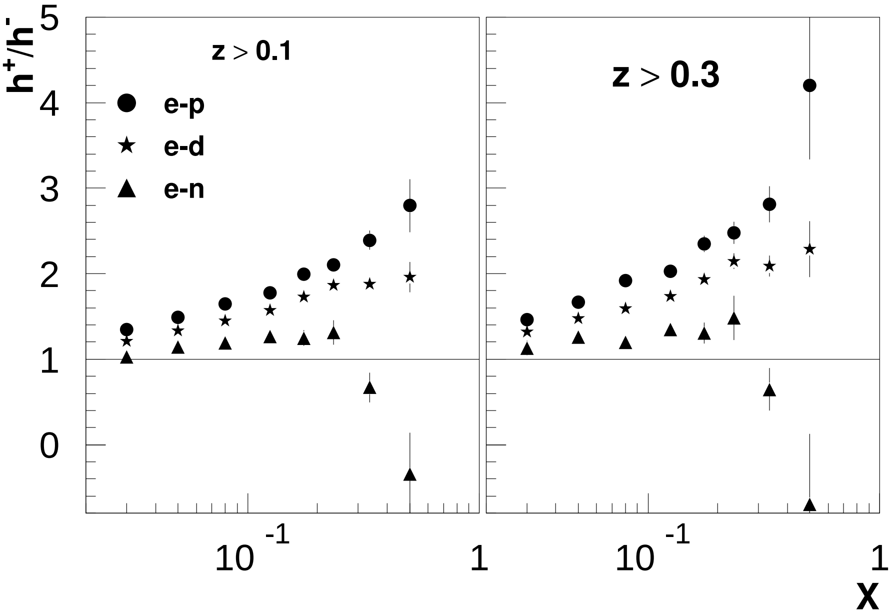

Figure 6.4: The charge multiplicity ratio versus x for hadrons for two different z cuts (see text). Only statistical errors are shown.

Figure 6.4 shows the charge multiplicity ratio for the deuteron, proton and neutron versus x for two different z cuts. The ratio on the proton increases with x indicating the large excess of the u-quarks in the valence region, for the deuteron it still increases whereas for the neutron it stays above unity for low x and falls below for high x. Since the virtual photon coupling to a quark is proportional to the square of the quark charge, even for the isoscalar deuteron an increase is expected since the valence quarks have different charges. The same can be seen for the neutron, the ratio is above unity over a large range although the photon and neutron are electrically neutral. Since the charge of the u-quark is 2/3 of an electron charge and the d-quark charge is only 1/3, a neutron containing two d and one u quark explains the observed behavior qualitatively. The drop of the ratio at large x reflects the result already seen in the structure function ratio $F_2^{\mathrm{n}}/F_2^{\mathrm{p}}$, a domination of the d-quark in the neutron for large x, which under isospin invariance means the same domination of the u-quark in the proton.

As mentioned in section 2.3 the probability for a detected hadron originating from the *current fragmentation region* rises with the fractional energy z of the hadron. The target fragments would dilute the charge differences so one expects the differences in the charge multiplicity ratio between the proton and neutron to increase with a minimum z-cut. In figure 6.4 the ratios are shown for $z_{\mathrm{min}} = 0.1$ and $z_{\mathrm{min}} = 0.3$, the differences are slightly enhanced for the higher z-cut. The fact that the effect is very small indicates that the HERMES spectrometer has a very small acceptance for the *target fragmentation region* compared to the *current fragmentation region*. Detailed Monte Carlo studies have to be performed to quantify this point. The problem with these Monte Carlo studies is that the fragmentation at HERMES energies is not yet theoretically understood, all existing fragmentation models and their implementation into Monte Carlo generators are valid for much higher values of Q^2 and are currently being modified to incorporate the HERMES kinematical range.

6.2 Valence Quark Distribution Ratios

Assuming only two different fragmentation functions for the light quarks (see equation 2.45) and defining the valence quark distribution as:

$$q_v(x) = q(x) - q_{\mathrm{sea}}(x) \ , \tag{6.3}$$

the sea contribution cancels exactly in the difference of charge multiplicities since the number of positive hadrons produced on the quarks is equal to the number of negative hadrons produced on the anti-quarks and vice versa. Assuming isospin invariance the valence quark distributions can be defined as $u_v(x) := u_v^{\mathrm{p}} = d_v^{\mathrm{n}}$ and $d_v(x) := u_v^{\mathrm{n}} = d_v^{\mathrm{p}}$ (see section 5.1 equation 2.25). The pion charge multiplicity differences for neutron and proton are then (using equation 6.1):

$$\begin{aligned}
\frac{1}{N^{\mathrm{p}}_{e+}}\left(\frac{dN^{\pi^+}_{\mathrm{p}}}{dz}-\frac{dN^{\pi^-}_{\mathrm{p}}}{dz}\right)dz &= \frac{x}{F^{\mathrm{p}}_2}\left(\frac{4}{9}u_v-\frac{1}{9}d_v\right)(D^+-D^-)dz\ ,\\
\frac{1}{N^{\mathrm{n}}_{e+}}\left(\frac{dN^{\pi^+}_{\mathrm{n}}}{dz}-\frac{dN^{\pi^-}_{\mathrm{n}}}{dz}\right)dz &= \frac{x}{F^{\mathrm{n}}_2}\left(\frac{4}{9}d_v-\frac{1}{9}u_v\right)(D^+-D^-)dz\ . \qquad (6.4)
\end{aligned}$$

For fixed Q^2 equations 6.4 can be solved for $d_v(x)/u_v(x)$ in terms of the measured ratio $R^\pi(x)$:

$$R^\pi(x) := \frac{\frac{1}{N^n_{e+}}\int\left(\frac{dN^{\pi^+}_n}{dz}(x)-\frac{dN^{\pi^-}_n}{dz}(x)\right)dz}{\frac{1}{N^p_{e+}}\int\left(\frac{dN^{\pi^+}_p}{dz}(x)-\frac{dN^{\pi^-}_p}{dz}(x)\right)dz}\frac{F^n_2(x)}{F^p_2(x)}\ . \qquad (6.5)$$

In this ratio the fragmentation functions cancel. The EMC [Ash91] suggests a correction to the ratio for measuring all charged hadrons instead of a pure pion sample. This means that the fragmentation into charged kaons, protons and anti-protons has to be taken into account. To be able to compare the HERMES results with EMC results this correction is applied also to the HERMES data. Taking equation 6.4 the correction Δ contains only the fragmentation functions and is independent of x:

$$\Delta = 1-\frac{\int(D^{h^-}_d-D^{h^+}_d)dz}{\int(D^{h^-}_u-D^{h^+}_u)dz}\ , \qquad (6.6)$$

Δ has been estimated by the LUND group (see [Ash91]) to be 0.4 ± 0.1. To obtain neutron multiplicities the weighted difference of the deuterium and proton data is used:

$$\frac{1}{N^n_{e+}}\frac{dN^\pm_n}{dz} = \left(1+\frac{F^p_2}{F^n_2}\right)\frac{1}{N^d_{e+}}\frac{dN^\pm_d}{dz}-\frac{F^p_2}{F^n_2}\frac{dN^\pm_p}{dz}\ . \qquad (6.7)$$

The ratio $R^h(x)$ for hadrons is then:

$$R^h(x) := \frac{\frac{1}{N^d_{e+}}\int\left(\frac{dN^{h^+}_d}{dz}(x)-\frac{dN^{h^-}_d}{dz}(x)\right)dz}{\frac{1}{N^p_{e+}}\int\left(\frac{dN^{\pi^+}_p}{dz}(x)-\frac{dN^{\pi^-}_p}{dz}(x)\right)dz}\left(1+\frac{F^n_2(x)}{F^p_2(x)}\right)-1\ . \qquad (6.8)$$

The ratio $d_v(x)/u_v(x)$ for hadrons is calculated from the measured ratios like:

$$\frac{d_v(x)}{u_v(x)} \stackrel{\pi}{=} \frac{4R^\pi(x)+1}{4+R^\pi} \stackrel{h}{=} \frac{4R^h(x)+1-\Delta}{4+R^h(1-\Delta)}\ . \qquad (6.9)$$

Figure 6.5 shows the HERMES result for hadrons and pions separately together with the EMC data and fits to parton distribution from the CTEQ3M [Lai95] at $Q^2 = 1.6\ GeV^2$. In the analysis no Q^2-dependence is assumed, the dependence in the HERMES kinematical range is assumed to be small as seen in the analysis of $F_2^{\mathrm{n}}/F_2^{\mathrm{p}}$. The data are not corrected for smearing and there is no radiative correction applied. Both corrections are assumed to be small. Within the statistical errors the HERMES data agree well with the EMC data. Two measurements from neutrino and anti-neutrino experiments (CDHS [Abr84] and WA21/25 [All84],[Jon94]) do also agree within the errors. The HERMES data indicate a slight difference at low x from the other experiments and the fits. A cut on z is applied to the hadron sample, $z > 0.1$ avoids the region where the sample is most likely diluted by target fragments. For the pion sample this is not necessary since the momentum cut applied for PID with the Cerenkov corresponds to a z-cut of 0.25 (see figure 6.2). The fact that both measurements, the one with all hadrons and the one with a pure pion sample do agree very well within the statistical errors indicates that there is no large dilution of the hadron sample from target fragments This result again indicates the effect that the u-quark dominates at large x which was already seen in the results on $F_2^{\mathrm{n}}/F_2^{\mathrm{p}}$. The naive QPM expectation for the ratio $d_v(x)/u_v(x) = 0.5$ independently of x assuming exact SU(6) symmetry is clearly violated as seen already in the result of $F_2^{\mathrm{n}}/F_2^{\mathrm{p}}$.

Remember that the sea contribution drops out in this method and the fundamental sum rules (see equation 2.46):

$$\int_0^1 u_v(x)\, dx = 2 \quad \text{and} \quad \int_0^1 d_v(x)\, dx = 1 \ , \tag{6.10}$$

have to be fulfilled. Since the ratio is lower than 0.5 for large x it has to be larger at small x somewhere. The HERMES data are in agreement with this prediction too. With higher statistics from the 1996 data and improved understanding of the systematic uncertainties HERMES can contribute another high precision measurement of $d_{\mathrm{v}}/d_{\mathrm{v}}$.

6.3 The Sea Quark Flavor Asymmetry

As already mentioned in the previous sections the naive QPM expectation is that the light sea quarks are flavor symmetric, meaning there are as many $\bar{d} - d$- as $\bar{u} - u$-pairs in the nucleon sea. However there is no physical reason why this should be true. Experimental data on the Gottfried Sum Rule (GSR) can be explained with a flavor asymmetric sea. Defining:

$$\tau(x) = u(x) - d(x) \ \text{and} \ \bar{\tau}(x) = \bar{u}(x) - \bar{d}(x) \ , \tag{6.11}$$

the Gottfried sum can be written as:

$$\Rightarrow S_G = \frac{1}{3}\int_0^1 (\tau(x) - \bar{\tau}(x))dx \equiv \frac{1}{3}(T - \bar{T}) \ , \tag{6.12}$$

with $T, \bar{T}$ contributions of quark, antiquark of the nucleon. As stated before the semi-inclusive cross section (equ. 6.1) can be interpreted with the number of $N^h(x,z)$ of

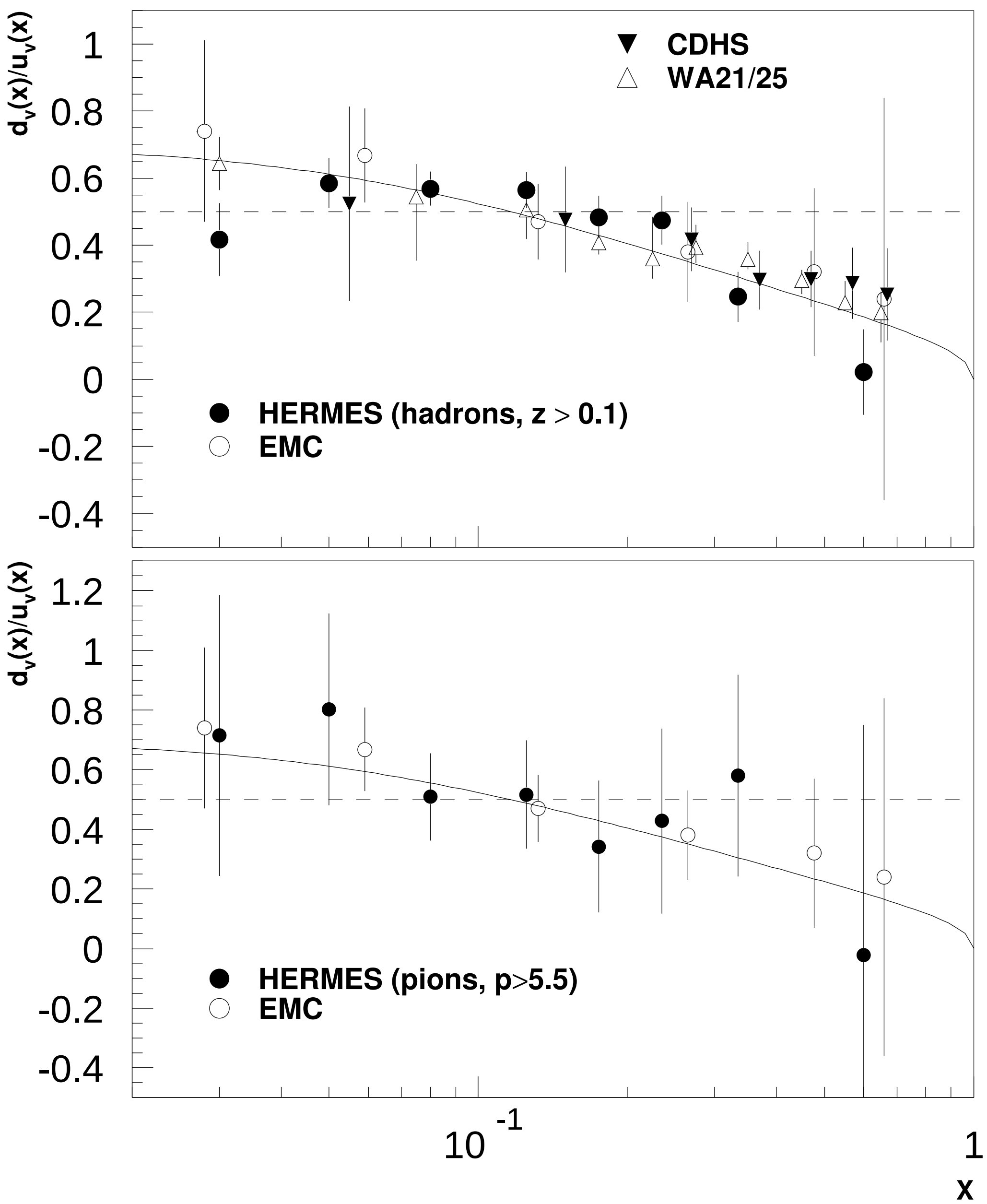

Figure 6.5: The valence quark distribution function ratio (statistical errors only for HERMES , for WA21/25, EMC and CDHS stat. and sys. error is combined). The upper plot shows the HERMES and EMC result using all hadrons. The triangles are measurements from neutrino/anti-neutrino experiments. The line is the CTEQ3M parameterization for the valence quark distribution functions. The lower plot shows the same EMC data and CTEQ fit but with HERMES data using the pion PID, in which case the correction for the hadron fragmentation functions is not needed. The dashed lines indicate the naive QPM expectation with exact SU(6) symmetry.

detected hadrons and the number N_{e^+} of detected positrons like

$$\frac{1}{\sigma_N(x)}\frac{d\sigma_N^h(x,z)}{dz} = \frac{\sum_i e_i^2 f_{iN}(x) D_i^h(z)}{\sum_i e_i^2 f_{iN}(x)} \sim \frac{N_h(x,z)}{N_{e^+}(x)} \ . \tag{6.13}$$

Using the fragmentation functions $D_i^{\pm}$ for a quark of flavor i fragmenting into positive/negative pion (or hadron) and the quark charges and distribution functions for only the light quarks including the strange quarks these numbers for the proton are:

$$\begin{aligned} N^{p\pi\pm} =& \\ & \frac{4}{9}uD_u^{\pm}(z) + \frac{4}{9}\bar{u}D_{\bar{u}}^{\pm}(z) + \frac{1}{9}dD_d^{\pm}(z) + \\ & \frac{1}{9}\bar{d}D_{\bar{d}}^{\pm}(z) + \frac{1}{9}sD_s^{\pm}(z) + \frac{1}{9}\bar{s}D_{\bar{s}}^{\pm}(z) \end{aligned} \tag{6.14}$$

and for the neutron assuming isospin invariance:

$$\begin{aligned} N^{n\pi\pm} =& \\ & \frac{4}{9}dD_u^{\pm}(z) + \frac{4}{9}\bar{d}D_{\bar{u}}^{\pm}(z) + \frac{1}{9}uD_d^{\pm}(z) + \\ & \frac{1}{9}\bar{u}D_{\bar{d}}^{\pm}(z) + \frac{1}{9}sD_s^{\pm}(z) + \frac{1}{9}\bar{s}D_{\bar{s}}^{\pm}(z) \ . \end{aligned}$$

Using the result from equation 2.45 one defines a ratio:

$$R(x,z) = \frac{\tau(x) - \bar{\tau}(x)}{\tau(x) + \bar{\tau}(x)} \left(\frac{3D^+(z) + 3D^-(z)}{5D^+(z) - 5D^-(z)} \right) \tag{6.15}$$

and uses the parameterization of the ratio of the fragmentation functions (Feynman $\&$ Field, EMC [Fie78][Arn89]):

$$D^+ = (1+z)/(1-z)D^- \ , \tag{6.16}$$

so that $R(x,z)$ bocomes independent of the fragmentation functions:

$$R(x,z) = \frac{\tau(x) - \bar{\tau}(x)}{\tau(x) + \bar{\tau}(x)}\frac{3}{5}\frac{1}{z} \ . \tag{6.17}$$

The integral over this ratio is then directly proportional to the Gottfried sum:

$$\int_0^1 R(x,z)dx = 3S_{\mathrm{G}}\frac{3}{5z} \ . \tag{6.18}$$

The ratio $R(x,z)$ in turn is proportional to the actually measured ratio $r(x,z)$:

$$r(x,z) = \frac{N^{\mathrm{p}\pi-} - N^{\mathrm{n}\pi-}}{N^{\mathrm{p}\pi+} - N^{\mathrm{n}\pi+}} \Rightarrow R(x,z) = \frac{1 + r(x,z)}{1 - r(x,z)} \ . \tag{6.19}$$

By measuring the z dependence of the ratio $r(x,z)$ the sea quark flavor asymmetry can be extracted. Figure 6.6 shows a first measurement using the HERMES $\mathrm{H_2/D_2}$ data. Due to the low statistics of the pure pion sample the ratio is measured for all hadrons. A cut on x is applied, $x < 0.3$ because the contribution of the sea becomes too small for higher values and $x > 0.1$ because for smaller values the absolute charge difference becomes increasingly small (see figure 6.4) and the ratio is difficult to measure (the ratio becomes a ratio of two very small differences in the denominator and enumerator and the error becomes very large). Estimates using a LUND Monte Carlo simulation for the statistical error $\delta r(x,z)$ in the ratio $r(x,z)$ are shown in table 6.1 [Jac92] for the kinematical region of interest for the HERMES data. The table shows that around $\bar{x} = 0.2$ the relative error has

$\bar{x}$	$0.3 \leq z \leq 0.4$ $\delta r(x,z)$	$0.5 \leq z \leq 0.6$ $\delta r(x,z)$
0.05	± 0.18	± 0.12
0.20	± 0.08	± 0.05
0.45	± 0.24	± 0.66
$r(x,z)_{\mathrm{predicted}}$	$+0.27$	$+0.05$

Table 6.1: Monte Carlo estimates for $\delta r(x,z)$ in measuring the sea quark flavor asymmetry. 300 hours of data taking with $\mathrm{H_2/D_2}$ targets at a thickness of $10^{14}\frac{\mathrm{nucl.}}{\mathrm{cm^2}}$ and a perfect pion identification for hadrons with a momentum larger than 5 GeV were assumed.

a minimum. The lines indicate expectations for $r(z)$ for different assumptions. The upper line shows the expectation for a flavor symmetric sea, the middle line is the expectation for the NMC results on the Gottfried sum assuming that flavor asymmetry is the origin for the deviation from 1/3 ($S_G = 0.2235 \pm 0.0226$ [Arn94]). The lowest line represents a sea characterized by $(\tau - \bar{\tau})/(\tau + \bar{\tau}) = 0.5$. The data are in agreement with the NMC prediction within the statistical errors. The lowest point in z reflects the fact that the fragmentation does not reflect the current fragments anymore. The HERMES data cannot decide between these curves yet since there is no correction going in for the fact that all hadrons enter into the determination of $r(x,z)$, which was derived for a pure pion sample. Using a pure pion sample with higher statistics will yield a cleaner result.

However the data support the picture of a flavor asymmetry to explain the deviation from the naive value of 1/3 for the Gottfried sum. This again supports the NMC and HERMES measurement of $F_2^{\mathrm{n}}/F_2^{\mathrm{p}}$ which was used to extract the Gottfried sum.

The HERMES Monte Carlo simulation and especially the Monte Carlo generators are not yet perfectly usable for semi-inclusive studies. Hence studies of the HERMES acceptance and semi-inclusive systematics could not be performed for the semi-inclusive analysis of the data taken with unpolarized $\mathrm{H_2/D_2}$ in 1995. Nevertheless measuring multiplicities and estimating the acceptance difference for positive and negative charged

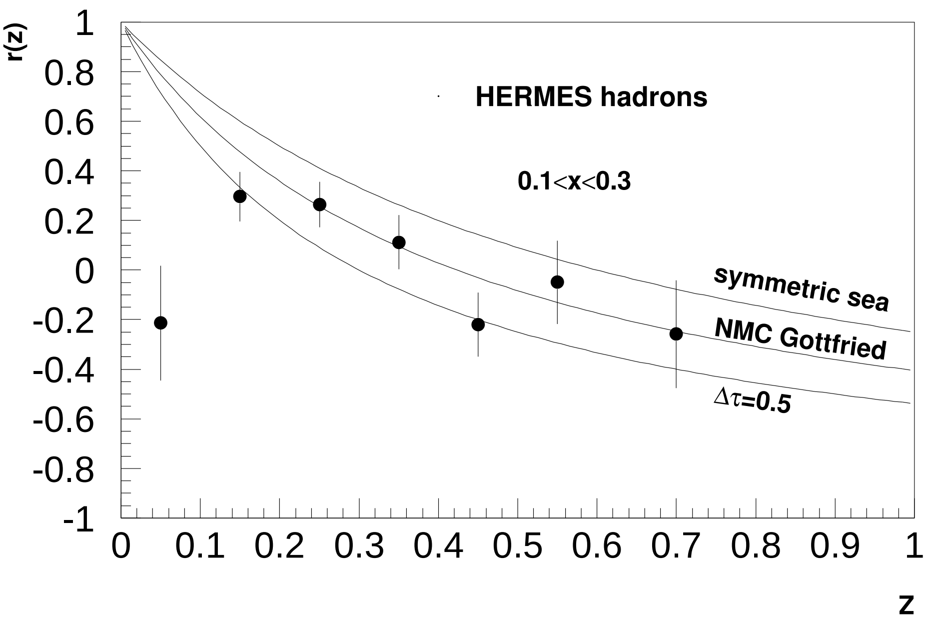

Figure 6.6: The ratio $r(x, z)$ testing the sea quark flavor asymmetry. The data shown contain all hadrons (no pion PID) and are integrated over x for $0.1 \leq x \leq 0.3$ to enhance the signal (see text). The three curves show the expected result for a flavor symmetric sea, a sea quark flavor asymmetry which explains the deviation of the Gottfried sum from its expected value measured by the NMC and the expectation for $r(x, z)$ for a sea where $\Delta\tau = 0.5$. Only statistical errors are shown.

hadrons using the data itself yields results which confirm the inclusive results. The relatively high Cerenkov threshold in 1995 leads to a relatively small pion sample so that the statistical error bars using the 45 hours of $\mathrm{H_2/D_2}$ data from 1995 are too large to extract reasonable physics quantities. However using all hadrons and cross checking with a pure pion sample gives confidence in the preliminary measurement of the valence quark ratio $d_v(x)/u_v(x)$ described here.

This analysis shows that HERMES is able to increase the precision on semi-inclusive measurements using unpolarized targets in a relatively short time. An important goal is the determination of the fragmentation functions in the HERMES kinematic regime. Finally HERMES has a vast program of polarized semi-inclusive measurements to determine the spin content of the nucleon in terms of the different quark flavors and gluon contributions.

Chapter 7

Conclusion and Outlook

The novel experimental technique, the internal polarized storage cell target, used by the HERMES experiment has been tested successfully in the 1994 test-experiment. No major problems were observed in operating the prototype detectors in the HERA environment. In spite of the limited redundancy of the tracking chamber prototypes used during the test-experiment the analysis software already was able to reconstruct tracks.

After the installation of the complete HERMES experiment and a commissioning phase data taking started in 1995. Shortly after the first data taking with unpolarized targets the first physics results, namely the structure function ratio $F_2^{\mathrm{n}}/F_2^{\mathrm{p}}$, could be extracted showing good agreement with previous measurements. With a data sample corresponding to 45 h of data taking the statistics allows an analysis of $F_2^{\mathrm{n}}/F_2^{\mathrm{p}}$ in x and Q^2. The extraction of the ratio $F_2^{^3\mathrm{He}}/F_2^{\mathrm{D}}$ from data taken in different running periods however shows that the normalization using the luminosity monitor is not yet finalized and has to be studied further. However in 1996 switching between unpolarized $\mathrm{H}_2/\mathrm{D}_2$ and $^3\mathrm{He}$ targets on a small time scale will reduce the normalization uncertainties significantly and yield a result on $F_2^{^3\mathrm{He}}/F_2^{\mathrm{D}}$ comparable to $F_2^{\mathrm{n}}/F_2^{\mathrm{p}}$.

The semi-inclusive measurements described in this thesis also show good agreement with previous measurements and are consistent with the inclusive measurements. The HERMES Monte Carlo simulation and especially the Monte Carlo generators are not yet perfectly usable for semi-inclusive studies. Hence studies of the HERMES acceptance and semi-inclusive systematics could not be performed for the semi-inclusive analysis of the data taken with unpolarized $\mathrm{H}_2/\mathrm{D}_2$ in 1995. Nevertheless measuring multiplicities and estimating the acceptance difference for positive and negative charged hadrons using the data itself yields results which confirm the inclusive results. The high Cerenkov threshold in 1995 leads to a relatively small pion sample so that the statistical error bars using the 45 hours of $\mathrm{H}_2/\mathrm{D}_2$ data from 1995 are too large to extract reasonable physics quantities. However using all hadrons and cross checking with a pure pion sample gives confidence in the preliminary measurement of the valence quark ratio $d_v(x)/u_v(x)$ described here.

Increased statistics with the 1996 data on unpolarized targets together with an improved pion identification will enable HERMES to measure the sea quark flavor asymmetry as shown in this thesis.

This analysis shows that HERMES is able to increase the precision on semi-inclusive measurements using unpolarized targets in a relatively short time. An important goal is the determination of the fragmentation functions in the HERMES kinematic regime.

Although not topic of this thesis, the major goal of the HERMES experiment is the rich program of polarized inclusive and semi-inclusive measurements to determine the spin contend of the nucleon in terms of the different quark flavors and gluon contributions. First preliminary results on the spin structure function $g_1^{\mathrm{n}}(x)$ have been presented [DIS96].

Appendix A

Technical Details

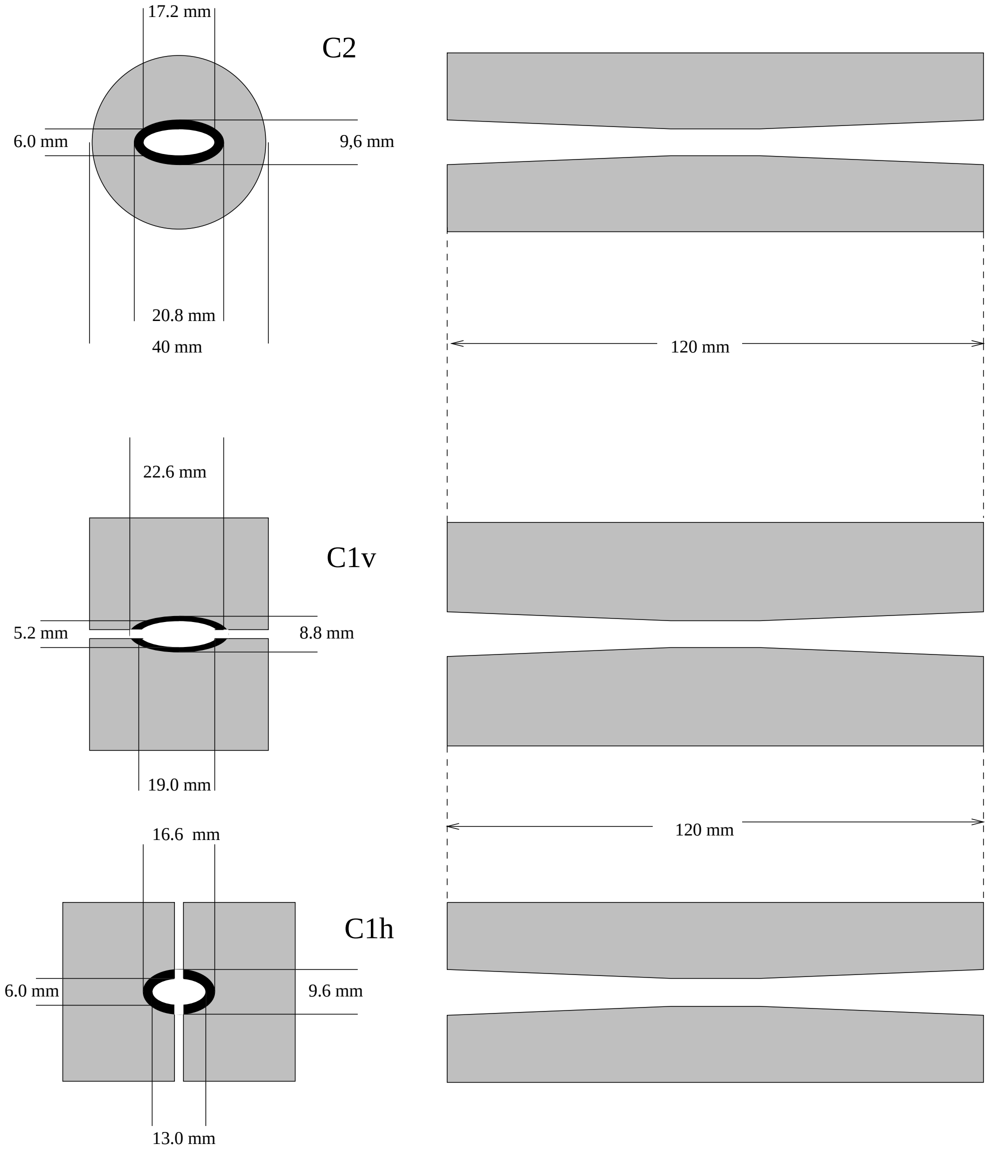

Figure A.1: The fixed collimator C2 and the two movable collimators C1h/v.

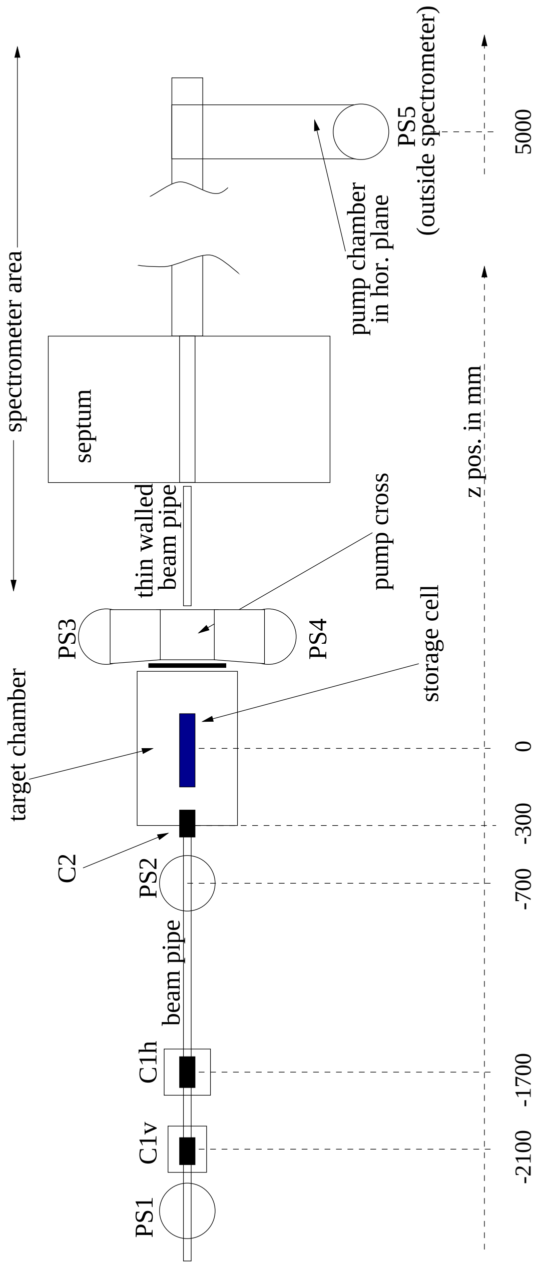

Figure A.2: Schematical top view of the vacuum system with 5 pump stands (PS1-5). PS5 is attached to a chamber connecting to the beam pipe in the horizontal gap of the spectrometer, is is mounted outside the detector. The two movable collimators (C1v and C1h) are between PS1 and PS2, the fixed collimator is located at the entrance of the beam pipe into the target chamber.

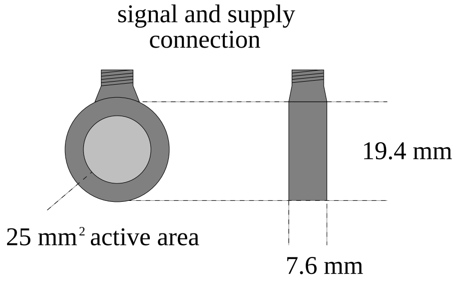

Figure A.3: The silicon Surface Barrier Detector with its dimensions. It is used in transition mode with scintillators behind it (see next figure).

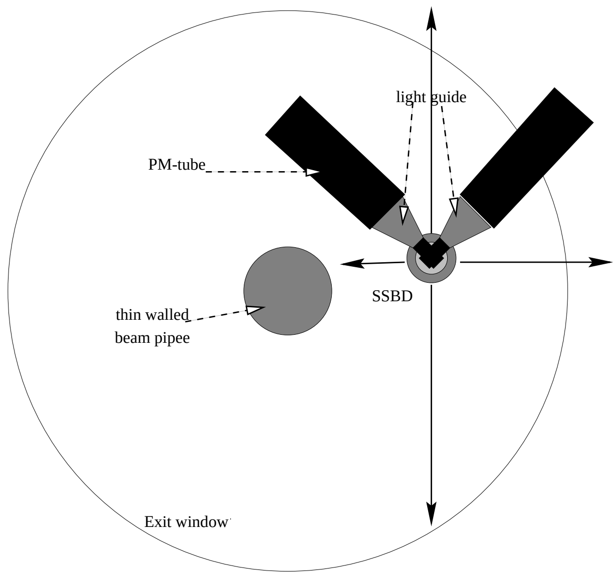

Figure A.4: The SSBD together with the charged particle scintillators in front of the target chamber exit window. It was mounted on a movable platform. The detector setup could be moved remotely in front of one half of the exit window.

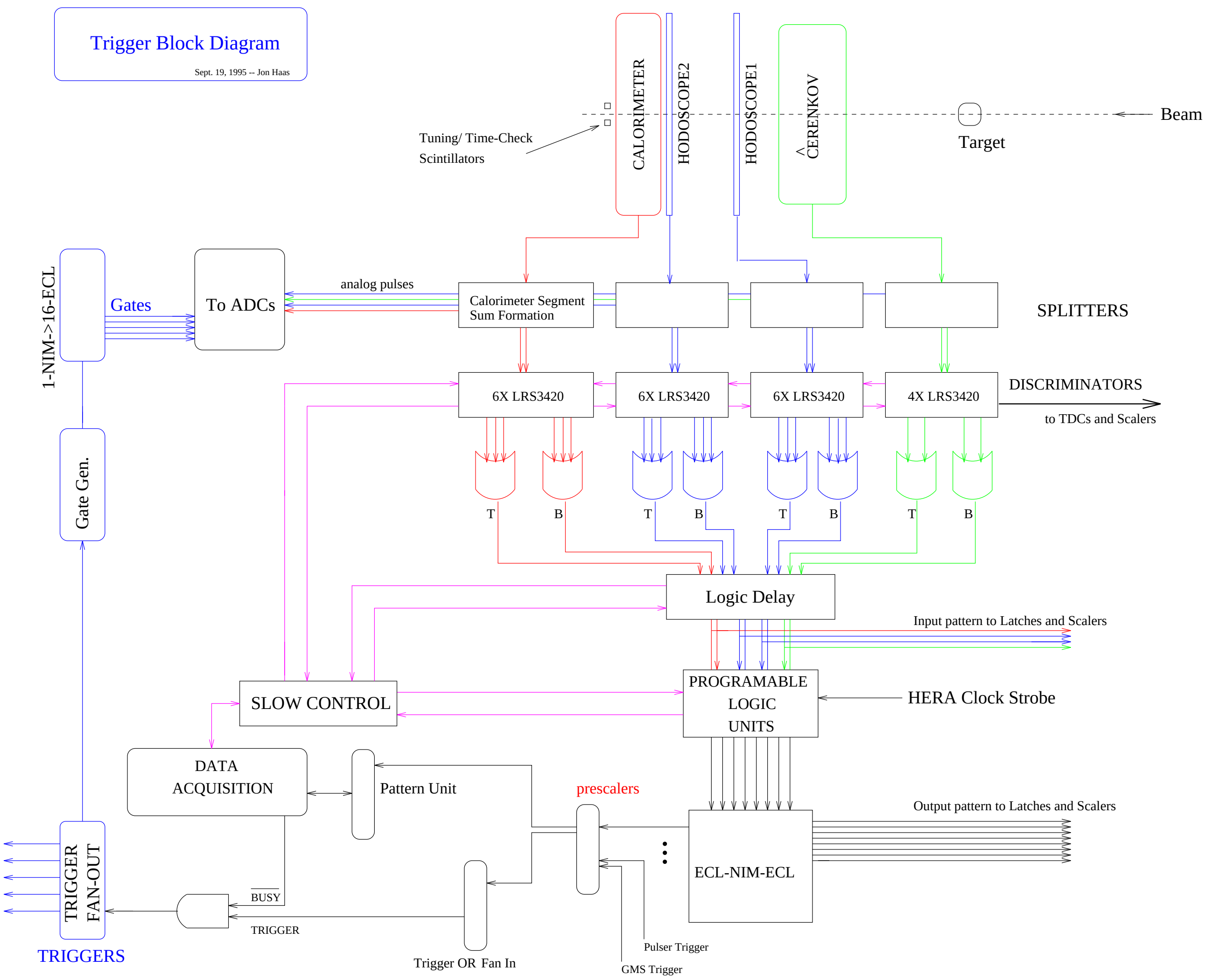

Figure A.5: Schematical block diagram of the HERMES trigger. The signals from the hodoscopes, the Cerenkov and the calorimeter are splitted and go into ADC's and discriminators. The discriminator signals go into a programable logic unit where the trigger conditions are tested using the time information from HERA to correlate the event with the bunch crossing the HERMES target.

Appendix B

Data Tables

	F_2^n/F_2^p					
x	P I	P II	P III	raw	all	sys
0.01 - 0.02	1.009 ± 0.039	0.960 ± 0.029	0.968 ± 0.035	0.726	0.984 ± 0.020	0.012
0.02 - 0.035	0.930 ± 0.030	0.949 ± 0.023	0.916 ± 0.027	0.801	0.947 ± 0.016	0.015
0.035 - 0.06	0.902 ± 0.024	0.921 ± 0.019	0.907 ± 0.022	0.834	0.922 ± 0.013	0.011
0.06 - 0.1	0.877 ± 0.022	0.847 ± 0.017	0.855 ± 0.020	0.804	0.865 ± 0.011	0.010
0.1 - 0.15	0.821 ± 0.022	0.820 ± 0.017	0.804 ± 0.020	0.785	0.826 ± 0.012	0.011
0.15 - 0.21	0.816 ± 0.024	0.748 ± 0.018	0.768 ± 0.022	0.737	0.777 ± 0.013	0.012
0.21 - 0.3	0.703 ± 0.027	0.681 ± 0.021	0.659 ± 0.024	0.660	0.690 ± 0.014	0.014
0.3 - 0.5	0.583 ± 0.034	0.578 ± 0.027	0.593 ± 0.032	0.570	0.588 ± 0.018	0.019
0.5 - 0.75	0.400 ± 0.122	0.415 ± 0.093	0.564 ± 0.123	0.453	0.442 ± 0.065	0.060

Table B.1: F_2^n/F_2^p for all periods with statistical errors in x-bins. The combined uncorrected ratio for all three periods is shown in column *raw*, the combined corrected in column *all*. The last column show the upper bound on systematic errors.

$\bar{x}$	Q^2 $F_2^{\mathrm{n}}/F_2^{\mathrm{p}} \pm$ stat.err.				
0.015	0.424 1.007 ± 0.058	0.578 0.977 ± 0.023	0.785 1.020 ± 0.081		
0.03	0.686 0.985 ± 0.038	0.936 0.936 ± 0.019	1.322 0.857 ± 0.060		
0.05	1.027 0.903 ± 0.019	1.535 0.920 ± 0.019	2.199 0.876 ± 0.060		
0.08	1.099 0.840 ± 0.026	1.582 0.862 ± 0.017	2.527 0.843 ± 0.021	3.605 0.816 ± 0.076	
0.125	1.143 0.795 ± 0.041	1.595 0.778 ± 0.018	2.576 0.851 ± 0.021	4.024 0.879 ± 0.032	5.715 0.408 ± 0.194
0.175	1.169 0.785 ± 0.075	1.612 0.751 ± 0.021	2.594 0.762 ± 0.022	4.234 0.810 ± 0.029	6.132 0.713 ± 0.062
0.25	1.775 0.666 ± 0.035	2.600 0.714 ± 0.022	4.240 0.662 ± 0.026	6.668 0.624 ± 0.039	9.560 0.890 ± 0.322
0.35	2.888 0.601 ± 0.044	4.346 0.597 ± 0.028	6.905 0.608 ± 0.033	10.264 0.520 ± 0.076	
0.55	5.427 0.784 ± 0.670	7.353 0.499 ± 0.087	10.976 0.366 ± 0.102		

Table B.2: Q^2 dependence of $F_2^{\mathrm{n}}/F_2^{\mathrm{p}}$. For each x-bin center (weighted mean) $F_2^{\mathrm{n}}/F_2^{\mathrm{p}}$ is given along with the statistical error for values of the maen Q^2.

	$F_2^{^3\mathrm{He}}/F_2^{\mathrm{D+H}}$		
x	P I	P II	P III
0.004 - 0.01	1.019 ± 0.023	0.853 ± 0.016	0.929 ± 0.021
0.01 - 0.02	1.039 ± 0.012	0.887 ± 0.009	0.952 ± 0.011
0.02 - 0.035	1.071 ± 0.010	0.916 ± 0.007	0.983 ± 0.009
0.035 - 0.06	1.087 ± 0.009	0.930 ± 0.006	1.001 ± 0.008
0.06 - 0.1	1.092 ± 0.008	0.930 ± 0.006	1.009 ± 0.007
0.1 - 0.15	1.092 ± 0.008	0.924 ± 0.006	1.010 ± 0.008
0.15 - 0.21	1.094 ± 0.009	0.936 ± 0.007	1.013 ± 0.009
0.21 - 0.3	1.087 ± 0.011	0.924 ± 0.008	1.010 ± 0.010
0.3 - 0.4	1.092 ± 0.017	0.921 ± 0.012	1.020 ± 0.016
0.4 - 0.5	1.063 ± 0.030	0.899 ± 0.021	0.991 ± 0.028
0.5 - 0.65	1.174 ± 0.064	0.940 ± 0.042	1.107 ± 0.062
0.65 - 0.85	0.822 ± 0.204	0.717 ± 0.153	0.765 ± 0.192

Table B.3: The ratio $F_2^{^3\mathrm{He}}/F_2^{\mathrm{D+H}}$ for the three data taking periods along with the statistical error, note that there is a 10% normalization uncertainty.

	$d_\mathrm{v}(x)/u_\mathrm{v}(x)$			
$\bar{x}$	P I	P II	P III	all
0.030	-0.017 ± 0.164	0.549 ± 0.168	0.651 ± 0.200	0.416 ± 0.109
0.050	0.914 ± 0.171	0.494 ± 0.102	0.379 ± 0.106	0.585 ± 0.075
0.080	0.596 ± 0.098	0.585 ± 0.073	0.478 ± 0.084	0.569 ± 0.050
0.125	0.524 ± 0.100	0.528 ± 0.079	0.733 ± 0.100	0.564 ± 0.054
0.175	0.329 ± 0.102	0.538 ± 0.099	0.549 ± 0.108	0.484 ± 0.064
0.235	0.447 ± 0.140	0.537 ± 0.107	0.322 ± 0.116	0.474 ± 0.073
0.335	0.172 ± 0.141	0.210 ± 0.101	0.466 ± 0.176	0.246 ± 0.074
0.600	0.104 ± 0.243	-0.050 ± 0.182	0.122 ± 0.242	0.022 ± 0.128

Table B.4: The valence quark distribution ratio for hadrons along with statistical errors.

	$d_{\mathrm{v}}(x)/u_{\mathrm{v}}(x)$			
$\bar{x}$	P I	P II	P III	all
0.030	-0.017 ± 0.554	1.031 ± 0.790	0.850 ± 0.547	0.715 ± 0.471
0.050	0.914 ± 0.626	1.028 ± 0.491	-0.554 ± 0.278	0.802 ± 0.322
0.080	0.596 ± 0.257	0.517 ± 0.212	0.750 ± 0.319	0.509 ± 0.147
0.125	0.524 ± 0.415	0.382 ± 0.240	0.411 ± 0.305	0.516 ± 0.181
0.175	0.329 ± 0.313	0.589 ± 0.350	0.549 ± 0.358	0.342 ± 0.221
0.235	0.447 ± 0.612	0.774 ± 0.459	-0.461 ± 0.414	0.428 ± 0.311
0.335	0.172 ± 0.818	0.549 ± 0.416	0.111 ± 0.657	0.580 ± 0.339
0.600	0.104 ± 1.935	0.522 ± 1.013	-1.536 ± 0.690	-0.022 ± 0.771

Table B.5: The valence quark distribution ratio for identified pions along with statistical errors.

Appendix C

HERMES Software Packages

HERMES developed several software packages for analysis and online monitoring and control (see chapter 4).

The HERMES software uses the ADAMO Entity Relationship database [CER94] for data handling and storage extensively. The raw data, calibration, alingnment and online monitoring data as well as control commands are kept in ADAMO structures. The DAD library package [Wan95] developed for the HERMES experiment extends ADAMO towards a distributed database enabeling multiple programs to access the same database from different platforms via network. The DAD client server concept and the extension of time-dependent data handling are used for experimental control and monitoring as well as for handling time-dependent calibration data. Figure C.1 shows the principle concept of the ADAMO and DAD data structures. The data is kept in records, where the records contain dataflows which are collections of tables and sub-dataflows. Entries of tables can be interconnected via relationships.

An extension to the script language TCL including the toolkit TK [TclTk] has been designed for the HERMES experiment called PINK [Ack95],[Fun95]. It incorporates the functionality of DAD and ADAMO in an object oriented approach. It is used extensively in online monitoring and control of the experiment, but also is used in the analysis. For visualization of data in an interactive mode or as data processing tool it extends the use of ADAMO. Figure C.2 shows the implementation of PINK into the TCL/TK toolkit. The TCL/TK code has a well defined interface for extensions which are compiled into the basic shell (script language). In addition a script library is provided for specific applications for the HERMES experiment. Almost all the online monitoring at HERMES is done using *Graphical User Interfaces* (GUI's) written in PINK. A library provides common functionality like graph widgets displaying monitored data versus time. The DAD mechanism of time-stamps and booking of data from servers ensures an easy way for GUI's to react on incoming data. Figure C.3 shows an example of the use of PINK scripts in the HERMES online monitoring and control. The status of the complete vacuum system is monitored and it allows also the control of various components.

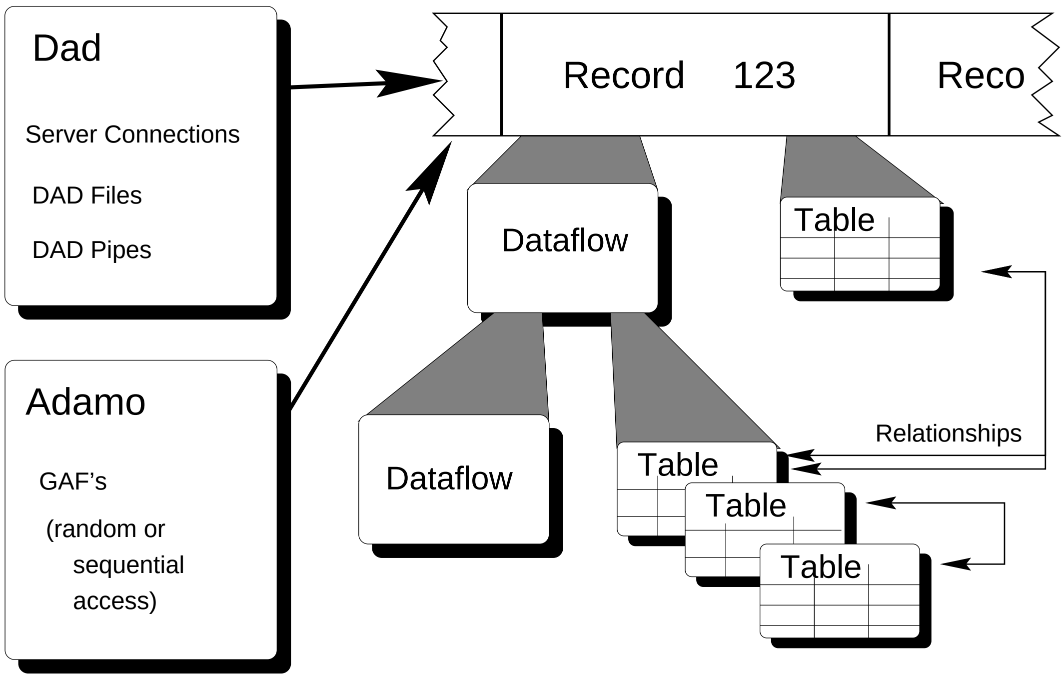

Figure C.1: ADAMO and DAD data structures are organized in records containing dataflows and tables connected via relationships.

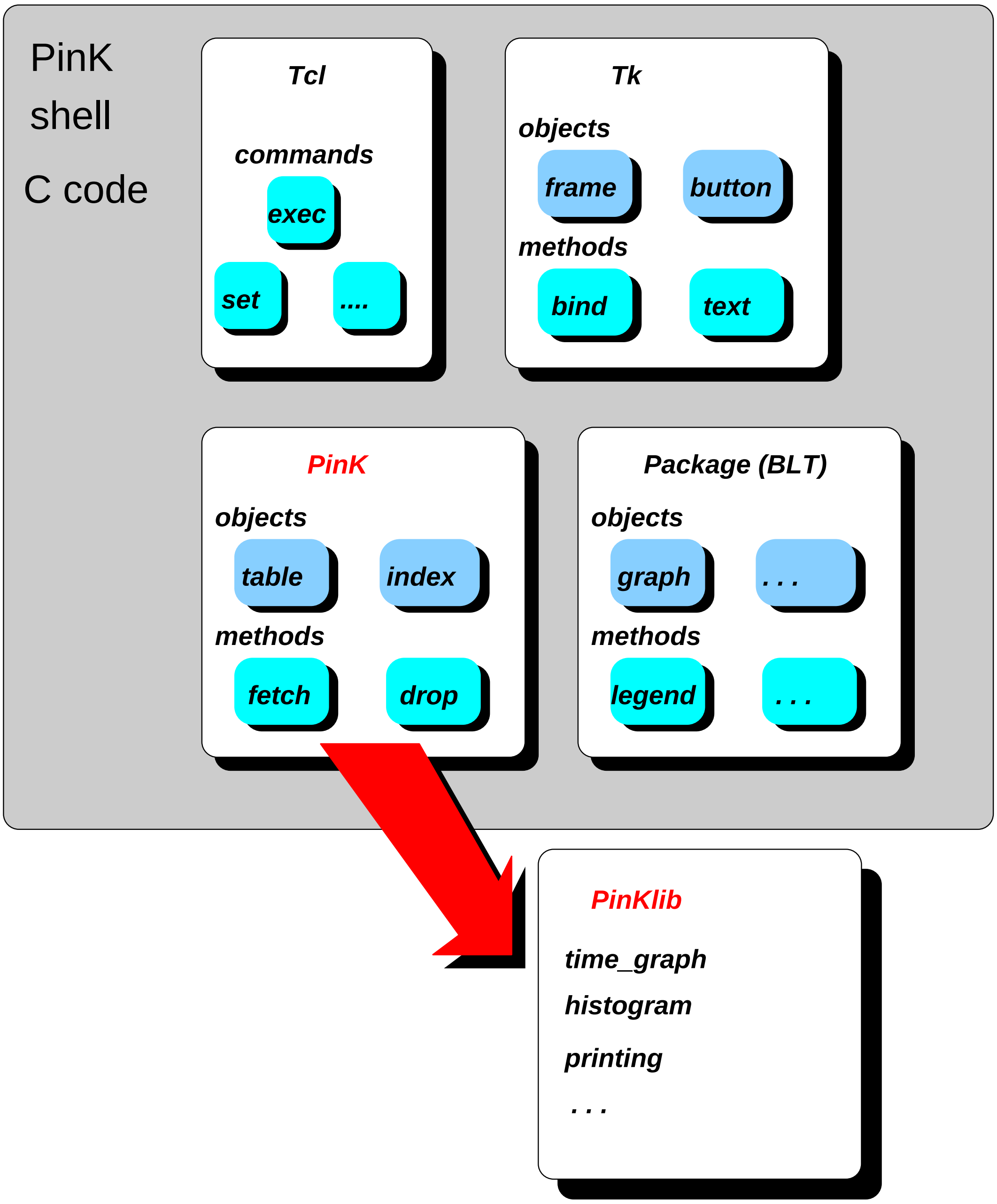

Figure C.2: Basic Concept of PINK . PINK is an extension to the TCL/TK package written in *C* . Like TK it implements objects and corresponding methods which can be invoked on the objects. It is combined along with other packages into an executable interpreting scripts. The PINKLIB is a library of scripts providing utilities for the HERMES PINK applications.

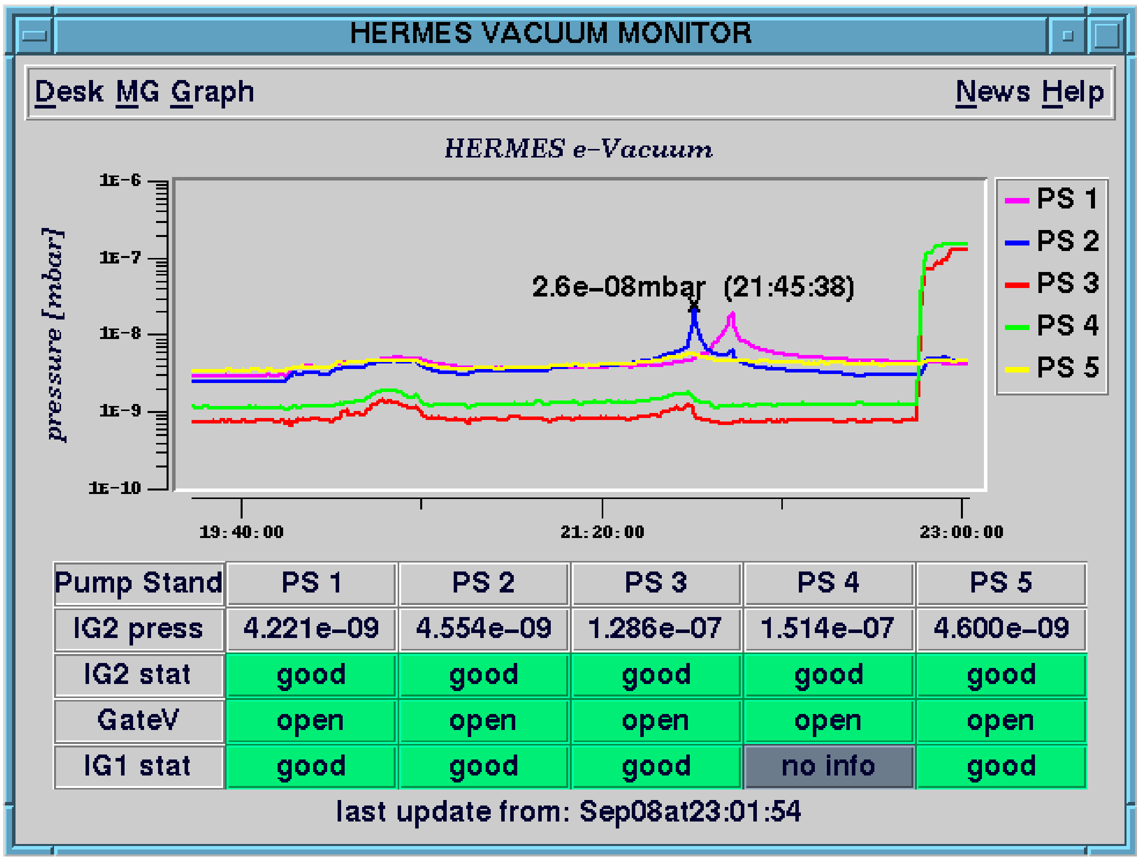

Figure C.3: The online vacuum monitor used to monitor the vacuum pressures and pump stand status of the HERMES vacuum system. It is an interactive tool and allows control and flexible monitoring. In the upper part the pressure in the beam line above the 5 pump stands is plotted online versus time. The rise of the pressures on the right side of the plot is due to the target gas being injected into the HERMES storage cell. Data points can interactively be selected to visualize the data values (the pressure and time in this case). Zooming of regions inside the plot to magnify regions of interest is also possible. The lower part shows status information of hardware components. The menu allows invocation of control applications or more specific information on special parts of the hardware like the complete status of all components of a single pump stand. The data are kept in a central DAD server and can be accessed by multiple instances of this monitor.

Bibliography

[Ack95] K. Ackerstaff et al., PINK*: A Tcl/Tk based Database Interface to* ADAMO *and* DAD, `WWW: http://dxhra1.desy.de/pink/`, Proc. of CHEP 95, Rio de Janeiro, 18. - 22. Sept. 95, to be published.

[Abr84] H. Abramowicz et al., *Measurement of Neutrino and Antineutrino Structure Functions in Hydrogen and Iron*, Z. Phys. C 25 (1984), 29-43.

[Ago94] G. D' Agostini, *A multidimensional unfolding method based on Bayes' theorem*, DESY 94-009, 1994

[Akh86] A. A. Akhundov and D. Yu. Bardin and N. M. Shumeiko, *Electromagnetic corrections to elastic radiative tail in deep inelastic lepton-nucleon scattering*, Sov. J. Nucl. Phys. 44, 1986

[All84] D. Allasia et al., *Measurement of the Neutron and Proton Structure Functions from Neutrino and Antineutrino Scattering in Deuterium*, Phys. Lett. 135 (1984), 231-236.

[Ama91] P. Amaudruz et al., *Gottfried Sum from the Ratio* F_2^n/F_2^p, Phys. Rev. Lett. 66 (1991), 2712.

[Ama95] P. Amaudruz et al., *A Re-Evaluation of the Nuclear Structure Function Ratios for* D*,* He*,* $^6\mathrm{Li}$*,* C *and* Ca, Nucl. Phys. B441 (1995), 3-11.

[Arn89] M. Arneodo et al., *Measurements of the u-valence quark distribution function in the proton and u-quark fragmentation functions*, Nuclear Physics B321, 541-560, 1989.

[Arn94] M. Arneodo et al., *Reevaluation of the Gottfried sum*, Phys. Rev. D 50 (1), R1, 1994.

[Ash91] J. Ashman et al., *Forward produced hadrons in* μp *and* μd *scattering and investigation of the charge structure of the nucleon*, CERN-PPE/91-53, March 1991

[Aub83] J. J. Aubert et. al., *Measurement of the Deuteron Structure Function and a Comparison of Proton and Neutron Structure*, Phys. Lett. B123, 1983

[Bad94] B. Badełek and J. Kwieciński, *Shadowing in the deuteron and the new F_2^n/F_2^p measurements*, Phys. Rev. D 50 (1), R4, 1994.

[Bal95] M. Ballentijn, *The ratio of structure functions for the neutron and the proton*, Akademisch Proefschrift NIKHEF, 1995.

[Bar95] D. P. Barber et al., *The first achievement of longitudinal spin polarization in a high energy electron storage ring*, Phys. Lett. B 343 (1995) 436.

[Ber87] Edmond L. Berger, *Semi-inclusive inelastic electron scattering from nuclei*, ANL-HEP-CP-87-45, 1987.

[Ber95] S. Bernreuther et al., *Design and performance of the large HERMES drift chambers*, Nucl. Instr. Meth. A 367, 1995.

[Bjo66] J. D. Bjorken, *Application of the Chiral U(6) $\times$ U(6) Algebra of Current Densities*, Phys. Rev. 148 (1966) 1467 and J. D. Bjorken, *Inelastic Scattering of Polarized Leptons from Polarized Nucleons*, Phys. Rev. D1 (1970) 1377.

[Brü93] A. Brüll, *Die Strukturfunktionen des Nukleons bei kleinen Werten von X*, Dissertation, Universität Freiburg, 1993.

[Brü96] A. Brüll, personal communication, data are to be published.

[Car75] R. Carlitz, *SU(6) Symmetry Breaking Effects in Deep Inelastic Scattering*, Phys. Lett. B58, (1975), 345-347.

[CER94] *ADAMO – Entity-Relationship Programming System, Version 3.3*, `WWW: http://www1.cern.ch/Adamo/ADAMO_ENTRY.html`, Programming Techniques Group, ECP Division, CERN, Geneva, 1994.

[Cio93] C. Ciofi degle Atti et. al., *Nuclear Effects in Deep Inelastic Scattering of polarized $^3\mathrm{He}$ and the Neutron Spin Functions*, Phys. Rev. Vol 48, 1993.

[Clo79] F. E. Close, *An Introduction to Quarks and Partons*, Academic Press, London 1979.

[DIS96] K. Ackerstaff, *Semi-Inclusive Data from polarized $^3\mathrm{He}$ and unpolarized $\mathrm{H}_2/\mathrm{D}_2$ targets*, talk given at: Int. Workshop on Deep Inelastic Scattering and related Phenomena, Rome, 14-19 April, to be published in the proceedings.
D. DeSchepper, *g_1 Neutron from polarized $^3\mathrm{He}$*, talk given at: Int. Workshop

on Deep Inelastic Scattering and related Phenomena, Rome, 14-19 April, to be published in the proceedings.

[Dür91] M. Düren, *Protecting the* HERMES *Experiment from Synchrotron Radiation*, Proc. of 9^{th} Int. Symposium of High Energy Spin Physics, Sept. 1990, Bonn; eds. W. Meyer et al. (Springer-Verlag, Berlin, 1991) Vol. 2, 217.

[Dür92] M. Düren et al., *Test of a polarized hydrogen gas target based on the storage cell technique*, Nucl. Instr. Meth. A 322, 1992.

[Dür94] M. Düren, K. Zapfe, *Experimental Techniques and Physics in a Polarized Storage Ring*, DESY Internal Report, DESY 94-238, 1994.

[Dür95] M. Düren, *The HERMES Experiment: From the Design to the First Results*, Habilitationsschrift, Friedrich-Alexander-Universität Erlangen-Nürnberg, 1995.

[Eic92] E. J. Eichten, I. Hinchliff, C. Quigg, *Flavour asymmetry in the light-quark sea of the nucleon*, Phys.Rev.D 45 (1992) 2269.

[Ell74] J. Ellis, R. L. Jaffe, *Sum Rule for Deep-Inelastic Electroproduction from Polarized Protons* Phys.Rev.D 9 (1974), 1444.

[Ell95] J. Ellis and M. Karliner, *Nucleon Spin*, CERN-TH 95-279, 1995.

[EPIO93] CERN-CN devision, *EPIO, Experimental Physics Input Output Package*, CERN Program Library Long Writeup I101, CERN Geneva, 1993.

[Fer96] M. Ferstl, personal communication.

[Fie77] R. D. Field and R. P. Feynman, *Quark elastic scattering as a source of high-transverse-momentum mesons*, Phys. Rev. D (15,9) 1977.

[Fie78] R. D. Field and R. P. Feynman, *A Parametrization of the Properties of Quark Jets*, Nucl. Phys. B (136) 1978

[Fie93] K. Fiedler, *Absorption von Synchrotronstrahlung durch Stahlfenster*, Internal Report, 1993

[Fie95] K. Fiedler, *Studien zum protoneninduzierten Untergrund am* HERMES *-Experiment*, Diplomarbeit, Physikalisches Institut II, Universität Erlangen-Nürnberg, 1995.

[Fun95] M.-A. Funk, personal communication, documentation: *The PinK Documentation Page*, `WWW: http://dxhra1.desy.de/pink/`, 1995

[Fun96] M.-A. Funk, personal communication, documentation: *Hanna: A C-based HERMES Analysis Tool*, `WWW: http://dxhra1.desy.de/hanna/`, 1996.

[Got67] K. Gottfried, *Sum rule for high-energy electron-proton scattering*, Phys. Rev. Lett. 18 (1967), 1174.

[Gre95] W. Greiner, A. Schäfer, *Quantum Chromodynamics*, Springer Verlag, Berlin, 1995.

[Gro94] C. Großhauser, *Optimierung der transversalen Elektronenpolarisation von HERA bei 26.67 GeV*, Diplomarbeit, Physikalisches Institut II, Universität Erlangen-Nürnberg, 1994.

[Hae85] W. Haeberli, Proc. Workshop on Nucl. Phys. with Stored Cooled Beams, Indiana 1984, eds. P. Schwandt and H. O. Meyer, AIP Conf. Proc. 128, 1985 NIKHEF-H/94-36, 1994.

[Hal84] F. Halzen, A. D. Martin G., *Quarks and Leptons: An Introductory Course in Modern Particle Physics*, New York, 1984.

[Har94] F. G. Hartjes et al., *The construction of a microstrip gas tracker for HERMES*, NIKHEF Report, NIKHEF-H/94-36, 1994.

[Hen95] Th. Henkes et al., *Operational Experiences with the Large Microstrip Gas Tracker of HERMES*, HERMES Internal Report, 95-066, 1995.

[HER93] Hermes Collaboration, HERMES *Technical Design Report*, DESY-PRC 93-06, MPIH-V20 1993, 1993.

[Ihs96] H. Ihssen, personal comunication.

[Jac92] H. E. Jackson, *Sea-quark flavour asymmetry in* HERMES , Argonne National Lab., PHY-7076-ME-92, 1992.

[Jon94] G. T. Jones et. al, *Dtermination of the Ratio $r_v = d_v/u_v$ of the Valence Quark Distributions in the Proton from Neutrino and Antineutrino Reactions on Hydrogen and Deuterium*, Z. Phys. C62 (1994), 601-607.

[Kab95] E.-M. Kabuß, *Die Untersuchung der Struktur des Nukleons in tiefinelastischer Lepton-Nukleon-Streuung*, Habilitationsschrift, Johannes-Gutenberg-Universität Mainz, 1995.

[Klei87] K. Kleinknecht, *Detektoren für Teilchenstrahlung*, Teubner Verlag, Stuttgart, 1987.

[Kra95] L. Kramer et al., *A cryogenic storage cell for polarized internal gas targets*, Nucl. Instr. Meth. A 365, 1995.

[Lai95] H. L. Lai et al., *Global QCD analysis and the CTEQ parton distributions*, Phys. Rev. D 51 (1995), 4763.

[Lea82] E. Leader and Elliot, *An Introduction to gauge theories and the `new physics'*, Cambridge University Press, Cambridge 1982.

[Lee93] K. Lee et al., *A laser optically pumped polarized* $^3\mathrm{He}$ *target for storage rings*, Nucl. Instr. Meth. A 333 (1993) 294.

[Lev91] J. Levelt, P. J. Mulders, A. W. Schreiber, *Isospin distribution in the proton and the Gottfried sum rule from leptoproduction of hadrons*, Phys.Lett. B 263 (3,4), 498ff, 1991.

[Man92] A. Manohar, *An Introduction to Spin Dependent Deep Inelastic Scattering*, Proc. of the 7th Lake Louise Winter Institute, World Scientific, Singapore, 1992.

[Mar76] J. F. Martin et al., *Particle ratios in inclusive electroproduction from hydrogen and deuterium*, Physics Letters 65B (5) 483ff, 1976.

[Mar93a] A. D. Martin and W. J. Stirling, *New information on parton distributions*, Phys. Rev. D (47,3) 1993.

[Mar93b] A. D. Martin and W. J. Stirling, *Parton distributions updated*, Phys. Lett. B (306) 1993.

[Oel95] Ph. Oelwein, *Messung der longitudinalen Elektronenpolarisation beim Speicherring HERA und Monte-Carlo-Studien zur Kalibration des HERA-Elektronen-Polarimaters*, Diplomarbeit, Max-Planck-Institut für Kernphysik Heidelberg, Universität Heidelberg 1995.

[TclTk] J.K. Ousterhout, *Tcl and the Tk Toolkit*,Addison-Wesley Massachusetts, 1994.

[Pat94] S. F. Pate, *Progress at HERMES: Preparations for measurements of nucleon spin structure functions*, Proc. of 8^{th} Int. Symposium on *Polarization Phenomena in Nuclear Physics*, Bloomington 1994, eds. E. J. Stephenson and S. E. Vigdov, AIP Conf. Proc. 339 (95) 71.

[Pat95] S. F. Pate et al., *Cryogenic Polarized Internal* $^3\mathrm{He}$ *Gas Target for* HERMES , Proc. International Workshop on Polarized Beams and Polarized Gas Targets, Köln, 1995, in preparation; MIT-LNS-95-159, 1995.

[PDG94] The Particle Data Group, *Review of Particle Properties*, Phys. Rev. D, Vol. 50 (1994), 1535.

[Pit87] D. D. Pitzl, *Abschirmung der* HERA *Detektoren gegen Synchrotronstrahlung*, Diplomarbeit, II. Institut für Experimentalphysik, Universität Hamburg, 1987

[Pit95] M. L. Pitt et al., *TOM: A Target Optical Monitor of Polarization and Luminosity for Polarized Internal Gas Targets*, Presented to the International Workshop on Polarized Beams and Polarized Gas Targets, Köln, 1995.

[Pot96] S. Potashov, *Offline Calibration of the HERMES Luminosity Monitor: Procedure and Software*, HERMES Internal Note, 96-012, 1996.

[Roe94] G. Röper, *Messung der Feldverteilung des HERMES Spektrometermagneten*, Diplomarbeit, DESY, 1994.

[Sch88] P. Schmüser, *Feynman-Graphen und Eichtheorien für Experimentalphysiker*, Springer-Verlag, Berlin, 1988.

[Shi64] L. I. Shiff, *Theory of the Electromagnetic Form Factors of* H^3 *and* He^3, Phys. Rev. 133(1964)3B,802

[Smi95] G. I. Smirnov, *On the universality of the* x *and* A *dependence of the EMC effect and its relation to parton distributions in nuclei*, CERN/PPE (submitted to Physics Letters), 1995.

[Sok64] A. A. Sokolov and I. M. Ternov, *On Polarization and Spin Effects in the Theory of Synchrotron Radiation*, Sov. Phys Dokladi 8, (1964), 1203.

[Sto94] F. Stock et al., *The FILTEX/HERMES polarized hydrogen atomic beam source*, Nucl. Instr. Meth. A 343, 1994.

[Wan95] W. Wander et al., *DAD – Distributed Adamo Database system at Hermes*, `WWW: http://dxhra1.desy.de/dad/`, Proc. of CHEP 95, Rio de Janeiro, 18. - 22. Sept. 95, to be published.

[Wan96] W. Wander, *Rekonstruktion hochenergetischer Streuereignisse im Hermes Experiment*, Doktorarbeit, Physikalisches Institut II, Universität Erlangen-Nürnberg, 1996.

[Whi90] L. W. Whitlow et al., *A precise extraction of* $R = \sigma_L/\sigma_T$ *from a global analysis of the SLAC deep inelastic e-p and e-d scattering cross sections*, Phys. Lett. B 250 (1990), 193.

[Whi92] L. W. Whitlow et al., *Precise measurements of the proton and deuteron structure functions from a global analysis of the SLAC deep inelastic electron scattering cross sections*, Phys. Lett. B 282 (1992), 475.

[Whi74] R. R. Whitney et al., *Quasielastic Electron Scattering*, Phys. Rev. C9(1974), 2230

[Zap95] K. Zapfe-Düren, *The Internal Storage Cell Target for HERMES*, Proc. of International Workshop on Polarized Beams and Polarized Gas Targets, Köln, 1995, in preparation.

[Zap95a] K. Zapfe et al., *A High-Density polarized Hydrogen Gas Target for Storage Rings*, Rev. Sci. Instr. 66, 1995.

[Zap96] K. Zapfe et al., *Detailed studies of a high-density polarized hydrogen gas target for storage rings*, Nucl. Inst. Meth. A 386, 1996.

[Zap96a] K. Zapfe et al., *Beam induced Heating of the HERMES Storage Cell*, HERMES Internal Report, 96-010, 1996

Acknowledgments

The environment in the HERMES collaboration provided a very creative and inspiring atmosphere. There has always been room for new ideas and I enjoyed learning from experienced people from many countries. Setting up an experiment like HERMES is a lot of work, but also an exciting project. I want to express my thanks to all members of the HERMES collaboration for sharing the work and the success with me.

I would like to thank my advisor Albrecht Wagner for his constant support throughout this project. The regular meetings with him kept me focused and I benefited from his experienced advice. Thanks for pointing out the success when I only saw the problems.

During the first part of my work at HERMES Kirsten Zapfe-Düren introduced me to the HERMES project and I learned a lot about the HERMES target, I would like to thank her for this and for supporting me during my work in the target group.

Special thanks go to Yorck Holler supporting me whenever I needed help in the East Hall, he organized almost everything at any time.

I would like to express special thanks to the people who participated in the setup of the test-experiment and the $^3\mathrm{He}$-target, particularly Steve Pate, Laird Kramer, Mike Vetterli, Dirk DeSchepper, Friedemann Stock and Thomas Henkes.

The work in the HERMES software group has been a great pleasure, I profited from the experienced *hackers* and enjoyed working and the entertainment inside and outside our office. Especially I have to thank Wolfgang Wander for teaching me lots about computers and software, answering hundreds of questions and pointing me to the right *man-pages*. I would like to thank Philipp Oelwein not only for his valuable comments to this thesis but also for the organization of the fruitful *offsite* meetings. I am grateful to Marc-André Funk for his work on PINK, his help in any software problem and the fruitful discussions not only concerning physics.

I would like to thank all people in the HERMES analysis group coordinated by Michael Düren whom I thank for his physics advice and critical comments. Thanks also to Holger Ihssen for his suggestions and contributions to the analysis effort.

The discussions with Antje Brüll and Hal Jackson have much improved my understanding of the HERMES physics. I am grateful for their comments and would like thank Antje for her help in the analysis and for carefully reading parts of this thesis.

I have to thank my friends and parents for their support and for all they did for me in the last years.

Finally I want to express thanks to my daughter Fenna-Louise and her mother Imke for their patience, love and encouragement, I have to apologize for being absent from my family too often and thank Imke for making it possible for me to do all this work.

Ich versichere, diese Arbeit selbständig angefertigt und alle wesentlichen Hilfsmittel und Quellen angegeben zu haben.

Klaus Ackerstaff

Hamburg, im Mai 1996